

# A genetic program boosts mitochondrial function to power macrophage tissue invasion

Shamsi Emtenani<sup>1</sup>, Elliott T. Martin<sup>2</sup>, Attila Gyoergy<sup>1</sup>, Julia Bicher<sup>1</sup>, Jakob-Wendelin Genger<sup>4</sup>, Thomas R. Hurd<sup>3</sup>, Thomas Köcher<sup>5</sup>, Andreas Bergthaler<sup>4</sup>, Prashanth Rangan<sup>2</sup>, Daria E. Siekhaus<sup>1\*</sup>

1) Institute of Science and Technology Austria, 3400 Klosterneuburg, Austria

2) University at Albany, Department of Biological Sciences, RNA Institute, Albany, NY 12222

3) Department of Molecular Genetics, University of Toronto, Toronto, Ontario, M5G 1M1, Canada.

4) CeMM Research Center for Molecular Medicine of the Austrian Academy of Sciences, 1090 Vienna, Austria

5) Vienna BioCenter Core Facilities, 1030 Vienna, Austria

\*Correspondence: [daria.siekhaus@ist.ac.at](mailto:daria.siekhaus@ist.ac.at)

## SUMMARY

Metabolic adaptation to changing demands underlies homeostasis. During inflammation or metastasis, cells leading migration into challenging environments require an energy boost, however what controls this capacity is unknown. We identify a previously unstudied nuclear protein, Atossa, as changing metabolism in *Drosophila melanogaster* immune cells to promote tissue invasion. Atossa's vertebrate orthologs, FAM214A-B, can fully substitute for Atossa, indicating functional conservation from flies to mammals. Atossa increases mRNA levels of Porthos, an unstudied RNA helicase and two metabolic enzymes, LKR/SDH and GR/HPR. Porthos increases translation of a gene subset, including those affecting mitochondrial functions, the electron transport chain, and metabolism. Respiration measurements and metabolomics indicate that Atossa and Porthos powers up mitochondrial oxidative phosphorylation to produce sufficient energy for leading macrophages to forge a path into tissues. As increasing oxidative phosphorylation enables many crucial physiological responses, this unique genetic program may modulate a wide range of cellular behaviors beyond migration.

Keywords: immune cell, invasion, metabolism, mitochondria, translation, oxidative phosphorylation, RNA helicase, tissue infiltration, migration

## INTRODUCTION

Charged with protecting the organism against continuously changing threats, the immune system must constantly adapt, altering the location, number, and differentiation status of its different immune cell subtypes (Nicholson, 2016). Such continuous adjustment comes at a cost, as it requires high levels of energy. However, how immune cells adjust their metabolic capacities to achieve these increased metabolic requirements is just beginning to be

47 understood (Guak et al., 2020; O'Neill et al., 2016). The main energy currency in the cell is  
48 ATP. The conversion of carbohydrates into ATP is mediated mostly by cytoplasmic  
49 glycolysis and the mitochondrial TCA cycle that feeds electron donors into oxidative  
50 phosphorylation (OxPhos) complexes I through IV. Anaerobic glycolysis is quick and does  
51 not require oxygen, but respiratory OxPhos extracts considerably more ATP from a single  
52 molecule of glucose, albeit more slowly (Berg et al., 2002). Amino acids and fatty acids also  
53 feed into the TCA cycle and fuel OxPhos (O'Neill et al., 2016). OxPhos is most directly  
54 regulated by the activity and the amount of complexes I through V that carry it out  
55 (Hüttemann et al., 2007), but can also be affected by mitochondrial fusion (Rambold et al.,  
56 2015) and biogenesis (Le Bleu et al., 2014). Upregulation of OxPhos is known to be required  
57 for many important immune cell functions, such as B cell antibody production (Price et al.,  
58 2018), pathogenic T cell differentiation during autoimmunity (Shin et al., 2020), and CD8+  
59 memory T cell development and expansion (van der Windt et al., 2012; van der Windt et al.,  
60 2013), T reg suppressive function (Angelin et al., 2017; Weinberg et al., 2019; Beir et al.,  
61 2015) and the maturation of anti-inflammatory macrophages (Vats et al., 2006). However,  
62 what genetic programs immune cells utilize to upregulate OxPhos remains unclear and how  
63 such shifts in metabolism could influence immune cell migration is unexplored.

64  
65 Immune cells move within the organism to enable their distribution and maturation (Kierdorf  
66 et al., 2015; Masopust and Schenkel, 2013), as well as to detect and respond to homeostatic  
67 challenges, injuries, tumors or infections (Woodcock et al., 2015; Luster et al., 2005;  
68 Ratheesh et al., 2015). To migrate across unimpeded environments cells expend energy to  
69 restructure their own actin cytoskeleton, activate myosin ATPase, and reorganize their cell  
70 membrane (Bernstein and Bamberg, 2003; Cuvelier et al., 2007; Rottner and Schaks, 2019;  
71 Li et al., 2019). Even greater energy requirements exist when cells must also remodel their  
72 surroundings as they move ahead against the resistance of flanking cells or extracellular  
73 matrix (Zanotelli et al., 2018; Zanotelli et al., 2019; Cunniff et al., 2016; Kelley et al., 2019).  
74 Most studies on the metabolism that enables immune cell migration *in vitro* or *in vivo* have  
75 highlighted the importance of glycolysis, in macrophages, dendritic cells and regulatory T  
76 cells (Guak et al., 2018; Kishore et al., 2018; Semba et al., 2016; Liu et al., 2019). To our  
77 knowledge, only one study has demonstrated a need for a functional electron transport chain  
78 (ETC) to speed neutrophil migration *in vivo* (Zhou et al., 2018) potentially through polarized  
79 secretion of ATP to amplify guidance cues (Bao et al., 2015). In cancer cells an increase in  
80 the transcription of mitochondrial genes, mitochondrial biogenesis and thus OxPhos by PGC-  
81 1 appears to underlie enhanced invasion and metastasis (Le Bleu et al., 2014). OxPhos is  
82 particularly required in the first cancer cell leading coordinated chains into challenging  
83 environments *in vitro* (Khalil et al., 2010; Commander et al., 2020); these leader cells have  
84 been shown to need higher ATP levels to create a path (Zhang et al., 2019). Although the  
85 ability of immune cells to invade tissues or tumors also depends on movement against  
86 surrounding resistance, it is not known if immune cells similarly require OxPhos for such  
87 infiltration.

88  
89 To identify new mechanisms governing *in vivo* migration, we study *Drosophila*  
90 macrophages, also called plasmatocytes. Macrophages are the primary phagocytic and

91 innate immune cell in *Drosophila* and share remarkable similarities with vertebrate  
92 macrophages in ontogeny, functional properties, and migratory behavior (Brückner et al.,  
93 2004; Nourshargh and Alon, 2014; Ratheesh et al., 2015; Weavers et al., 2016; Wood and  
94 Martin, 2017; Weavers et al., 2020). Phagocytic macrophages not only resolve infections,  
95 but also influence development and homeostasis (Caputa et al., 2019; Riera-Domigo et al.,  
96 2020; Buck et al., 2016; Bunt et al., 2010). Embryonic *Drosophila* macrophages follow  
97 guidance cues to disseminate along predetermined routes (Cho et al., 2002; Brückner et al.,  
98 2004; Wood et al., 2006) from their initial site of specification. During embryogenesis a  
99 dynamic chain of macrophages invades into the extended germband between the closely  
100 apposed ectoderm and mesodermal tissues, moving against the resistance of surrounding  
101 tissues (Siekhaus et al., 2010; Ratheesh et al., 2018; Valoskova et al., 2019). Importantly,  
102 the rate limiting step for this tissue invasion is the infiltration of the pioneer macrophage, a  
103 process affected both by the properties of the surrounding tissues (Ratheesh et al., 2018) as  
104 well as macrophages themselves (Valoskova et al., 2019; Belyaeva et al., 2021).

105

106 Here we identify a program that powers the invasive capability of these pioneer  
107 macrophages *in vivo*. We characterize a metabolic shift orchestrated in these immune cells  
108 by a single previously unexamined nuclear factor that we name Atossa. We show that  
109 Atossa induces higher mRNA levels of two metabolic enzymes and a previously unstudied  
110 helicase. This helicase which we name Porthos enhances translation of a diverse set of  
111 proteins, including those affecting mitochondrial and metabolic function, to increase  
112 OxPhos and ATP. Our work thus reveals a detailed cellular mechanism that induces  
113 concerted metabolic and mitochondrial reprogramming to support higher energy levels.  
114 Given that we find that Atossa's mammalian orthologs maintain its function, our data lay  
115 the foundation for mammalian studies on diverse pathological conditions, from  
116 autoimmunity to cancer, as well as those independent of invasion.

117

## 118 **RESULTS**

### 119 ***CG9005* is required in macrophages for their early invasion into the extended germband**

120 To identify unknown molecular pathways mediating germband invasion, we searched for  
121 previously uncharacterized genes enriched in macrophages prior to and during germband  
122 tissue entry. Examining the BDGP *in situ* project ([https://insitu.fruitfly.org/cgi-  
123 bin/ex/report.pl?ftype=1&ftext=FBgn0033638](https://insitu.fruitfly.org/cgi-bin/ex/report.pl?ftype=1&ftext=FBgn0033638)) we identified *CG9005* as a gene fitting these  
124 requirements. *CG9005* is enriched in macrophages from their birth through their invasion of  
125 the germband. *CG9005* is maternally deposited and expressed in all mesodermal cells during  
126 stage 4-6 when macrophages are specified in the head mesoderm. *CG9005* is further  
127 upregulated in macrophages starting at Stage 7 while its expression decreases in the  
128 remaining mesoderm. *CG9005* continues to be expressed during Stage 9-12 in macrophages,  
129 during their ingression, dissemination, and movement towards and into the germband. After  
130 invasion, *CG9005* is downregulated in macrophages to match the lower expression levels  
131 found ubiquitously in the embryo.

132

133 We examined a P element insertion allele, *CG9005*<sup>BG02278</sup>, henceforth abbreviated to

134 *CG9005<sup>PBG</sup>*, visualizing macrophages through expression of a nuclear fluorescent marker.  
135 Quantification of the number of macrophages within the germband in fixed embryos at Stage  
136 12 revealed a 36% decrease in *CG9005<sup>PBG</sup>* mutant embryos compared to the control (Figs.  
137 1A-B and 1D), similar to that seen when *CG9005<sup>PBG</sup>* was placed over either *Df(2R)ED2222*  
138 or *Df(2R)BSC259* that remove the gene entirely (Fig. 1D), demonstrating that *CG9005<sup>PBG</sup>* is a  
139 genetic null for macrophage germband invasion. Expressing *CG9005* in macrophages in the  
140

141 **Figure 1. *CG9005* acts in macrophages to spur pioneer cell infiltration into the germband tissue. Fig 1A-**  
142 **C.** Representative confocal images of Stage 12 embryos from the control, the *P{GT1}CG9005<sup>BG02278</sup>* P element  
143 mutant (henceforth called *CG9005<sup>PBG</sup>*), and *CG9005<sup>PBG</sup>* with *CG9005* expression restored in macrophages.  
144 Macrophages (red) and phalloidin to visualize embryo (green). “*mac*” represents the *srpHemo-Gal4* driver.  
145 Germband edge indicated by dotted white line. **Fig 1D.** Quantification reveals a significant decrease in the  
146 number of macrophages that have penetrated the germband in Stage 12 embryos from *CG9005<sup>BG</sup>* (n=56), and  
147 from *CG9005<sup>BG</sup>* over two deficiencies (Df) that completely remove the gene (*CG9005<sup>BG</sup>/Df1(2R)* n=25 and  
148 *CG9005<sup>BG</sup>/Df2(2R)* n=9), compared to the control (n=35). Macrophage expression of *CG9005* rescues the  
149 mutant phenotype arguing that *CG9005* is required only in macrophages for germband penetration (n=18 for  
150 rescue, p<0.0001 for control vs mutant, p=0.98 for control vs rescue, p=0.001 for mutant vs rescue).  
151 *Df1(2R)=Df(2R)ED2222*. *Df2(2R)=Df(2R)BSC259*. **Fig 1E.** Macrophage specific knockdown of *CG9005* by  
152 *UAS RNAi* lines under the control of *srpHemo-GAL4* can recapitulate the mutant phenotype (control 1 n=22,  
153 *CG9005 RNAi 1* (VDRC 106589) n=20; p<0.0001; control 2 n=21, *CG9005 RNAi 2* (VDRC 36080) n=23;  
154 p<0.0001; control 3 n=35, *CG9005 RNAi 3* (BL33362) n=28, p<0.0001). **Fig 1F.** Stills from two-photon movies  
155 of control and *CG9005<sup>PBG</sup>* mutant embryos showing macrophages (nuclei, red) migrating starting at Stage 10  
156 from the head towards the germband and invading into the germband tissue. Elapsed time indicated in minutes.  
157 The germband edge (white dotted line) was detected by yolk autofluorescence. **Fig 1G-H.** Quantification shows  
158 no change in macrophage migration speed (G) in the head or (H) between the yolk sac and the germband edge  
159 in the *CG9005<sup>PBG</sup>* mutant compared to the control. Head speed: control and mutant=2.2  $\mu\text{m}/\text{min}$ ; movie #:  
160 control=8, mutant=3; track #: control=360, mutant=450, p=0.65. Between yolk sac and germband speed:  
161 control=2.6 and mutant=2.4  $\mu\text{m}/\text{min}$ ; # movies: control=3; # tracks: control=46, mutant=19, p=0.62.  
162 **Fig 1I.** The time required for the first macrophage nucleus to enter into the extended germband is increased by  
163 65% in the *CG9005<sup>PBG</sup>* mutant compared to the control (control=22.8 min, n=7, mutant=37.4 min, n=5,  
164 p<0.0001). **Fig 1J-K.** The migration speed of the first and second macrophage into the germband between the  
165 mesoderm and ectoderm is significantly slower in the *CG9005<sup>PBG</sup>* mutant compared to the control. First  
166 macrophage speed: control=2.5 and mutant=2.1  $\mu\text{m}/\text{min}$ , movie #: control=6, mutant=5, p=0.012. Second  
167 macrophage speed: control=2.9 and mutant=2.2  $\mu\text{m}/\text{min}$ , movie #: control=5, mutant=5, p=0.03. **Fig 1L.** The  
168 migration speed of the third to fifth macrophage nuclei along the first 25-30  $\mu\text{m}$  of the path between the  
169 germband mesoderm and ectoderm is similar in the *CG9005<sup>PBG</sup>* mutant and the control (speed: control=2.5 and  
170 mutant=2.4  $\mu\text{m}/\text{min}$ , movie #: control=5, mutant=4, p=0.17). In schematics, macrophages are shown in red and  
171 analyzed macrophages in light blue, the ectoderm in green, the mesoderm in purple, and the yolk in beige.  
172 Macrophage nuclei visualized by *srpHemo-H2A::3xmCherry* expression. See also **Fig. S1** and **Videos 1** and **2**.  
173 Throughout this work, embryos were staged based on germband retraction away from the anterior of less than  
174 29% for stage 10, 29%-31% for stage 11, and 35%–40% for stage 12. In all figures and histograms show  
175 mean $\pm$ SEM and ns=p>0.05, \*p<0.05, \*\*p<0.01, \*\*\*p<0.001, \*\*\*\*p<0.0001. One-way ANOVA with Tukey for  
176 (D-E), and unpaired t-test for (G-L). Scale bars: 50  $\mu\text{m}$  in (A-C), 30  $\mu\text{m}$  in (F).  
177 See also **Figure S1** and **Videos 1** and **2**: representative movies of macrophage migration into the germband in  
178 the control (**Video 1**) and the *CG9005<sup>PBG</sup>* (*atos*) mutant (**Video 2**). Macrophages (red) are labeled  
179 with *srpHemo-H2A::3xmCherry*. Arrow indicates first macrophage moving into the germband. The time  
180 interval between each acquisition is 40 s and the display rate is 15 frames/s. Scale bar: 20  $\mu\text{m}$ .

181  
182  
183 mutant completely restored their capacity to invade the germband (Figs. 1C-D). Depleting  
184 *CG9005* by driving any one of three independent RNA interference (RNAi) lines in  
185 macrophages caused a 37-40% decrease in macrophages within the germband compared to  
186 controls (Fig. 1E). We also observed 24-27% more macrophages sitting on the yolk near the  
187 entry site that have not yet invaded the germband in *CG9005<sup>PBG</sup>* (Fig. S1A) and in the RNAi



188 lines (Fig. S1B) compared to their controls. This finding supports the conclusion that  
189 macrophages in these backgrounds migrate normally up to the germband but are less able to  
190 enter. We counted macrophages migrating along the ventral nerve cord (vnc) in late Stage 12  
191 embryos, a route guided by the same factors that lead into the germband (Brückner et al.,  
192 2004; Cho et al., 200; Wood et al., 2006) but that does not require tissue invasion (Siekhaus  
193 et al., 2010; Weavers et al., 2016). There was no significant difference in both the  
194 *CG9005<sup>PBG</sup>* mutant (Fig. S1C) and the *CG9005* RNAi-expressing macrophages (Figs. S1D-F)  
195 compared to their controls, arguing that basic migratory processes and recognition of  
196 chemotactic signals are unperturbed. Moreover, we detected no significant change in the total  
197 number of macrophages for any of these genotypes (Figs. S1G-H). Taken together, these  
198 results from fixed embryos clearly suggest that *CG9005* is specifically required in  
199 macrophages for the early steps of germband invasion.

200

### 201 **Atossa (*CG9005*) promotes efficient invasion of pioneer macrophages into the** 202 **germband tissue**

203 To directly assess *CG9005*'s role in germband invasion, we conducted two-photon live  
204 imaging. We labeled macrophages with the nuclear marker *srpHemo-H2A::3xmCherry* in  
205 control and *CG9005<sup>PBG</sup>* embryos (Figs. 1F and S1I, Videos 1 and 2). We observed no  
206 significant change in speed or directionality during macrophage migration from their initial  
207 position at Stage 9 in the head mesoderm up to the yolk neighboring the germband entry  
208 point in *CG9005<sup>PBG</sup>* (Fig. 1G, Figs. S1J-L) (speed in the head and yolk: 2.2  $\mu\text{m}/\text{min}$  for both  
209 the control and *CG9005<sup>PBG</sup>*;  $p=0.65$ ,  $p=0.78$  respectively), nor in their directionality within  
210 these regions (directionality: 0.39 in control and 0.37 in mutant in both regions,  $p=0.74$  for  
211 head,  $p=0.86$  for yolk). We also observed no significant change in migration speed for  
212 macrophages moving between the yolk and ectoderm (control=2.6 and *CG9005<sup>PBG</sup>*=2.5  
213  $\mu\text{m}/\text{min}$ ,  $p=0.62$ ) (Fig. 1H). However, the first macrophage in *CG9005<sup>PBG</sup>* required 65%  
214 more time than the control to enter into the germband tissue (time to entry: control=23 min  
215 and *CG9005<sup>PBG</sup>*=38 min,  $p<0.0001$ ) (Fig. 1I). The speed of the first two pioneering  
216 macrophages is also significantly slower as they invade along the path between the mesoderm  
217 and ectoderm in *CG9005<sup>PBG</sup>* mutant embryos compared to the control (1<sup>st</sup> cell: control=2.5  
218 and *CG9005<sup>PBG</sup>*=2  $\mu\text{m}/\text{min}$ ,  $p=0.012$ ; 2<sup>nd</sup> cell: control=2.9 and *CG9005<sup>PBG</sup>*=2.1  $\mu\text{m}/\text{min}$ ,  
219  $p=0.03$ ) (Figs. 1J-K). However, the speed of the next few cells migrating along this path was  
220 not affected (3<sup>rd</sup>-5<sup>th</sup> cells: control=2.5 and *CG9005<sup>PBG</sup>*=2.4  $\mu\text{m}/\text{min}$ ,  $p=0.17$ ) (Fig. 1L). We  
221 conclude that *CG9005* specifically regulates tissue invasion, facilitating the initial entry into  
222 and subsequent movement within the germband tissue of the first two pioneer macrophages.  
223 Since the macrophage stream invading the germband becomes a trickle in *CG9005<sup>PBG</sup>* we  
224 named the gene *atossa* (*atos*), for the powerful Persian queen whose name means trickling.

225

226

### 227 **Atossa (*CG9005*) is a nuclear protein whose conserved motifs and TADs are important** 228 **for macrophage tissue invasion, a function conserved by its vertebrate orthologs**

229 *Atossa* (*Atos*) contains a conserved domain of unknown function (DUF4210) and a  
230 Chromosome segregation domain (Chr\_Seg) (Fig. 2A). *Atos* also displays two trans-  
231 activating domains (TADs) common among transcription factors as well as three nuclear

232 localization signals (NLS) and a nuclear export signal (NES). We first tested the subcellular  
233 distribution of the Atos protein, transfecting the macrophage-like S2R+ cell line with a  
234 *FLAG::HA* tagged form of *atos* under the control of the macrophage promoter *srpHemo*. We  
235 found Atos mainly in the nucleus colocalized with DAPI, and also partially in the cytoplasm  
236 (Fig. S2A). When expressed *in vivo* in macrophages, Atos is also predominantly a nuclear  
237 factor (Fig. 2B). To assess the importance of the conserved domains and TADs, we made  
238 versions of Atos lacking these regions. All mutant forms were present in the nucleus similarly  
239 to wild-type Atos (Fig. S2A). While expression of wild-type Atos in the macrophages of *atos*  
240 embryos completely rescues germband invasion (Figs. 2C-D), Atos lacking either the  
241 conserved DUF2140, the Chr\_Seg domain, or either or both of the two TAD motifs failed to  
242 do so (Figs. 2D, S2B-C). Consistent with a germband invasion defect, expression of these  
243

244 **Figure 2. CG9005/Atossa requires conserved domains linked to transcriptional activation to enhance**  
245 **tissue invasion, a function maintained by its mammalian orthologs.**

246 **Fig 2A.** Deduced protein structure of *Drosophila* CG9005/Atossa (Atos) and its murine orthologs, mFAM214A  
247 and B. These proteins all contain the same conserved motifs: a domain of unknown function (DUF4210), a  
248 domain associated with Chromosome segregation (ChromSeg), at least one transcriptional activation domain  
249 (TAD), nuclear localization signal (NLS) and nuclear export signal (NES). FAM214A and B are 44-45%  
250 identical to Atos. **Fig 2B.** Macrophages (red) near the germband in Stage 11/12 embryos display colocalization  
251 of Atos tagged with HA (HA antibody, green) with the nucleus stained by DAPI (blue). *srpHemo-atos::H2A*  
252 line utilized. **Fig 2C.** Representative confocal images of Stage 12 embryos from the control, *atos<sup>PBG</sup>*, and  
253 *atos<sup>PBG</sup>* expressing Atos itself or variants lacking particular domains in macrophages. **Fig 2D.** Germband  
254 macrophage quantification in control, *atos<sup>PBG</sup>*, and *atos<sup>PBG</sup>* expressing Atos or its altered forms in macrophages.  
255 The tissue invasion defect in *atos<sup>PBG</sup>* can be fully rescued by Atos expression in macrophages unless Atos lacks  
256 the conserved DUF4210, ChrSeg, or TADs. Control n=32, mutant n=56, WT rescue n=18, DUF4210<sup>-</sup> rescue  
257 n=17, ChrSeg<sup>-</sup> rescue n=21, DUF4210/ChrSeg<sup>-</sup> rescue n=19, TAD1/TAD2<sup>-</sup> rescue n=25. For control vs mutant  
258 p<0.0001, for control vs rescue p=0.99, for mutant vs rescue p=0.0014. **Fig 2E.** Representative confocal images  
259 of *atos<sup>PBG</sup>* rescued with a murine ortholog, *mFAM214A* or *mFAM214B*, expressed in macrophages. **Fig 2F.**  
260 Quantification of macrophages in the germband in Stage 12 embryos from the control, *atos<sup>PBG</sup>*, and *atos<sup>PBG</sup>*  
261 embryos expressing *mFAM214A* or *mFAM214B* in macrophages shows that Atos's mammalian orthologs can  
262 rescue *atos*'s macrophage tissue invasion defect. Control n=25, *atos<sup>PBG</sup>* n=56, rescue with *atos* n=18, with  
263 *mFAM214A* n=22, with *mFAM214B* n=25. For control vs *mFAM214A* and *mFAM214B* rescues p>0.05, for  
264 *atos<sup>PBG</sup>* vs *mFAM214A* and *mFAM214B* rescues p<0.005. *mFAM214A* or *B* are expressed under the direct  
265 control of the *srpHemo* promoter. Throughout paper > indicates *GAL4 UAS* regulation. In (C) and (E)  
266 macrophages (red) are visualized by *srpHemo-H2A::3xmCherry* expression and actin by Phalloidin staining  
267 (green). One-way ANOVA with Tukey for (D) and (F). Scale bars are 5 μm in (B) and 50 μm in (C) and (E).  
268 See also **Figure S2**.

270 Atos mutants led to a higher number of macrophages sitting on the yolk at the germband  
271 entry site prior to invasion than in the rescue with wild-type Atos (Fig. S2D). These data  
272 clearly show that the conserved domains and TADs are critical for the primarily nuclear  
273 protein, Atos, to facilitate macrophage invasion.

275 Atos's uncharacterized murine orthologs, mFAM214A and mFAM214B, maintain these  
276 domains, displaying 40% identity to their *Drosophila* counterpart (Fig. 2A). Expression in  
277 macrophages of either mFAM214A or B in *atos<sup>PBG</sup>* rescued the germband invasion defect as  
278 efficiently as the *Drosophila* protein itself (Figs. 2E-F) and restored the normal number of  
279 macrophages on the yolk next to the extended germband (Fig. S2E). Therefore, we conclude  
280 that the molecular functions that enable Atos to promote macrophage tissue invasion are  
281 maintained in vertebrates.

282

283 **Atos raises mRNA levels of an RNA helicase and metabolic enzymes, which are each**  
284 **required for germband invasion**

285 Given Atos's nuclear localization and requirement for TADs, we hypothesized that Atos  
286 might modulate transcription in macrophages to aid their initiation of germband invasion. To  
287 identify potential targets, we performed RNA-sequencing analysis on FACS isolated  
288 macrophages from wild type and *atos<sup>PBG</sup>* embryos during germband invasion in early Stages  
289 11-12 (Fig. S3A) (Supp. Data 1). Transcriptome analysis revealed 25 genes with reduced  
290 mRNA levels and 39 genes with higher ones in the absence of Atos, requiring a P value<0.05  
291 (Fig. S3B). Gene ontology analysis (GO term) indicates that the significantly downregulated  
292 genes are involved in oxidation-reduction (redox) processes, stress responses as well as the  
293 nervous system (Fig. S3C). We therefore conclude that the presence of Atos in macrophages  
294 controls the mRNA levels of a small set of proteins.

295 We tested the hypothesis that the *atos<sup>PBG</sup>* macrophage germband invasion defect is caused by  
296 the lower levels of the downregulated genes. We focused only on the 5 genes that had at least  
297 a >5-fold change in expression and were enriched in embryonic macrophages or had an  
298 identified molecular function (Fig. 3A). We expressed *RNAi* constructs against them in  
299 macrophages and observed a significant reduction in germband macrophage numbers for three  
300 of these 5 candidates (Figs. 3B-G, S3D-E). For all three we also observed an increase in the  
301 number of macrophages sitting on the yolk next to the germband before invasion, consistent  
302 with a specific defect in germband invasion (Figs. S3F-H). These were a predicted ATP-  
303 dependent RNA helicase (CG9253) we name Porthos (Pths) (Martin et al., 2021) (Figs. 3B,  
304 E), and two metabolic enzymes, Glyoxylate Reductase/Hydroxypyruvate Reductase  
305 (*dGR/HPR*, CG9331) (Figs. 3C and 3F) and Lysine α-Ketoglutarate Reductase/Saccharopine  
306 Dehydrogenase (*dLKR/SDH*, CG7144) (Figs. 3D, G). Downregulation of *Glycerophosphate*  
307 *oxidase 2* (*Gpo2*, CG2137) (Fig. S3D) and *Golgi matrix protein 130 kD* (*GM130*, CG11061)  
308 (Fig. S3E) did not produce any invasion defect. GR/HPR is highly conserved from bacteria to  
309 mammals and the *Drosophila* form shows 48% identity to its human ortholog (NCBI

310  
311 **Figure 3. Atos leads to higher mRNA levels of an RNA helicase and metabolic enzymes required for**  
312 **germband invasion.**

313 **Fig 3A.** A selection of genes down-regulated in *atos<sup>PBG</sup>* mutant macrophages compared to the control, chosen  
314 for having a >5 fold change in expression as well as an identified biological function. **Fig 3B-D.** Representative  
315 confocal images of early Stage 12 embryos from the control, and lines expressing an *RNAi* against **(B)** *porthos*,  
316 **(C)** *dGR/HPR* or **(D)** *dLKR/SDH* specifically in macrophages (red). *srpHemo-H2A::3XmCherry* labels  
317 macrophages. **Fig 3E.** Quantification of Stage 12 embryos reveals that expression of a *porthos RNAi* in  
318 macrophages decreases their number in the germband by 48%. Control n=36, *porthos RNAi* (BL36589) n=28,  
319 p<0.0001. **Fig 3F-G.** Quantification of Stage 12 embryos indicates that fewer macrophages have moved into the  
320 germband upon the expression in macrophages of any of **(F)** three different *RNAi*s against *dGR/HPR* or **(G)** two  
321 different *RNAi*s against *dLKR/SDH*, arguing that these metabolic enzymes are required in macrophages for  
322 tissue invasion. Control 1 n=18, *dGR/HPR RNAi 1* (VDRC 44653) n=18, p<0.0001, control 2 n=21, *dGR/HPR*  
323 *RNAi 2* (VDRC 107680) n=24, p<0.0001, control 3 n=15, *dGR/HPR RNAi 3* (VDRC 64652) n=23, p=0.08.  
324 *dLKR/SDH RNAi 1* (VDRC 51346) n=17, control 2 n=21, *dLKR/SDH RNAi 2* (VDRC 109650) n=23, p<0.0001.  
325 **Fig 3H.** Schematic illustrates how the bifunctional enzyme dGR/HPR can catalyze the reduction of glyoxylate  
326 into glycolate and convert hydroxypyruvate into D-glycerate by oxidation of the cofactor NAD(P)H. **Fig 3I.**  
327 Schematic shows the metabolic pathway in which *Drosophila* Lysine  $\alpha$ -Ketoglutarate Reductase/Saccharopine  
328 Dehydrogenase (*dLKR/SDH*) catalyzes the first two steps of the lysine catabolism pathway, resulting in the  
329 production of glutamate and acetyl-CoA, a TCA substrate, through several downstream enzymatic reactions.  
330 Glu: Glutamate,  $\alpha$ -KG:  $\alpha$ -Ketoglutarate, AASA:  $\alpha$ -Amino adipate  $\delta$ -semialdehyde. Unpaired t test for **(E-G)**.  
331 Scale bar: 50  $\mu$ m in **(B-D)**. See also **Figure S3** and **Data S1**. **Data S1:** Annotated primary and normalized RNA  
332 sequencing data from FACS sorted control and *atos* macrophages.

333

334 BLAST). GR/HPR is the linchpin of the glyoxylate cycle, catalyzing the reduction of  
335 glyoxylate into glycolate and the conversion of hydroxypyruvate into D-glycerate (Fig. 3H)  
336 (Booth et al., 2006). This contributes to glucose and urea synthesis. The bifunctional  
337 enzyme dLKR/SDH is also highly conserved, with 71% identity to its human counterpart  
338 (identified by NCBI BLAST). It catalyzes the first two steps of lysine catabolism and can  
339 participate in the production of Acetyl CoA (Bhattacharjee, 1985) (Fig. 3I). We therefore  
340 conclude that Atos enhances macrophage tissue invasion by increasing the levels of the  
341 metabolic enzymes dLKR/SDH and dGR/HPR and the helicase ortholog Porthos.

342

### 343 **The nuclear RNA helicase, Porthos, functions downstream of Atos in pioneer** 344 **macrophages to allow their initiation of germband invasion**

345 Atos's target *porthos* (CG9253) displayed the strongest invasion defect upon RNAi  
346 knockdown (KD) (Fig 3E). Porthos is a conserved DEAD-box RNA helicase (Fig. S4A)  
347 sharing 71% identity and 84% similarity with its human ortholog, the helicase DDX47,  
348 including the conserved DEAD motif and helicase C terminal domain, with which DDX47  
349 interacts with RNA structures. *porthos* is expressed in the embryo by *in situ* analysis in a  
350 pattern similar to *atos* but a few stages later, to *atos* in *Drosophila* embryos, being enriched  
351 in macrophages in the head region during Stages 9-12 ([https://insitu.fruitfly.org/cgi-](https://insitu.fruitfly.org/cgi-bin/ex/report.pl?ftype=1&ftext=FBgn0032919)  
352 [bin/ex/report.pl?ftype=1&ftext=FBgn0032919](https://insitu.fruitfly.org/cgi-bin/ex/report.pl?ftype=1&ftext=FBgn0032919)). In S2R+ cells, HA-tagged Porthos  
353 colocalized with markers for the nucleus (DAPI) and the nucleolus (Fibrillarin), where  
354 ribosome assembly and rRNA processing occur (Fig. 4SB). In embryonic macrophages  
355 HA-tagged Porthos also localized to the nucleus, detected by DAPI (Fig. 4A).

356

### 357 **Figure 4. The nucleolar RNA helicase, Porthos, acts as a key downstream target of Atos to promote** 358 **pioneer macrophage germband invasion.**

359 **Fig 4A.** Macrophages (red) near the germband in Stage 11/12 embryos show partial colocalization of the HA  
360 antibody labeling Porthos (green) with the nucleus stained by DAPI (blue). Embryo express *srpHemo-*  
361 *porthos::HA*. **Fig 4B.** Stills starting at Stage 11 from two-photon movies of control embryos and those  
362 expressing *porthos RNAi* in macrophages; stills show macrophage migration from the head mesoderm towards  
363 and into the germband at the indicated time points. White dotted line indicates the germband edge. Macrophage  
364 nuclei labeled by *srpHemo-H2A::3xmCherry*. *UAS-porthos RNAi* (BL36589) expressed by *srpHemo-GAL4*. **Fig**  
365 **4C-H.** Quantification of macrophage migration parameters from two-photon movies. **(C-D)** Macrophages  
366 expressing *porthos RNAi* migrate with a similar speed in the head and between the yolk sac and the germband  
367 edge compared to the control. Speed in head: control=2.01  $\mu\text{m}/\text{min}$ , *porthos RNAi*=2.09  $\mu\text{m}/\text{min}$ ; movie #:  
368 control=4, *porthos RNAi*=6; track #: control=507, *porthos RNAi*=859,  $p=0.56$ . Speed between yolk sac and  
369 germband mesoderm: control=2.17  $\mu\text{m}/\text{min}$ , *porthos RNAi*=2.41  $\mu\text{m}/\text{min}$ ,  $p=0.45$ ; movie #: control n=5, *porthos*  
370 *RNAi* n=5, track #: control n=40, *porthos RNAi* n=51. **Fig 4E.** The time required for the first macrophage  
371 nucleus to enter into the germband is significantly increased in embryos expressing *porthos RNAi* compared to  
372 the control. Control=21.5 min, n=6, *porthos RNAi*=36.2 min, n=4,  $p<0.0001$ . Blue arrow in schematic indicates  
373 route analyzed. **Fig 4F-G.** The speed of the first and second macrophage invading into the germband along the  
374 path between the mesoderm and ectoderm is significantly slower in embryos expressing *porthos RNAi*  
375 compared to the control. First macrophage speed: control=2.99 and *porthos RNAi*=2.0  $\mu\text{m}/\text{min}$ ;  $p=0.009$ ; #  
376 movies: control n=4, *porthos RNAi* n=4. Second macrophage speed: control=2.61 and *porthos RNAi*=1.98  
377  $\mu\text{m}/\text{min}$ ;  $p=0.037$ ; # movies: control n=6, *porthos RNAi* n=4. **Fig 4H.** The speed of the third to fifth  
378 macrophages invading the germband is similar in macrophages downregulated for *porthos* and the control  
379 (speed: control=2.66 and *porthos RNAi*=2.31  $\mu\text{m}/\text{min}$ ;  $p=0.21$ ; # movies: control n=5, *porthos RNAi* n=4). **Fig**  
380 **4I.** Representative confocal images of early Stage 12 embryos from control, *atos<sup>PBG</sup>*, and *atos<sup>PBG</sup>* expressing  
381 *atos::FLAG::HA* or *porthos::FLAG::HA* in macrophages (red) through *srpHemo-GAL4* control of UAS  
382 constructs. Embryo detected by phalloidin staining (green). **Fig 4J.** Quantification of macrophages in the  
383 germband shows that the *atos<sup>PBG</sup>* mutant phenotype can be substantially rescued by expressing  
384 *porthos::FLAG::HA* in macrophages. Control (n=15), *atos<sup>PBG</sup>* (n=22), *atos<sup>PBG</sup>* with *srpHemo>atos::FLAG::HA*



385 (n=27), *srpHemo>porthos::FLAG::HA* (n=30). For control vs *atos<sup>PBG</sup>*  $p < 0.0001$ , for control vs *atos* rescue of  
386 *atos<sup>PBG</sup>*  $p < 0.0001$ , for control vs *porthos* rescue of *atos<sup>PBG</sup>*  $p = 0.0007$ . Macrophages detected by cytoplasmic  
387 *srpHemo-3xmCherry* in (A) and nuclear *srpHemo-H2A::3xmCherry* in movies and in (I). Unpaired t test for (C-  
388 H), and one-way ANOVA with Tukey for (J). Scale bars: 50  $\mu\text{m}$  in (A) and 30  $\mu\text{m}$  in (B).

389 See also **Figure S4** and **Videos 3** and **4**. Representative movies of macrophage migration into the germband in  
390 the control (**Video 3**) and the *porthos RNAi* embryos (**Video 4**). Macrophages (red) are labeled with *srpHemo-*  
391 *H2A::3xmCherry*. Arrow indicates first macrophage moving into the germband. The time interval between each  
392 acquisition is 40 s and the display rate is 15 frames/s. Scale bar: 20  $\mu\text{m}$ .

---

393

394 To determine at which step in macrophage germband invasion Porthos is needed, we  
395 examined wild type embryos and those expressing *porthos* RNAi in macrophages. In fixed  
396 embryos we observed no change in migration along the non-invasive route of the vnc (Fig.  
397 S4C) or in the total number of macrophages compared to the control (Fig. S4D), arguing  
398 that Porthos is specifically required for migration into or within the tissues of the  
399 germband. We then utilized 2-photon imaging of live embryos and tracked macrophages as  
400 they moved from their initial position within the head towards the germband and then  
401 during their infiltration into this tissue (Videos 3-4, Fig. 4B and 4SE). We observed no  
402 significant change in speed or directionality in the head or on the yolk (Fig. 4C, Fig S4F-H)  
403 (speed: in head, 2  $\mu\text{m}/\text{min}$  for control and *porthos RNAi*,  $p = 0.56$ , and on yolk, control=2.1  
404 and *porthos RNAi*=2.2  $\mu\text{m}/\text{min}$ ,  $p = 0.35$ ; directionality: in head, control=0.35 and *porthos*  
405 RNAi=0.37,  $p = 0.27$ , and on yolk, control=0.42 and *porthos RNAi*=0.39,  $p = 0.58$ ).  
406 Moreover, we detected no significant change in the speed of macrophages moving on the  
407 yolk and beneath the germband beyond the entry point (control=2.2 and *porthos RNAi*=2.4  
408  $\mu\text{m}/\text{min}$ ,  $p = 0.45$ ) (Fig. 4D). However, *porthos RNAi* macrophages waited 69% longer than  
409 the control to enter the germband tissue, (control=21.5 and *porthos RNAi*=36.3 min,  
410  $p < 0.0001$ ) (Fig. 4E). Once within the germband, the first two macrophages invading  
411 between the mesoderm and ectoderm progressed significantly slower than the control (Fig.  
412 4F-G) (1<sup>st</sup> cell: control=3.0 and *porthos RNAi*=2.0  $\mu\text{m}/\text{min}$ ,  $p = 0.009$ , 2<sup>nd</sup> cell: control=2.6  
413 and *porthos RNAi*=2.0  $\mu\text{m}/\text{min}$ ,  $p = 0.037$ ). In contrast, the speed of the subsequent  
414 macrophages was not significantly altered by *porthos RNAi* (Fig. 4H) (3<sup>rd</sup>-5<sup>th</sup> cells:  
415 control=2.7 and *porthos RNAi*=2.3  $\mu\text{m}/\text{min}$   $p = 0.21$ ). Thus, *porthos RNAi* phenocopies  
416 *atos*'s migration defect. Finally, we expressed Porthos in *atos<sup>PBG</sup>* to restore its higher levels  
417 in macrophages. This strongly improves the *atos* mutant phenotype (87% rescue) (Figs. 4I-  
418 J). Thus, we conclude that Porthos is a key player downstream of Atos, exerting an  
419 essential role in pioneer macrophages to specifically allow their initiation of germband  
420 invasion.

421

#### 422 **Porthos alters translation of a subset of mRNAs**

423 Given the helicase Porthos's nucleolar localization we hypothesized that it might modulate  
424 translation. We purified ribosomes and polysomes by sucrose density gradient fractionation  
425 of the control and S2R+ cells treated with *porthos* dsRNA (Fig. 5A). We observed a  
426 reduction in polysomes, the 40S small subunit, and 80S ribosome fraction (Fig. 5B) along  
427 with an increase in the large 60S subunit peak in the *porthos* KD. This data suggests that  
428 Porthos is required for normal levels of 40S biogenesis, ribosome and polysome assembly,  
429 and supports the idea that the higher levels of Porthos triggered by Atos could affect mRNA  
430 translation.



431

432 **Figure 5. Porthos increases translation of an mRNA subset including many involved in mitochondrial**  
433 **OxPhos and metabolic processes. Fig 5A.** Sucrose density gradient fractionation allowed purification of  
434 ribosome subunits and polysomes. Polysomal or total cellular mRNA fractions were isolated following dsRNA  
435 treatment and RNA sequencing libraries were prepared. **Fig 5B.** Sedimentation analysis showing the relative  
436 abundance of 40S, 60S, and 80S ribosomes indicates that *porthos* depletion by dsRNA markedly reduces the  
437 ratio of polysomes to monosomes. A non-targeting dsRNA was used as a control. Profiles were aligned on the  
438 basis of the 40S ribosome peak's position and labeled with distinct colors, black for control and red for *porthos*  
439 KD, n=3 biological replicates. **Fig 5C.** Scatter plot of Translational efficiency (TE) values from *porthos dsRNA*  
440 S2R+ vs control *gfp dsRNA* cells. Red (down-regulated, DR) and green (up-regulated, UP) dots represent genes  
441 with log<sub>2</sub> TE changes that meet the 2 standard deviation cutoff. **Fig 5D.** DR mRNAs in *porthos dsRNA* treated  
442 versus Control *dsRNA* treated S2R+ cells. 71% of the genes encoded proteins with predicted functions, the  
443 number corresponding to a functional category is shown. Proteins involved in mitochondrial-related functions,  
444 metabolic processes, and redox processes are highlighted. **Fig 5E.** Porthos modulates the translation of RNAs  
445 encoding components of mitochondrial OxPhos, including subunits of mitochondrial complexes III, and the  
446 ATP synthase complex V along with assembly factors for complexes I and IV. Porthos also enhances the TE of  
447 mitochondrial transporting channels, structural proteins as well as those involved in mitochondrial translation.  
448 **Fig 5F.** List of the proteins encoded by mRNAs that are downregulated in *porthos dsRNA* treated S2R+ cells  
449 that are involved in metabolic pathways. NF: Not Found. See also **Figure S5** and **Data S2**. **Data S2:** Complete  
450 set of TE values from polysome-sequencing data from control *gfp dsRNA* and *porthos dsRNA* treated S2R+ cells.

451

452 To examine which mRNA transcripts depend on Porthos for their efficient translation, we  
453 performed polysome-profiling, sequencing transcripts associated with highly translationally  
454 active polysomes as well as all the transcripts in the S2R+ cells (Fig 5A, Supp. Data 2). We  
455 calculated translational efficiency (TE) as the ratio of the normalized reads present for each  
456 gene in the mRNAs from the polysome fraction to those in the total mRNA levels; this ratio  
457 was determined for the data from both the control *GFP RNAi* and *porthos KD* cells. We  
458 plotted the mean TE values for control (*GFP KD*) and *porthos KD* replicates and calculated  
459 the mean change in TE ( $\Delta$ TE) for each gene as the ratio of TEs between control (*GFP KD*)  
460 and *porthos KD* replicates (Fig. 5C). Targets were defined as genes falling 2 standard  
461 deviations from the median  $\Delta$ TE as previously described (Flora et al., 2018). We identified  
462 204 annotated coding genes that were less efficiently translated and 102 that were more  
463 efficiently translated in *porthos KD* cells.

464 The mRNA targets whose TE Porthos enhances are involved in respiration,  
465 transport and translation in mitochondria, metabolic processes, transcription, translation,  
466 signal transduction, immune responses as well as redox processes (Fig. 5D-F, Fig. S5A-B).  
467 The targets include several components of mitochondrial OxPhos, namely ubiquinol  
468 cytochrome C reductase (complex III, UQCR-Q), ATP synthase subunit G and coupling  
469 factor F(o) (complex V), predicted assembly factors for complex I and IV, and proteins  
470 involved in mitochondrial translation and transport (Fig. 5E) as well as other metabolic  
471 pathways (Fig. 5F).

472

### 473 **Porthos is required for mitochondrial oxidative respiration and energy production**

474 Mitochondria generate ATP through OxPhos mostly from the pyruvate formed by the  
475 glycolytic pathway (Pavlova and Thompson, 2016; Vander Heiden et al., 2009) (Fig. S6A)  
476 and thus can utilize metabolites downstream of the two enzymes we identified as Atos  
477 targets, LKR/SDH and GR/HPR. To directly investigate if Porthos regulates mitochondrial  
478 energy production, we generated S2R+ cells producing 56% of *porthos's* normal mRNA  
479 levels with CRISPR/Cas9-mediated mutagenesis (which we call *porthos-KD* cells) (Fig.

480 S6B). We then utilized a Seahorse assay in which the oxygen consumption rate (OCR)  
481 (Llufrio et al., 2018) is determined before and after sequential treatment with compounds  
482 affecting different steps in OxPhos (Figs. 6A, S6A). By comparing the OCR observed upon  
483 the different treatments we calculated OxPhos-dependent basal and maximum respiration  
484 and found that both were reduced 64% in *porthos-KD* (Figs. 6A-C) (see Methods). We also  
485 found significant decreases in OxPhos-dependent spare respiration capacity and as well as  
486 OxPhos-independent respiration (72% and 42% reduction, respectively) (Fig. 6C). S2R+  
487 cells utilize primarily mitochondrial OxPhos rather than glycolysis for ATP production  
488 (Freijie et al., 2012); this remains the case even in the *porthos KD* cells (Fig. S6C) as we  
489 also observed a 60% reduction in the basal extracellular acidification rate (ECAR), a  
490 measure of lactate production through complete glycolysis (Fig. S6D). In totality, ATP  
491 production through OxPhos was reduced by 50% upon *porthos* depletion (Fig. 6C). Given  
492 that Porthos modulates the translation of subunits of mitochondrial complex III and the  
493 ATP synthase complex V, our data argues that Porthos induces a shift in metabolic capacity  
494 and flux that contributes to the upregulation of the OxPhos pathway and higher levels of  
495 energy production.

496

#### 497 **Mitochondrial respiration is required for metabolism and energy production in** 498 **macrophages to initiate invasion into the germband tissue**

499 We sought to directly assess the importance of the OxPhos complexes whose TE is  
500 upregulated by Porthos for macrophage germband invasion in the embryo. Therefore, we  
501 tested the effect of a dominant negative form of *complex V*, the ATP synthase which  
502 converts the electron gradient produced during OxPhos into ATP (*CV-DN*) (Figs. 6D-F).  
503 We also expressed RNAis against different subunits of *complex III* and the  $\alpha$  subunit of  
504 *complex V* in macrophages (Figs. 6G-H). Consistent with the polysome-profiling results  
505 from *porthos-KD* S2R+ cells, these treatments significantly reduced macrophage numbers  
506 within the germband (Figs. 6D-H) and increased them on the yolk at the germband entry  
507 site (Figs. 6F, S6E), phenocopying the germband invasion defect of *atos<sup>PBG</sup>* or *porthos*  
508 *RNAi* in macrophages. We observed no significant difference in macrophage numbers on  
509 the vnc in late Stage 12 upon expression of *CV-DN* (Fig. S6F) or of the RNAis (Fig. S6G)  
510 compared to the control, indicating normal general migration. This data strongly supports  
511 the conclusion that higher levels of the OxPhos complexes III and V are required  
512 specifically for macrophage tissue invasion.

513

514 **Figure 6. Higher levels of mitochondrial respiration are required in macrophages to power their**  
515 **germband tissue invasion. Fig 6A.** Schematic of the procedure for mitochondrial energetic profiling in wild-  
516 type and *porthos KD* S2R+ cells with a Seahorse efflux assay. **Fig 6B.** The Oxygen Consumption Rate (OCR,  $\mu\text{mol O}_2/\text{min}$ ) was assessed as a representative parameter of OxPhos in control and *porthos KD* S2R+ cells by a  
517 Seahorse Bioscience XF96 Extracellular Flux Analyzer. The ATP synthase inhibitor oligomycin (2  $\mu\text{M}$ ), the  
518 uncoupler FCCP (2  $\mu\text{M}$ ), and the mitochondrial complex I inhibitor Rotenone (1  $\mu\text{M}$ ) with antimycin A (1  $\mu\text{M}$ )  
519 were injected sequentially (see S6A). **Fig 6C.** Calculation from relative OCR values at different stages assesses  
520 basal and maximum OxPhos respiration, spare OxPhos respiration capacity, OxPhos ATP production, and non-  
521 OxPhos respiration rates. At least three independent biological experiments ( $n > 6$  technical replicates in each  
522 repeat). **Fig 6D-E. (D)** Representative confocal images and **(E)** quantification of Stage 12 embryos reveals that  
523 the number of macrophages (red) that penetrated into the germband in Stage 12 embryos is significantly  
524 decreased upon the expression of a dominant negative c-ring of the ATP synthase (*CV-DN*) compared to the  
525 control. Control  $n=24$ , *CV-DN*  $n=20$ ,  $p=0.003$ . **Fig 6F.** Quantification of macrophages on the yolk in fixed early  
526 Stage 12 embryos shows a significant increase in the *CV-DN* embryos compared to the control. Control  $n=21$ ,  
527

528 *CV-DN* n=17, p=0.003. **Fig 6G-H.** (G) Representative confocal images and (H) quantification of Stage 12  
529 embryos indicates that fewer macrophages (red) move into the germband upon the expression in macrophages  
530 of any of three different *RNAi*s against mitochondrial OxPhos *Complex III* (*Ubiquinol-cytochrome c reductase*,  
531 *UQCR*), or an *RNAi* against *Complex V* (*F1F0*, *CG3612*), arguing that these two components are required in  
532 macrophages for germband tissue invasion. Control n=34; *Complex III* (*Cyt-c1*, *CG4769*): *RNAi 1* (VDRC  
533 109809) n=20, p=0.0001; *Complex III* (*UQCR-cp1*, *CG3731*): *RNAi 2* (VDRC 101350) n=18, p<0.0001;  
534 *Complex III* (*UQCR-cp2*, *CG4169*): *RNAi 3* (VDRC 100818) n=16, p=0.0027; *Complex V*: (*F1F0*, *CG3612*)  
535 *RNAi* (VDRC 34664) n=24, p<0.0001. **Fig 6I.** A single plane confocal microscope image during germband  
536 entry in early Stage 12 embryos from control (Ctrl) or *atos<sup>PBG</sup>* embryos, or lines expressing *porthos* *RNAi* or  
537 *CV-DN* in macrophages. Antibodies used against the phosphorylated at S293 and thus inactivated Pyruvate  
538 Dehydrogenase (pPDH, green) or total PDH (magenta) in macrophages (red). Higher pPDH levels are usually  
539 found when ATP/ADP levels are high and input into the TCA cycle is being downregulated (Patel et al., 2014).  
540 **Fig 6J.** Quantification of normalized values for pPDH/PDH levels calculated from fluorescence intensities in  
541 macrophages from the genotypes in (6I) during initial germband invasion in early Stage 12. The pPDH/PDH  
542 ratio is significantly reduced in all compared to the control, arguing that decreasing the function of CV, *atos* or  
543 *porthos* in macrophages results in lower cellular ATP/ADP ratios compared to the control. Control n=10, *CV-*  
544 *DN* n=9, p=0.0002; *atos<sup>PBG</sup>* n=13, level p=0.0002; control n=7, *macro>porthos RNAi* n=8, p=0.0002. Three  
545 independent experiments. Macrophages visualized in (C) and (G) with nuclear *srfHemo-H2A::3xmCherry*  
546 expression and (I) with cytoplasmic *srfHemo-3xmCherry*. Unpaired t test for (B-C), (E-F), and (H-J). Scale  
547 bars: 50  $\mu$ m in (D) and (G), 10  $\mu$ m in (I). See also **Figure S6**.  
548

549

## 550 **Atos and its target Porthos increase macrophage bioenergetics for germband tissue** 551 **invasion**

552 To examine the bioenergetic state of embryonic macrophages *in vivo* in the absence of  
553 Porthos or Atos, we first assessed the Pyruvate dehydrogenase complex (PDH), which allows  
554 pyruvate formed by glycolysis to feed into the TCA cycle. PDH is a key point of metabolic  
555 regulation (Patel et al., 2014) (see Fig. 7A). Metabolites produced by the TCA cycle increase  
556 PDH's phosphorylation thereby inhibiting it and thus the running of the cycle; metabolites  
557 utilized by the TCA cycle decrease PDH phosphorylation and activate it. Importantly, when  
558 energy levels fall and mitochondrial ADP levels rise, PDH is unphosphorylated and active,  
559 opening the gate to the TCA cycle and OxPhos (Patel et al., 2014). By antibody staining we  
560 determined the levels of phosphorylated inactive PDH (pPDH) and the total amounts of PDH  
561 (Lieber et al., 2019) in embryonic macrophages. We assessed the pPDH/PDH ratio; a smaller  
562 number indicates less inhibition and thus more activity of PDH. As a positive control we first  
563 examined macrophages expressing *CV-DN*, which blocks mitochondrial ATP synthase, and  
564 thus increases ADP levels. Indeed we observed a lower pPDH/PDH ratio than in the control  
565 (Fig. 6J). We also observed significantly lower pPDH/PDH ratios in macrophages invading  
566 the germband in *atos<sup>PBG</sup>* embryos as well as those expressing *porthos* *RNAi* in macrophages  
567 compared to the control (Figs. 6I-J). Our results support the conclusion that in the absence of  
568 Atos or Porthos, macrophages *in vivo* have reduced ATP/ADP ratios, leading the cells to  
569 keep PDH in its active form to try to generate more ATP by converting pyruvate into acetyl  
570 CoA that can feed into the TCA cycle.

571

## 572 **Atos enhances cellular metabolism and ATP/ADP levels**

573 To investigate the full complement of metabolic changes that Atos enables, we performed  
574 untargeted comparative metabolite profiling by capillary liquid chromatography-tandem mass  
575 spectrometry (LC-MS/MS) (Figs. S7A, 7A) characterizing extracts from control and *atos<sup>PBG</sup>*  
576 embryos. Most importantly, consistent with the results we had observed in the Seahorse assay

577 and the p-PDH/PDH ratio measurement, we observed a significantly decreased ATP/ADP  
578 ratio in the absence of Atos (Fig. 7B). Thus our metabolic data supports that Atos regulates a  
579 set of targets that shift metabolism to enhance ATP production. Consistent with Atos's role in  
580 increasing GR/HPR levels, in *atos<sup>PBG</sup>* we observed higher levels of this enzyme's substrate,  
581 4-hydroxy  $\alpha$ -ketoglutarate (4-H $\alpha$ KG) (Figs. S7B-C) and of hydroxy-L-proline (HLP), the  
582 metabolite just upstream of 4-H $\alpha$ KG (Fig. 7A). We also observed significantly higher levels  
583 of dipeptides containing HLP (Fig. 7D). Atos also regulates LKR/SDH; we observed a  
584 reduction to 60% of control levels of its product alpha-amino adipic semialdehyde (ASAA),  
585 by targeted-metabolomics profiling (Fig. 7A).

586

587 **Fig 7. Mitochondrial metabolism is enhanced by Atos and Porthos. Fig 7A.** Schematic depicting ATP-  
588 generating pathways in eukaryotic cells: glycolysis, the Pentose Phosphate Pathway (PPP), fatty acid  
589 oxidation (FAO), the TCA cycle, and the mitochondrial respiratory electron transport chain (ETC). Blue stars  
590 mark *porthos* targets. Green indicates individual metabolites with statistically significant upregulation in  
591 *atos<sup>PBG</sup>* compared to the control. **Fig 7B-F.** Cellular metabolites were measured by LC-MS-based  
592 metabolomics from extracts of Stage 11 embryos (Control n=5, *atos<sup>PBG</sup>* n=7). **Fig 7B.** Normalized ATP/ADP  
593 ratio values are decreased in *atos<sup>PBG</sup>* compared to control embryos. (p-value=0.028). **Fig 7C.** Quantification in  
594 *atos<sup>PBG</sup>* compared to wild-type embryos shows an increase in the pyruvate/glucose ratio (p-value=0.035), but  
595 none for the Lactate/Glucose ratio (p-value=0.65). **Fig 7D-F.** Heatmap of non-targeted metabolites in *atos<sup>PBG</sup>*  
596 compared to wild-type embryos shown with average log<sub>2</sub>fold change (FC) reveals **(D)** a significant increase in  
597 some dipeptides including those containing hydroxyproline, **(E)** increases in intermediates of mitochondrial  
598 fatty acid  $\beta$ -oxidation (FAO), including different carnitine-conjugated lipids, and **(E-F)** a significant increase  
599 in ketone body substituents compared to the control. \*p<0.05, \*\*p<0.01, \*\*\*p<0.001, \*\*\*\*p<0.0001. Values  
600 are obtained from untargeted metabolomic analysis in **(B, D-F)**. **Fig 7G.** Our model: Atos raises mRNA  
601 transcript levels of the helicase Porthos and the metabolic enzymes GR/HPR and LKR/SDH in macrophages.  
602 Metabolic pathways downstream of GR/HPR and LKR/SDH are known to produce metabolites that feed into  
603 glycolysis and the TCA cycle to produce ATP. Porthos enhances the translational efficiency of mRNAs,  
604 including those encoding mitochondrial OxPhos components and a mitochondrial carnitine transporter.  
605 Macrophages with elevated mitochondrial OxPhos can meet the demands for the energy needed to create a  
606 path for tissue invasion. However, the absence of Atos leads to reduced levels of GR/HPR, LKR/SDH and  
607 Porthos. This decreases generation of ATP through OxPhos leading to defective tissue infiltration of the  
608 pioneering macrophages. Unpaired t-test for **(B-F)**. See also **Figure S7** and **Data S3**. **Data S3:** Primary  
609 metabolomics data from control and *atos* mutant embryos.

610

611 As the metabolomics was conducted on embryos constitutively defective in Atos,  
612 we expected to see some compensatory changes as well. Matching our previous data, no  
613 indications of a metabolic shift away from mitochondrial OxPhos towards aerobic  
614 glycolysis in the absence of Atos were present (Figs. 7C, S7D-F). Instead we observed  
615 results consistent with a backup of some metabolites whose products would normally be  
616 fed into glycolysis and the TCA cycle. We found significantly higher levels of  $\beta$ -  
617 hydroxybutyrate, which can be broken down to acetyl-CoA (Puchalska and Crawford,  
618 2017) along with increases in carnitine-conjugated fatty acids (Figs. 7E-F). There were  
619 strong increases in thymidine, which can be catabolized to a product that is fed into  
620 glycolysis (Tabata et al., 2017), and uridine which can be interconverted with thymidine,  
621 along with other purine and pyrimidine nucleotides (Figs. S7G-H). We observed a small  
622 increase in most amino acids in *atos<sup>PBG</sup>* (Fig. S7I). Additionally strong reductions occurred



623 in the glycine-related metabolite sarcosine (N-methylglycine) known to be a biomarker of  
624 highly metastatic prostate cancer (Fig. S7J) (Sreekumar et al., 2009; Zhang et al., 2012).  
625 In sum, the metabolomics profiling data in combination with our other findings strongly  
626 supports the conclusion that Atos is a powerful regulatory protein, increasing the efficiency  
627 and amount of OxPhos by inducing a metabolic shift that affects the ETC and complex V  
628 as well as the TCA cycle (Fig. 7G).

629

## 630 **DISCUSSION**

631 We identify a key regulator of energy levels in *Drosophila* macrophages as a highly  
632 conserved and previously uncharacterized nuclear protein, that we name Atos. Atos mRNA is  
633 deposited maternally and is ubiquitously expressed at low levels. However Atos mRNA is  
634 also developmentally upregulated in macrophages several hours prior to tissue invasion and  
635 down regulated after invasion is completed. Live imaging shows that the presence of Atos  
636 speeds the tissue entry and forward movement within the germband tissue of only the first  
637 two macrophages, the invasion pioneers. RNA sequencing indicates that Atos leads to the  
638 upregulation in macrophages of mRNAs encoding two metabolic enzymes, dGR/HPR by 6.5-  
639 fold and dLKR/SDH by 25-fold, as well as a 10-fold increase in the mRNA encoding an  
640 ATP-dependent RNA helicase, named Porthos. Each of these three proteins is required for  
641 normal amounts of invasion. We show in S2R+ cells that two-fold higher levels of Porthos  
642 mRNA correspond to two-fold higher OxPhos activity, a process that generates ATP by  
643 transferring electrons from NADH and FADH<sub>2</sub> produced by the TCA cycle to oxygen  
644 (Martínez-Reyes and Chandel, 2020). We thus favor the hypothesis that these two metabolic  
645 enzymes act in pathways that ultimately feed into the TCA cycle and thus the ETC. We  
646 identify an increase in the active state of the PDH enzyme in *porthos* and *atos* mutant  
647 macrophages, an indirect indication that ATP could be lower without these proteins.  
648 Importantly, we directly detect two-fold lower ATP/ADP levels in *atos* mutant embryos.  
649 Given that Atos is much more highly expressed in macrophages at this stage than in the rest  
650 of the embryo, the effects within these immune cells will be even greater. In sum our data  
651 argues that the developmentally programmed upregulation of Atos triggers a metabolic shift  
652 by upregulating this triad of targets, ultimately significantly increasing ATP/ADP in all  
653 macrophages and thereby enabling pioneer macrophages to power the creation of a path for  
654 tissue infiltration against surrounding resistance. Our findings are consistent with previous  
655 work indicating that higher ATP levels are needed in the first cell to migrate through  
656 extracellular matrix (Kelley et al., 2019; Zhang et al., 2019). However, to our knowledge our  
657 work is the first to identify a concerted molecular pathway that can produce the higher energy  
658 levels needed to speed pioneer cell invasion.

659

660 The target of Atos that we have focused on in this study is a previously  
661 uncharacterized protein we call Porthos. Porthos belongs to a family of ATP-dependent  
662 DEAD-box RNA helicases that have essential roles in RNA metabolism (Martin et al., 2021,  
663 Bourgeois et al., 2016; Venema et al., 1997; Venema and Tollervey, 1995). We find Porthos  
664 localized to the nucleolus in macrophages, suggesting a function in ribosome production or  
665 assembly (Baßler and Hurt, 2019). Porthos' vertebrate ortholog, DDX47, binds rRNA  
666 precursors (Sekiguchi et al., 2006); its *S. cerevisiae* ortholog, RRP3, can separate short RNA



667 helices and is required for the RNA processing that produces the 18S rRNA component of the  
668 40S ribosomal subunit (O'Day et al., 1996; Garcia et al., 2012). Consistent with this in S2R+  
669 cells treated with *porthos* dsRNA we find a lower ratio of the 40S to the 60S ribosome  
670 subunits along with a strong decrease in multiple ribosomes sitting on an mRNA, called  
671 polysomes. Importantly, Porthos also enhances the translational efficiency (TE) of a subset of  
672 mRNAs. A significant subset of the mRNAs whose TE is enhanced by Porthos encode  
673 mitochondrial proteins. These are orthologs of proteins shown to affect many aspects of the  
674 organelle's biology, from its specialized translation, its import of proteins and their insertion  
675 into the inner membrane where the ETC resides, to its import of fatty acids as fuel. Some of  
676 these targets are also components directly involved in OxPhos. We identify two orthologs of  
677 proteins that affect the assembly and function of OxPhos complexes I and IV (Formosa et al.,  
678 2015; Dennerlein et al., 2015), one of which causes mitochondrial disease if mutated (Calvo  
679 et al., 2010). The yeast ortholog of the complex III subunit we identify as a target, QCR9, is  
680 required to strongly increase reductase activity (Brandt et al., 2017). We identify a protein  
681 whose ortholog has been implicated in ATP synthase function (Belogradov, 2002;  
682 Belogradov, 2008). Another, complex V subunit G, fosters complex dimerization, thereby  
683 contributing to cristae formation (Davies et al., 2011; Hahn et al., 2016), as does another  
684 target, Mics1 (Oka et al., 2008). More cristae correlate with higher levels of OxPhos (Brandt  
685 et al., 2017), and have been proposed to foster ATP production (Mannella, 2020). Thus the  
686 increased OxPhos we see in cells with more Porthos could result from improved efficiency  
687 through multiple avenues; more translation of Porthos targets would be predicted to increase  
688 the amount, localization, and assembly of OxPhos components as well as the extent of the  
689 membrane folds in which they are localized. Co-regulation to increase this set of  
690 mitochondrial proteins could thus allow a concerted enhancement of OxPhos and  
691 mitochondrial energy production by avoiding that individual steps become rate limiting.  
692 Atos's two mammalian orthologs, FAM214A and B, can fully substitute for Atos during  
693 macrophage invasion, arguing that they maintain Atos's ability to increase ATP/ADP. All of  
694 Atos's targets that we show act during invasion have highly conserved human orthologs  
695 whose mRNAs are broadly expressed along with FAM214A and B (Sekiguchi et al., 2006;  
696 Human Protein Atlas, BioGPS). Thus Atos's vertebrate orthologs could be utilized by  
697 particular mammalian cell types in energetically demanding circumstances. In the immune  
698 system FAM214A appears particularly enriched within plasmacytoid dendritic cells (pDCs)  
699 and B cells (Table 1); pDCs upregulate OxPhos in response to IFN-1s during anti-viral  
700 responses (Wu et al., 2016) and B cells upregulate OxPhos during differentiation for effective  
701 antibody secretion (Price et al., 2018). Furthermore, FAM214A and B are well expressed in  
702 the brain which utilizes large amounts of energy and produces almost all of its ATP through  
703 OxPhos (Raichle and Gusnard, 2002; Hall et al., 2012). A shift from aerobic glycolysis to  
704 OxPhos is required for neural stem cell differentiation and neural survival (Zheng et al.,  
705 2016); many neurodegenerative diseases are associated with defects in OxPhos (Koopman et  
706 al., 2013). Interestingly, four different single nucleotide polymorphisms (SNP) in FAM214A  
707 introns have been linked to more severe Alzheimer's disease or neurofibrillary tangles in  
708 genome wide association studies while another SNP in a transcription factor-binding region  
709 was associated with increased general intelligence (p-value for all variants  $\leq 5 \times 10^{-6}$ ;  
710 <https://www.ebi.ac.uk/gwas/search?query=FAM214A>), Sherva et al., 2020; Beecham et al.,

711 2014; Wang et al., 2020; Davies et al., 2018). The importance of OxPhos enhancers for brain  
712 function is demonstrated by the many neurodegenerative diseases connected to defects in  
713 PGC-1 (Zheng et al., 2010; Cui et al., 2006; Weydt et al., 2006). PGC-1 activates OxPhos  
714 through transcription of mitochondrial genes and thus mitochondrial biogenesis (Lin et al,  
715 2005). In contrast, Atossa increases translation from mitochondrial mRNAs that already exist  
716 by raising levels of the helicase Porthos. The closest *Drosophila* ortholog of PGC-1 also  
717 raises transcription of mitochondrial proteins and OxPhos (Tiefenbock et al., 2010) and is  
718 expressed in invading macrophages at levels comparable to Atossa in our RNAseq. We  
719 hypothesize that these two regulators of mitochondrial function could work in concert, with  
720 Atossa allowing faster and more easily reversible control of enhanced energy production.  
721 Thus investigating the mammalian version of the regulatory network that we identified in this  
722 work and strategies to modulate it in the brain and immune system is of wide interest.

723 Altogether, our work uncovers a surprising molecular genetic view into the  
724 physiology of the organism, revealing a heretofore unsuspected cross-regulatory mechanism  
725 that spans different levels of the biological organization of cellular metabolism, cell biology  
726 and the tissue invasiveness of the immune system.

727

## 728 **Acknowledgements**

729 We thank: The *Drosophila* Genomics Resource Center supported by NIH grant  
730 2P40OD010949-10A1 for plasmids, the Bloomington *Drosophila* Stock Center supported by  
731 NIH grant P40OD018537 and the Vienna *Drosophila* Resource Center (Dietzl et al., 2007)  
732 for fly stocks, FlyBase (Thurmond et al., 2019) for essential genomic information, and the  
733 BDGP *in situ* database for data (Tomancak et al., 2002; Tomancak et al., 2007). We thank the  
734 Vienna BioCenter Core Facilities for RNA sequencing and analysis and the Life Scientific  
735 Service Units at IST Austria for technical support and assistance with microscopy and FACS  
736 analysis. We thank C. Guet, C. Navarro and Siekhaus group members for discussions and  
737 comments on the manuscript. D.E.S. was funded by Marie Curie CIG 334077/IRTIM and  
738 Austrian Science Fund (FWF) grant ASI\_FWF01\_P29638S, P.R. by NIH/NIGMS  
739 (R01GM111779-06 and R01GM135628-01), and A.B. with support of the European  
740 Research Council (ERC) under the European Union’s Horizon 2020 research and innovation  
741 program, grant no. 677006, “CMIL”. T.R.H. is supported by the Natural Sciences and  
742 Engineering Research Council of Canada (RGPIN-2019-06766).

743

## 744 **Author Contributions**

745 S.E., E.T.M. A.G. J.B. J-W.G. and T.K. conducted experiments, T.R.H. and A.B. provided  
746 resources, S.E., T.R.H., J.B. J-W. A.G, T.K. P.R. and D.E.S. designed experiments, S.E.,  
747 E.T.M., and D.E.S. wrote the paper, S.E., E.T.M. and J-W.G. conducted formal analysis, all  
748 authors reviewed and edited the paper, A.B., D.E.S. and P.R. conducted Supervision and  
749 Project Administration, S.E., D.E.S. and P.R carried out Conceptualization. D.E.S., P.R. A.B.  
750 and T.R.H. acquired funding.

751

## 752 **Declaration of Interests**

753 The authors declare no competing interests.

754

755

## 756 **EXPERIMENTAL PROCEDURES**

757

### 758 **Fly work**

759 Flies were raised on food bought from IMBA (Vienna, Austria) which was prepared  
760 according to the standard recipe of agar, cornmeal, and molasses with the addition of 1.5%  
761 Nipagin. Adults were placed in cages in a Percival DR36VL incubator maintained at 29°C  
762 and 65% humidity or a Sanyo MIR-153 incubator at 29°C within the humidity controlled  
763 25°C fly room; embryos were collected on standard plates prepared in house from apple  
764 juice, sugar, agar and Nipagin supplemented with yeast from Lesaffre (Marcq, France) on the  
765 plate surface. Embryo collections for fixation (7-8 hour collection) as well as live imaging (4-  
766 5 hour collection) were conducted at 29°C.

767

### 768 **Fly lines obtained used in this work**

769 *srpHemo-GALA* was provided by K. Brückner (Brückner et al., 2004). The RNA lines tested  
770 in this paper (Table S1) were obtained from the Bloomington *Drosophila* Stock Centre  
771 (Bloomington, USA) and the Vienna *Drosophila* Resource Center (VDRC, Vienna, Austria).  
772 Lines  $w^{\bar{c}}$ ;  $P\{w[+mC] \textit{srpHemo-3xmCherry}\}$ ,  $w^{\bar{c}}$ ;  $P\{w[+mC] \textit{srpHemo-H2A::3xmCherry}\}$   
773 were published previously (Gyoergy et al., 2018).

774

### 775 **Embryo fixation and immunohistochemistry**

776 Embryos were collected on apple juice plates from between 6-8.5 hours at 29°C. Embryos  
777 were incubated in 50% Chlorox (DanClorix) for 5 min and washed. Embryos were fixed with  
778 17% formaldehyde/heptane (ThermoFisher Scientific, Waltham, MA, USA) for 20 min  
779 followed by methanol or ethanol devitellinization. PDH and p-PDH staining utilized hand-  
780 devitellinized embryos. Fixed embryos were blocked in BBT (0.1 M PBS + 0.1% TritonX-  
781 100 + 0.1% BSA) for 2 hours at RT and then incubated overnight at 4°C. Antibodies were  
782 used at the following dilutions: Mouse anti  $\alpha$ -GFP (Aves Labs Inc., Tigard, Oregon, 1:500),  
783 Rat anti-HA (Roche, Basel, Switzerland, 1:100), Mouse anti-PDH E1 $\alpha$  (Abcam, Cambridge,  
784 UK, ab110334, 1:200) and Rabbit antiphospho-PDH E1 $\alpha$  (S293) (Abcam, Cambridge, UK,  
785 ab92696, 1:200). Afterwards, embryos were washed in BBT for 2 hours, and incubated with  
786 secondary antibodies at RT for 2 hours, and washed again for 2 hours. Secondary antibodies  
787 and Phalloidin were used at the following dilutions: anti-rat 488 1:300, anti-chicken 488  
788 1:500, anti-mouse 488 1:500 or anti-mouse 633 1:200, anti-rabbit 488 1:300, and Phalloidin  
789 1:300 (all from ThermoFisher Scientific, Waltham, MA, USA) (Table S2). The embryos  
790 were mounted overnight at 4°C in Vectashield mounting medium (Vector Laboratories,  
791 Burlingame, USA), which contains DAPI. Embryos were placed on a slide and imaged with a  
792 Zeiss Inverted LSM800 Confocal Microscope using a Plain-Apochromat 20X/0.8 Air  
793 Objective or a Plain-Apochromat 63X/1.4 Oil Objective.

794

### 795 **S2R+ cell work and immunostaining**

796 S2R+ cells (a gift from Frederico Mauri of the Knöblich laboratory at IMBA, Vienna) were  
797 grown in Schneider's medium (Gibco) supplemented with 10% FBS (Gibco) and transfected  
798 with the *srpHemo-HA::CG9005(atos)*, or *UAS-CG9005(atos)::FLAG::HA*, *UAS-*

799 *CG9253(porthos)::FLAG::HA* and *srpHemo-GAL4* constructs using Effectene Transfection  
800 Reagent (Qiagen, Hilden, Germany) following the manufacturer's protocol (Table S3).  
801 Transfected S2R+ cells were grown on Poly-L-Lysine coated coverslips (ThermoFisher  
802 Scientific, Waltham, Massachusetts, USA) in complete Schneider's medium (Gibco)  
803 supplemented with 10% FBS (Sigma-Aldrich, Saint Louis, Missouri, USA) to a confluency  
804 of 60%. For antibody staining, cells were fixed with 4% paraformaldehyde (Sigma-Aldrich,  
805 St Louis, MI, USA) in PBS for 15 minutes at room temperature (RT). Cells were washed  
806 three times with PBS followed by permeabilization with 0.5% Triton X-100 (Sigma-Aldrich)  
807 in PBS for 15 minutes and then blocked in BBT (see above) for at least 1 hour. Antibodies  
808 were diluted in blocking buffer and incubated for 2 hours at RT. Primary antibodies were  
809 used at the following working dilutions: Chicken anti-GFP (clone 5G4, Ogris lab, MFPL,  
810 1:100), Rat anti-HA (Roche, Basel, Switzerland, 1:50), Mouse anti-Lamin (DSHB, lamin  
811 Dm0, ADL1010, 1:50), and Mouse anti-fibrillarin (gift from Rangan lab, 1:1). Cells were  
812 subsequently washed three times with PBS-Triton X-100 (0.05%) for 5 minutes each,  
813 followed by secondary antibody incubation in blocking/permeabilization buffer for 1 hour at  
814 RT. Secondary antibodies were used at the following working dilutions: anti-rat Alexa Flour  
815 488 (1:50), anti-mouse Alexa Flour 488 (1:200), and anti-mouse Alexa Flour 633 (1:100) (all  
816 from ThermoFisher Scientific, Waltham, MA, USA). Cells were counterstained with DAPI  
817 (ThermoFisher Scientific) for 10 minutes in PBS-Triton X-100 (0.05%). After  
818 immunoblotting, cells were mounted with Vectashield (Sigma-Aldrich). Images were  
819 acquired using the Zeiss inverted LSM-800 confocal microscope. Pictures were processed  
820 with ImageJ.

821

### 822 **DNA isolation from single flies**

823 Single male flies were frozen overnight before being grounded with a pellet homogenizer  
824 (VWR, Radnor, USA) and plastic pestles (VWR, Radnor, USA) in 50µl of homogenizing  
825 buffer (100 mM Tris-HCl, 100 mM EDTA, 100 mM NaCl, and 0.5% SDS). Lysates were  
826 incubated at 65°C for 30 minutes. Then 5 M KAc and 6 M LiCl were added at a ratio of 1:2.5  
827 and lysates were incubated on ice for 10 min. Lysates were centrifuged for 15 minutes at  
828 20,000xg, supernatant was isolated and mixed with Isopropanol. Lysates were centrifuged  
829 again for 15 minutes at 20,000xg, the supernatant was discarded and the DNA pellet was  
830 washed in 70% ethanol and subsequently dissolved in distilled water.

831

832

### 833 **FACS sorting of macrophages**

834 For embryo collections, adult flies of either  $w^+$ ; *srpHemo-3xmCherry* or  $w^+$ ;  
835 *CG9005<sup>BG02278</sup>*; *srpHemo-3xmCherry* genotypes were placed into plastic cages topped with  
836 apple juice plates with yeast for egg laying. Collections were performed at 29°C at 8h-20h  
837 light-dark cycle. Macrophages were collected from Stage 11-early Stage 12, when  
838 macrophages initiate invasive migration into the extended germband. Briefly, adult flies  
839 laid eggs for 1 hour, then the isolated plates with embryos were kept at 29°C for an  
840 additional 4 hours 45 minutes to reach the desired age. Embryos were collected for 2 days  
841 with about 6-7 collections per day and stored meanwhile at +4°C to slow down  
842 development. Collected embryos were dissociated and the macrophages were sorted

843 according to the procedure described in (Gyoergy et al., 2018). The cells were sorted using  
844 a FACS Aria III (BD) flow cytometer. Emission filters were 600LP, 610/20 and 502 LP,  
845 510/50. Data was analyzed with FloJo software (Tree Star). The cells from the negative  
846 control embryos were sorted to set a baseline plot. Approximately  $1-1.5 \times 10^5$   
847 macrophages were sorted within 30 minutes.

848

#### 849 **Sequencing of the macrophage transcriptome**

850 Total RNA was isolated from the FACS-sorted macrophages using the Qiagen RNeasy  
851 Mini kit (Cat No. 74104). The quality and concentration of RNA was determined using the  
852 Agilent 6000 Pico kit (Cat No. 5067-1513) on the Agilent 2100 Bioanalyzer: about 100 ng  
853 of total RNA was extracted from  $1.5 \times 10^5$  macrophages. RNA sequencing was performed  
854 by the CSF facility of the Vienna Biocenter according to their standard procedures  
855 (<https://www.vbcf.ac.at/facilities/next-generation-sequencing/>). Briefly, a cDNA library  
856 was synthesized using the QuantSeq 3' mRNA-seq Library Prep kit and 4 replicates of each  
857 of the genotypes ( $w^+$ ;  $+$ ; *srpHemo::3xmCherry* or  $w^+$ ; *CG9005<sup>BG02278</sup>*; *srpHemo-*  
858 *3xmCherry*) were sequenced on the Illumina HiSeq 2500 platform.

859 The reads were mapped to the *Drosophila melanogaster* Ensembl BDGP6 reference  
860 genome with STAR (version 2.5.1b). The read counts for each gene were detected using  
861 HTSeq (version 0.5.4p3). The Flybase annotation (r6.19) was used in both mapping and  
862 read counting. The counts were normalised using the TMM normalization from the edgeR  
863 package in R (Anders and Huber, 2015; Dobin et al., 2013). (Prior to statistical testing the  
864 data was transformed and then the differential expression between the sample groups was  
865 calculated with the limma package in R. The functional analyses were done using the  
866 topGO and gage packages in R.

867

#### 868 **Time-lapse imaging**

869 Embryos were dechorionated in 50% bleach for 4 min, washed with water, and mounted in  
870 halocarbon oil 27 (Sigma) between a coverslip and an oxygen permeable membrane (YSI).  
871 The anterior dorsolateral region of the embryo was imaged on an inverted multiphoton  
872 microscope (TrimScope, LaVision) equipped with a W Plan-Apochromat 40X/1.4 oil  
873 immersion objective (Olympus). mCherry was imaged at an 820 nm excitation wavelength,  
874 using an optical parametric oscillator technology (Coherent Chameleon Compact OPO).  
875 Excitation intensity profiles were adjusted to tissue penetration depth and Z-sectioning for  
876 imaging was set at  $1 \mu\text{m}$  for tracking. For long-term imaging, movies were acquired for  
877 180-200 minutes with a frame rate of 40 seconds. Embryos were imaged with a temperature  
878 control unit set to  $29^\circ\text{C}$ .

879

#### 880 **Image Analysis**

##### 881 **Macrophage cell counts**

882 Autofluorescence of the embryo was used to measure the position of the germband to  
883 determine the stages for analysis of fixed samples. Embryos with germband retraction of  
884 between 29-31% were assigned to Stage 11. Embryos with 35-40% retraction (Stage 12)  
885 were analysed for the number of macrophages that had entered the germband. Embryos with  
886 above 50-75% retraction were used for the number along the ventral nerve cord (vnc) and in



887 the whole embryo. Macrophages were visualized using confocal microscopy with a Z-  
888 resolution of 2  $\mu\text{m}$  and the number of macrophages within the germband or the segments of  
889 the vnc was calculated in individual slices (and then aggregated) using the Cell Counter  
890 plugin in FIJI. Total macrophage numbers were obtained using Imaris (Bitplane) by detecting  
891 all the macrophage nuclei as spots.

892

### 893 **Macrophage tracking, speed, directionality and time for macrophage entry analysis**

894 Embryos in which the macrophage nuclei were labeled with *srpHemo-H2A::3XmCherry*  
895 were imaged and 250X130X36  $\mu\text{m}^3$  3D-stacks were typically acquired with a constant  
896 0.5X0.5X1  $\mu\text{m}^3$  voxel size at every 40-41 seconds for approximately 3 hours. Images  
897 acquired from multiphoton microscopy were initially processed with InSpector software  
898 (LaVision Bio Tec) to compile channels from the imaging data (Table 3). Afterwards, the  
899 exported files were further processed using Imaris software (Bitplane) to visualize the  
900 recorded channels in 3D and the movie from each imaged embryo was rotated and aligned  
901 along the AP axis for further tracking analysis.

902 To analyze the movies by Imaris, the following analyses were applied:

903 **i.** To calculate the migration parameters while macrophages migrate from the head mesoderm  
904 to the yolk zone, movies were cropped in time to that period (typically 60 minutes from the  
905 original movie was used for analysis).

906 **ii.** To calculate the migration parameters of the macrophage moving on the yolk zone into the  
907 edge of germband, movies were acquired from the time point of the first macrophage  
908 appearing in the yolk zone and recorded until the onset of germband retraction.

909 **iii.** Macrophage nuclei were extracted using the spot detection function and tracks generated  
910 in 3D over time. We could not detect all macrophages in the head mesoderm as spots because  
911 of limitations in our imaging parameters. Tracks of macrophages which migrate towards the  
912 dorsal vessel, ventral nerve cord (vnc) and to the anterior of the head were omitted. The edge  
913 of the germband was detected using autofluorescence from the yolk and the mean position of  
914 the tracks in X- and Y-axis was used to restrict analysis to before macrophages reach the  
915 edge of the germband.

916 **iv.** Nuclei positions in XYZ-dimensions were determined for each time point and used for  
917 further quantitative analysis.

918 **v.** The time point when the first macrophage nucleus reached the germband was defined as  
919 T0 and the time point when the macrophage nucleus was within the germband and moved  
920 forward along the route between the ectoderm and mesoderm was taken as T1 and T1-T0 was  
921 defined as time for macrophage entry. T0 and T1 were determined by precisely examining  
922 macrophage position in xy and z dimensions (examination of individual 2 micron slices) over  
923 time.

924 **vi.** To measure the speed along the route between the germband edge and the yolk, tracks  
925 generated from macrophages from the time when the first macrophages started to move along  
926 the mentioned path until germband retraction onset were utilized.

927 **vii.** To calculate the speed of migration of the first or second macrophages in the germband  
928 the track generated for the first or second macrophages alone was used to obtain the nuclei  
929 position in XYZ-dimensions. Moreover, the average speed of the third through fifth  
930 macrophages moving along the same route was also measured. Speed was calculated within

931 the first 30-35  $\mu\text{m}$  of the path between the germband ectoderm and mesoderm. The mean  
932 position of the tracks in X- and Y-axis was used to restrict analysis to either of the migratory  
933 zones (head, yolk, germband entry, route along the germband ectoderm and mesoderm, route  
934 along the germband mesoderm and the yolk).

935 Macrophage migratory parameters, including cell speed and directionality  
936 (persistence), were calculated in Matlab (The MathWorks Inc.) from single cell positions in  
937 3D for each time frame measured in Imaris (Bitplane), as described elsewhere (Smutny et al.,  
938 2017). Briefly, instantaneous velocities from single cell trajectories were averaged to obtain a  
939 mean instantaneous velocity value over the course of the measurement. To calculate  
940 directionality values, single cell trajectories were split into segments of equal length ( $l$ ;  $l = 10$   
941 frames) and calculated via a sliding window as the ratio of the distance between the  
942 macrophage start-to-end distance ( $D$ ) over the entire summed distance covered by the  
943 macrophage between each successive frame ( $d_i$ ) in a segment. Calculated directionality  
944 values were averaged over all segments in a single trajectory and all trajectories were  
945 averaged to obtain a directionality index ( $I$ ) for the duration of measurement (with 0 being  
946 the lowest and 1 the maximum directionality) as follows:

$$I(l) = \sum_{k=1}^{n-l} \frac{\left( D_k / \sum_{i=k}^{k+l} d_i \right)}{n-l}$$

947 where  $n$  defines the total number of frames,  $i$  the sum of frame-to-frame distances over one  
948 segment and  $k$  the sum over all segments of a trajectory.

949 Embryos from the control ( $w^+$ ; +; *srpHemo::3xmCherry*) and the CG9005 mutant ( $w^+$ ;  
950 *CG9005<sup>BG02278</sup>*; *srpHemo::3xmCherry*) were used for calculating the time for macrophage  
951 entry. Briefly, 100X130X34 $\mu\text{m}^3$  3D-stacks were typically acquired with a constant  
952 0.28X0.28X2 $\mu\text{m}^3$  voxel size at every 40-41 seconds for approximately 3 hours.

953

#### 954 **Cloning of constructs**

955 Standard molecular biology methods were used and all constructs were sequenced by the  
956 Mycosynth company (Vienna, Austria) before injection into flies. The enzymes *NotI*, T4  
957 Polynucleotide Kinase (*PNK*) and *DpnI* were obtained from New England Biolabs, Ipswich,  
958 Massachusetts, USA (Frankfurt, Germany). PCR amplifications were performed with GoTaq  
959 G2 DNA polymerase (Promega, Madison, USA) using a peqSTAR 2X PCR machine from  
960 PEQLAB, (Erlangen, Germany). All Infusion cloning was conducted using an Infusion HD  
961 Cloning kit (Clontech's European distributor). The relevant oligo sequences were chosen  
962 using the Infusion primer Tool at the Clontech website  
963 (<http://bioinfo.clontech.com/infusion/convertPcrsInit.do>).

964

#### 965 **Construction of *srpHemo*-CG9005**

966 A 3894 bp fragment containing the CG9005 ORF was amplified from the *UAS*-  
967 *CG9005::FLAG::HA* construct (Table S3) (*Drosophila* Genomics Resource Centre, DGRC)  
968 using relevant primers (Table S4). The fragment was cloned into the *srpHemo* plasmid (a gift

969 from Katja Brückner (Brückner et al., 2004) after its linearization with *NotI*, using an  
970 Infusion HD cloning kit (Clontech's European distributor).

971

### 972 **Construction of *srpHemo-FAM214A* and *srpHemo-FAMB214B***

973 Fragments of 3225 bp and 1615 bp containing the FAM214A and FAMB214B ORFs,  
974 respectively, were amplified from cDNA prepared from dendritic cells (a gift from M. Sixt's  
975 lab) with FAM214A Fwd and Rev primers, and with FAM214B Fwd and FAM214B Rev  
976 primers (Table S4). The fragments were cloned into the *srpHemo* plasmid using an Infusion  
977 HD cloning kit after its linearization with *NotI* (NEB).

978

### 979 **Construction of mutant forms of *srpHemo-atossa***

980 Mutant forms of *atossa* (CG9005) were generated by removing the desired region from the  
981 CG9005 cDNA sequence by using inverse PCR followed by blunt end ligation and related  
982 primers (Table S4). Afterwards, *atossa* mutant constructs in the Bluescript vector were  
983 amplified and cloned into the *srpHemo* plasmid after its linearization with *NotI*, using an  
984 Infusion HD cloning kit.

985

### 986 **Transgenic fly line production**

987 The *srpHemo* and *UAS* constructs (Table S4) was injected into syncytial blastoderm stage  
988 embryos of M{3xP3-RFP.attP}ZH-86Fb (BL 24749) line (obtained from Peter Duchek of  
989 IMBA) to generate inserts on third chromosome by C31-mediated integration (Table S3)  
990 (Bischof et al., 2007; Gyoergy et al., 2018).

991

### 992 **CRISPR sgRNA production and cloning**

993 sgRNA target sequences for CRISPR-Cas9 based gene knock down for CG9253 (*porthos*)  
994 were designed as 20 nt sequences upstream of an NGG PAM motif in the *Drosophila* genome  
995 (<https://www.flyrnai.org/crispr/>) (Basset and Liu, 2014). The targeting oligonucleotides  
996 incorporated into *porthos* sgRNAs are given in (Table S4, The annealed oligo inserts were  
997 cloned into BspQ1-digested pAC-sgRNA-Cas9 vector (Addgene, plasmid # 49330) before  
998 transformation. Positive clones were confirmed by sequencing with pAC-sgRNA-Cas9-U6F  
999 primer (Table S4). All CRISPR-Cas9 constructs contain three distinct cassettes for  
1000 expression of Cas9, an sgRNA against *porthos*, and a puromycin resistance marker.

1001

### 1002 **Generation of *porthos* depleted S2R+ cells**

1003 To make the stable depleted cell lines, S2R+ Cells ( $2 \times 10^5$ ) were seeded in Schneider  
1004 medium plus 10% FCS (Gibco 21720024, Sigma F9665) in a 24-well plate. Plasmid sgRNA  
1005 CRISPR *porthos* was co-transfected (1  $\mu$ g of total DNA per well) with Effectene Transfection  
1006 Reagent (Qiagen, Hilden, Germany) following the manufacturer's protocol. 4 hours after  
1007 transfection the medium was changed and the cells were incubated for 72 hours at 25°C.  
1008 Cells were then transferred to a 6-well plate before addition of 5 $\mu$ g/ml Puromycin. Selection  
1009 with Puromycin took place for 7 days. Surviving cells were incubated without selection  
1010 medium for 24 hours, after that they were added to 96-well cell culture plates in conditioned  
1011 medium at a density of 1 cell/well. After 7 days we checked the wells for growing colonies to  
1012 rule out that more than 1 colony was present per well. When cells were dense enough we first

1013 transferred them to a 24-, then a 12- and finally a 6-well plate. Once the cells reached  
1014 confluency, we extracted the genomic DNA to perform a PCR-based prescreening of  
1015 *porthos*-depleted cells to detect effective CRISPR (Table S4).

1016

### 1017 **Quantitative Real Time-PCR (qRT-PCR) analysis**

1018 To verify the effective knockdown of genes, we first isolated RNA from S2R+ cells ( $1 \times 10^7$   
1019 for the control and KD cells) according to the manufacturer's protocol (Qiagen RNeasy Mini  
1020 Kit Cat No./ID: 74104). We used 500 ng of isolated RNA for cDNA synthesis, according to  
1021 the manufacturer's protocol (Qiagen Omniscript RT, Cat No./ID: 205111). Afterwards we  
1022 performed qPCR to assess the mRNA expression of *atossa* and *porthos*, using *RpS20* as an  
1023 internal control. Primer sequences for *Drosophila atossa* (CG9005) and *porthos* (CG9253)  
1024 transcripts were designed using NCBI's primer design tool  
1025 (<https://www.ncbi.nlm.nih.gov/tools/primer-blast/>) and primer sequences for *RpS20* gene, as an  
1026 internal control gene, were obtained from the FlyPrimerBank  
1027 (<http://www.flyrnai.org/FlyPrimerBank>) (Table S5). We amplified 4  $\mu$ L cDNA (50 ng) using  
1028 10  $\mu$ L of Takyon™ No Rox SYBR MasterMix Blue dTTP (Eurogentec, Liege, Belgium), 2  $\mu$ L  
1029 of each reverse and forward primers (10 mM). The thermal cycling conditions were as  
1030 follows: 40 cycles of amplification each consisting of 10 s at 95°C, 15 s at 60°C and 10 s at  
1031 72°C, and cooling at 4°C. The experiments were carried out in technical triplicates and three  
1032 biological replicates for each data point. The qPCR experiment was run on a LightCycler 480  
1033 (Roche, Basel, Switzerland) and data were analyzed in the LightCycler 480 Software and Prism  
1034 (GraphPad Software). To calculate the fold change in *atossa* and *porthos* mRNA levels  
1035 compared to the house-keeping gene mRNA levels, we averaged the Ct values of the technical  
1036 replicates of each trial. We measured  $\Delta$ ct by subtracting the housekeeping gene Ct average  
1037 from the Ct average of *atossa* or *porthos*. Afterwards, the  $2^{-\Delta$ ct was calculated for each trial.

1038

### 1039 **Polysome profiling in *porthos*-KD S2 cells**

#### 1040 **RNAi treatment of S2 cells**

1041 dsRNA for *porthos* (CG9253) was prepared as described by the SnapDragon manual  
1042 (<https://www.flyrnai.org/snapdragon>). Briefly, template was prepared from S2 cell cDNA  
1043 using the following primers designed using SnapDragon 5'-  
1044 TAATACGACTCACTATAGGATAAG GAAGGGGACAGCGAG-3' and the reverse  
1045 primer: 5'-TAATACGACTCACTATAGGTTTGAATGCCAGTTCCTC-3' both of  
1046 which contain a T7 polymerase promoter. As a negative control, we made non-targeting  
1047 dsRNA against GFP using the following primers: 5'-  
1048 TAATACGACTCACTATAGGGGAGCGCACCATCTTCTCAA-3' and 5'-  
1049 TAATACGACTCACTATAGGGCTGCTTGTCGGCCATGATATAG-3'. We performed *in*  
1050 *vitro* transcription overnight at 37°C using the T7 Megascript kit (AM1334) following  
1051 manufacturer's instructions (Table S4). The RNA was treated with DNase and purified using  
1052 acid-phenol chloroform extraction and ethanol precipitated. The resulting RNA was annealed  
1053 by heating at 65°C for 5 minutes and slow cooling to 37°C for an hour. Knocking down in S2  
1054 cells was performed using 1  $\mu$ g of dsRNA as previously described  
1055 (<https://www.ncbi.nlm.nih.gov/pmc/articles/PMC4465107/>).  $0.5-1.0 \times 10^6$  cells were seeded  
1056 30 minutes prior to transfection to adhere. Prior to transfection, the media was changed for

1057 500 µl of fresh media. The seeded cells were treated with 500 µl of transfection complexes  
1058 per well of a 6-well plate. 48 hours post transfection, cells were passaged to 10 cm dishes.  
1059 After 3 more days cells were harvested for further analysis.

1060

#### 1061 **Polysome profiling and polysome sequencing**

1062 Polysome sequencing was performed as described by (Flora et al., 2018) with minor  
1063 modifications. Cells were incubated with fresh medium 2-4 hours before harvesting.  
1064 Cycloheximide (100 µg/ml) was first added to the medium for 3 min at RT, and the cells  
1065 were subsequently centrifuged at 800 xg for 3 min. The cell pellet was afterwards washed  
1066 two times with ice-cold phosphate-buffered saline (1X PBS, pH 7.4). The supernatant was  
1067 discarded and the pellet was gently resuspended in 300 µl of lysis buffer A (300 mM NaCl,  
1068 15 mM Tris-HCl, pH 7.5, 15 mM EDTA, 1 mg/ml heparin, 1% Triton-X100, and 100 µg/ml  
1069 cycloheximide) and lysed for 15 min on ice. The lysate was clarified by centrifugation at  
1070 8500 xg for 5 min at 4°C. 20% of the lysate was kept aside as an input. The clarified lysate  
1071 was loaded onto a 10%-50% sucrose gradient in Buffer B (300 mM NaCl, 15 mM Tris-HCl,  
1072 pH 7.5, 15 mM MgCl<sub>2</sub>, supplemented with 100 µg/ml cycloheximide) and centrifuged for 3  
1073 hours at 35,000 rpm in an SW41 rotor in a Beckman L7 ultracentrifuge (Beckman Coulter,  
1074 Krefeld, Germany). The gradients were simultaneously fractionated on a Density Gradient  
1075 Fractionation System (#621140007) at 0.75 ml/min. We added 20 µl of 20% SDS, 8 µl of 0.5  
1076 M pH 8 EDTA, and 16 µl of proteinase K (#P8107S) to each polysome fraction and  
1077 incubated them for 30 min at 37°C. The RNA from each fraction was extracted by standard  
1078 acid phenol: chloroform purification followed by 80% ethanol precipitation. The polysome  
1079 fractions were then measured for RNA content and RNAseq libraries were prepared.

1080

#### 1081 **Polysome-seq library preparation and mRNA sequencing**

1082 The RNA was first treated with Turbo DNase (TURBO DNA-free Kit, Life Technologies,  
1083 AM1907) and then purified using DNase Inactivation buffer. The RNA was then centrifuged  
1084 for 1.5 min at 1000 xg and the supernatant was collected and centrifuged once more at the  
1085 same condition. The RNA quantity was determined by measuring the absorbance at 260 nm  
1086 (NanoDrop 2000 spectrophotometer; Peqlab).

1087 Poly-A selection was performed according to manufacturer's instructions (Bioo Scientific  
1088 Corp., 710 NOVA-512991). Following Poly-A selection mRNA libraries were prepared  
1089 according to manufacturer's instructions (Bioo Scientific Corp., NOVA-5138-08), except that  
1090 the RNA was incubated at 95°C for 13 min to generate optimal fragment sizes. The  
1091 sequencing library quantity was determined using Qubit (Thermo Fisher Scientific). The  
1092 library integrity was assessed with a Bioanalyzer 2100 system (RNA 6000 Pico kit, Agilent  
1093 Technologies). The libraries on biological duplicates from each genotype were subjected to  
1094 75 base-pair single-end sequencing on Illumina NextSeq500 at the Center for Functional  
1095 Genomics (CFG).

1096

#### 1097 **Data analysis of S2 cell polysome sequencing**

1098 First the reads were assessed for their quality using FastQC. Mapping of the reads was  
1099 performed against *Drosophila* Genome (dm6.01, [www.fruitfly.org](http://www.fruitfly.org)) using Hisat version 2.1.0.  
1100 Mapped reads were then assigned to feature using featureCount version v1.6.4. To calculate



1101 Translation efficiency (TE), TPMs (transcripts per million) values for polysome-libraries  
1102 were calculated (Flora et al., 2018). All transcripts with zero reads were discarded from  
1103 libraries for further analysis. The log<sub>2</sub> ratio of TPMs between the polysome fraction and total  
1104 mRNA was measured. This ratio represents TE. The TE value of each replicate was averaged  
1105 and delta TE ( $\Delta$ TE) was calculated as (*porthos* dsRNA TE)/(GFP dsRNA TE). Targets were  
1106 defined as transcripts falling greater or less than two standard deviations (SD) from the  
1107 median of  $\Delta$ TE (Table S5).

1108

### 1109 **Extracellular flux measurements for bioenergetic profiling**

1110 Cellular respiration was assessed using a Seahorse XF96 extracellular flux analyzer (Agilent  
1111 Technologies, Santa Clara, CA USA). The oxygen consumption rate (OCR) as a measure of  
1112 oxygen utilization of cells is an important indicator of mitochondrial function. The  
1113 extracellular acidification rate (ECAR) is a measure of glycolytic activity measured via  
1114 extracellular acidification due to lactate release, formed during the conversion of glucose to  
1115 lactate during anaerobic glycolysis. Prior to measurement, wild-type and *porthos* KD cells  
1116 were seeded at  $10 \times 10^5$  cells per well in Seahorse XF96 polystyrene tissue culture plates  
1117 (Agilent) and incubated in unbuffered Seahorse RPMI assay medium (Agilent) supplemented  
1118 with glucose (25 mM; Sigma-Aldrich), sodium pyruvate (1 mM; Gibco), and glutamine (2  
1119 mM; Gibco) in a non-CO<sub>2</sub> incubator at 25°C and pH 7.4 for 1 h before the experiment.  
1120 Cellular oxygen consumption was assessed in basal condition (prior to any addition) and after  
1121 addition of oligomycin (2  $\mu$ M; Agilent) Carbonyl cyanide-4 (trifluoromethoxy)  
1122 phenylhydrazone (FCCP, 2  $\mu$ M; Sigma-Aldrich), antimycin A and rotenone (both at 1  $\mu$ M;  
1123 Agilent). The three drugs were injected into the XF96 plate sequentially. This allowed for  
1124 calculation of OCR linked to ATP production, maximal respiration capacity and spare  
1125 respiratory capacity. Basal respiration was measured prior to injection of oligomycin A. Both  
1126 OCR and ECAR were measured every 4 min with a mixing of 2 min in each cycle, with 4  
1127 cycles in total for the first step and 3 cycles thereafter.

1128 Different parameters from the OCR graph were measured as follows. ATP turnover  
1129 was calculated by subtracting the “last rate measurement before oligomycin” from the  
1130 “minimum rate measurement after oligomycin injection”. Maximal respiration was defined as  
1131 (maximum rate measurement after FCCP) - (non-mitochondrial respiration). Spare  
1132 respiratory capacity (SRC) was measured by subtracting basal respiration from maximal  
1133 respiration (Mookerjee et al., 2017).

1134

### 1135 **Metabolomics profiling analysis**

1136 Samples for metabolomics were assessed by the VBCF metabolomics facility according to  
1137 Rao et al. with slight modifications  
1138 (<https://www.viennabiocenter.org/facilities/metabolomics/>) (Rao et al., 2019). 1 gr of wild-  
1139 type or *atos* embryos were extracted using an ice-cold MeOH:ACN:H<sub>2</sub>O (2:2:1, v/v) solvent  
1140 mixture. A volume of 1mL of cold solvent was added to each pellet, vortexed for 30 s, and  
1141 incubated in liquid nitrogen for 1 min. The samples were thawed at room temperature and  
1142 sonicated for 10 min. This cycle of cell lysis in liquid nitrogen combined with sonication was  
1143 repeated three times. To precipitate proteins, the samples were incubated for 1 h at -20°C,  
1144 followed by centrifugation at 13,000 rpm for 15 min at 4°C. The supernatant was removed

1145 and evaporated. The dry extracts were reconstituted in 100  $\mu$ L of ACN:H<sub>2</sub>O (1:1, v/v),  
1146 sonicated for 10 min, and centrifuged at 13,000 rpm for 15 min at 4°C to remove insoluble  
1147 debris. The supernatants were transferred to Eppendorf tubes, shock frozen and stored at  
1148 -80°C prior to LC/MS analysis. A volume of 1  $\mu$ L of the metabolite extract was injected on a  
1149 ZIC-pHILIC HPLC column operated at a flow rate of 100  $\mu$ L/min, directly coupled to a TSQ  
1150 Quantiva mass spectrometer (Thermo Fisher Scientific).

1151 We used the following transitions for quantitation in the negative ion mode: AMP 346  
1152 m/z to 79 m/z, ADP 426 m/z to 134 m/z, ATP 506 m/z to 159 m/z, IMP 347 m/z to 79 m/z,  
1153 GMP 362 m/z to 211 m/z, GDP 442 m/z to 344 m/z, GTP 522 m/z to 424 m/z, taurine 124  
1154 m/z to 80 m/z, malate 133 m/z to 115 m/z, citrate 191 m/z to 111 m/z, pyruvate 87 m/z to 43  
1155 m/z, lactate 89 m/z to 43 m/z, NADH 664 m/z to 408 m/z, NAD 662 m/z to 540 m/z, hexose  
1156 phosphates 259 m/z to 97 m/z, Acetyl CoA 808 m/z to 408 m/z, CoA 766 m/z to 408 m/z,  
1157 succinate 117 m/z to 73 m/z. Glutamine 147 m/z to 130 m/z, glutamate 148 m/z to 84 m/z,  
1158 serine 106 m/z to 60 m/z were calculated in the positive ion mode. For all transitions, the  
1159 optimal collision energy was defined by analyzing pure metabolite standards.  
1160 Chromatograms were manually interpreted using trace finder (Thermo Fisher Scientific),  
1161 validating experimental retention times with the respective quality controls. All  
1162 measurements were within the linear range of detection.

1163 For the metabolomics analysis, the metabolite concentration was normalized using a  
1164 Z-score normalization method with the formula of  $y = (x-\alpha)/\lambda$ , in which x refers to the real  
1165 concentration,  $\alpha$  indicates the mean value of all samples, and  $\lambda$  is the variance of all samples.  
1166 The normalized concentrations of metabolites were applied to generate a heatmap, which  
1167 showed the concentration difference of all metabolites. For KEGG (<http://www.kegg.jp>,  
1168 Tokyo, Japan) pathway analysis, the clusterProfiler R package was employed.  
1169

## 1170 **Statistics and repeatability**

1171 Statistical tests as well as the number of embryos/ cells assessed are listed in the figure  
1172 legends. All statistical analyses were performed using GraphPad Prism and significance was  
1173 determined using a 95% confidence interval. Data points from individual experiments/  
1174 embryos were pooled to estimate mean and SEM. No statistical method was used to  
1175 predetermine sample size and the experiments were not randomized. Unpaired t-test or  
1176 Mann-Whitney was used to calculate the significance in differences between two groups and  
1177 One-way Anova followed by Tukey post-test followed by Conover or Dunn's post-test for  
1178 multiple comparisons. All measurements were performed in 3-50 embryos. Representative  
1179 images illustrated in Figures 1A-C, Figures 2B-C,E, Figures S2A-B, Figures 3B-D, Figure  
1180 4A,I, Figure S4B, and Figure 6D,G,I were from separate experiments that were repeated at  
1181 least 3 and up to 7 times. Stills shown in Figure 1F, Figure S1I, Figure 4B, and Figure S4E  
1182 are representative images from two-photon movies, which were repeated at least 3 times.  
1183 Raw data from embryo scoring and analyzed tracking output from each movie is in Data S4.

1184

## 1185 **Exact genotype of *Drosophila* lines used in Figures:** 1186 **Figure 1 and Figure S1**

1187 **Figs. 1A-C:** Control: *w*<sup>-</sup>; +; *srpHemo-H2A::3xmCherry*, CG9005 mutant: *w*<sup>-</sup>;  
1188 *P{EP}CG9005<sup>BG02278</sup>*; *srpHemo-H2A::3xmCherry*, CG9005 rescue: *w*<sup>-</sup>;  
1189 *P{EP}CG9005<sup>BG02278</sup>*; *srpHemo-CG9005*, *srpHemo-H2A::3xmCherry*. **Fig. 1D:** Control: *w*<sup>-</sup>;  
1190 +; *srpHemo-H2A::3xmCherry*, CG9005 mutant: *w*<sup>-</sup>; *P{EP}CG9005<sup>BG02278</sup>*; *srpHemo-*  
1191 *H2A::3xmCherry*, Df1: *w*<sup>-</sup>; *P{EP}CG9005<sup>BG02278</sup>*/Df(2R)ED2222; *srpHemo-*  
1192 *H2A::3xmCherry*, Df2: *w*<sup>-</sup>; *P{EP}CG9005<sup>BG02278</sup>*/Df(2R)BSC259; *srpHemo-*  
1193 *H2A::3xmCherry*, CG9005 rescue: *w*<sup>-</sup>; *P{EP}CG9005<sup>BG02278</sup>*; *srpHemo-CG9005*, *srpHemo-*  
1194 *H2A::3xmCherry*. **Fig. 1E:** Control 1: *w*<sup>-</sup> *P(w+)UAS-dicer/w*<sup>-</sup>; *P{attP,y[+],w[3`]/+}*;  
1195 *srpHemo-Gal4 UAS-GFP*, CG9005 RNAi 1: *UAS-Dicer2/w*<sup>-</sup>; CG9005 RNAi (v106589)/+;  
1196 *srpHemo-Gal4 UAS-GFP*, *UAS-H2A::RFP/+*, Control 2: *w*<sup>-</sup> *P(w+)UAS-dicer/w*<sup>-</sup>; +;  
1197 *srpHemo-Gal4 UAS-GFP*, CG9005 RNAi 2: *UAS-Dicer2/w*<sup>-</sup>; CG9005 RNAi (v36080)/+;  
1198 *srpHemo-Gal4 UAS-GFP*, *UAS-H2A::RFP/+*, Control 3: *w*<sup>-</sup> *P(w+)UAS-dicer/w*<sup>-</sup>;  
1199 *P{attP,y[+],w[3`]/+}*; *srpHemo-Gal4 UAS-GFP*, CG9005 RNAi 3: *UAS-Dicer2/w*<sup>-</sup>; CG9005  
1200 RNAi (v33362)/+; *srpHemo-Gal4 UAS-GFP*, *UAS-H2A::RFP/+*. **Figs. 1F-L:** Control: *w*<sup>-</sup>; +;  
1201 *srpHemo-H2A::3xmCherry*, CG9005 mutant: *w*<sup>-</sup>; *P{EP}CG9005<sup>BG02278</sup>*; *srpHemo-*  
1202 *H2A::3xmCherry*.  
1203 **Fig. S1A:** Control: *w*<sup>-</sup>; +; *srpHemo-H2A::3xmCherry*, mutant: *w*<sup>-</sup>; *P{EP}CG9005<sup>BG02278</sup>*;  
1204 *srpHemo-H2A::3xmCherry*, Df1 cross: *w*<sup>-</sup>; *P{EP}CG9005<sup>BG02278</sup>*/Df(2R)ED2222; *srpHemo-*  
1205 *H2A::3xmCherry*, Df2 cross: *w*<sup>-</sup>; *P{EP}CG9005<sup>BG02278</sup>*/Df(2R)BSC259; *srpHemo-*  
1206 *H2A::3xmCherry*, CG9005 rescue: *w*<sup>-</sup>; *P{EP}CG9005<sup>BG02278</sup>*; *srpHemo-CG9005*, *srpHemo-*  
1207 *H2A::3xmCherry*. **Figs. S1B,H:** Control 1: *w*<sup>-</sup> *P(w+)UAS-dicer/w*<sup>-</sup>; *P{attP,y[+],w[3`]/+}*;  
1208 *srpHemo-Gal4 UAS-GFP*, CG9005 RNAi 1: *UAS-Dicer2/w*<sup>-</sup>; CG9005 RNAi (v106589)/+;  
1209 *srpHemo-Gal4 UAS-GFP*, *UAS-H2A::RFP/+*. Control 2: *w*<sup>-</sup> *P(w+)UAS-dicer/w*<sup>-</sup>; +;  
1210 *srpHemo-Gal4 UAS-GFP*, CG9005 RNAi 2: *UAS-Dicer2/w*<sup>-</sup>; CG9005 RNAi (v36080)/+;  
1211 *srpHemo-Gal4 UAS-GFP*, *UAS-H2A::RFP/+*. Control 3: *w*<sup>-</sup> *P(w+)UAS-dicer/w*<sup>-</sup>;  
1212 *P{attP,y[+],w[3`]/+}*; *srpHemo-Gal4 UAS-GFP*, CG9005 RNAi 3: *UAS-Dicer2/w*<sup>-</sup>; CG9005  
1213 RNAi (v33362)/+; *srpHemo-Gal4 UAS-GFP*, *UAS-H2A::RFP/+*. **Figs. S1C,G:** Control: *w*<sup>-</sup>;  
1214 +; *srpHemo-H2A::3xmCherry*, mutant: *w*<sup>-</sup>; *P{EP}CG9005<sup>BG02278</sup>*; *srpHemo-*  
1215 *H2A::3xmCherry*. **Fig. S1D:** Control 1: *w*<sup>-</sup> *P(w+)UAS-dicer/w*<sup>-</sup>; *P{attP,y[+],w[3`]/+}*;  
1216 *srpHemo-Gal4 UAS-GFP*, CG9005 RNAi 1: *UAS-Dicer2/w*<sup>-</sup>; CG9005 RNAi (v106589)/+;  
1217 *srpHemo-Gal4 UAS-GFP*, *UAS-H2A::RFP/+*. **Fig. S1E:** Control 2: *w*<sup>-</sup> *P(w+)UAS-dicer/w*<sup>-</sup>;  
1218 +; *srpHemo-Gal4 UAS-GFP*, CG9005 RNAi 2: *UAS-Dicer2/w*<sup>-</sup>; CG9005 RNAi (v36080)/+;  
1219 *srpHemo-Gal4 UAS-GFP*, *UAS-H2A::RFP/+*. **Fig. S1F:** Control 3: *w*<sup>-</sup> *P(w+)UAS-dicer/w*<sup>-</sup>;  
1220 *P{attP,y[+],w[3`]/+}*; *srpHemo-Gal4 UAS-GFP*, CG9005 RNAi 3: *UAS-Dicer2/w*<sup>-</sup>; CG9005  
1221 RNAi (v33362)/+; *srpHemo-Gal4 UAS-GFP*, *UAS-H2A::RFP/+*. **Figs. S1I-L:** Control: *w*<sup>-</sup>;  
1222 +; *srpHemo-H2A::3xmCherry*, CG9005 mutant: *w*<sup>-</sup>; *P{EP}CG9005<sup>BG02278</sup>*; *srpHemo-*  
1223 *H2A::3xmCherry*.

1224

## 1225 **Figure 2 and Figure S2**

1226 **Fig. 2B:** *w*<sup>-</sup>;+; *UAS-atossa::FLAG::HA*, *srpHemo-Gal4*, *srpHemo-H2A::3xmCherry*. **Figs.**  
1227 **2C,D:** Control: *w*<sup>-</sup>; +; *srpHemo-H2A::3xmCherry*, *atos* mutant: *w*<sup>-</sup>; *atossa<sup>BG02278</sup>*;  
1228 *srpHemo-H2A::3xmCherry*, *Atossa* rescue: *w*<sup>-</sup>; *atossa<sup>BG02278</sup>*; *srpHemo-atossa*, *srpHemo-*  
1229 *H2A::3xmCherry*, rescue: *w*<sup>-</sup>; *atossa<sup>BG02278</sup>*; *srpHemo-atossa<sup>DUF4210</sup>*, *srpHemo-*  
1230 *H2A::3xmCherry*, rescue: *w*<sup>-</sup>; *atossa<sup>BG02278</sup>*; *srpHemo-atossa<sup>CherSeg</sup>*, *srpHemo-*

1231 *H2A::3xmCherry*, rescue: *w-*; *atossa*<sup>BG02278</sup>; *srpHemo-atossa*<sup>DU4210-/CherSeg-</sup>, *srpHemo-*  
1232 *H2A::3xmCherry*, rescue: *w-*; *atossa*<sup>BG02278</sup>; *srpHemo-atossa*<sup>TAD1-/TAD2-</sup>, *srpHemo-*  
1233 *H2A::3xmCherry*. **Figs. 2E,F:** Control: *w-*; +; *srpHemo-H2A::3xmCherry*, mutant: *w-*;  
1234 *atossa*<sup>BG02278</sup>; *srpHemo-H2A::3xmCherry*, rescue: *w-*; *atossa*<sup>BG02278</sup>; *srpHemo-FAM214A*,  
1235 *srpHemo-H2A::3xmCherry*, rescue: *w-*; *atossa*<sup>BG02278</sup>; *srpHemo-FAM214B*, *srpHemo-*  
1236 *H2A::3xmCherry*.  
1237 **Figs. S2B:** Rescue: *w-*; *atossa*<sup>BG02278</sup>; *srpHemo-atossa*<sup>TAD1-</sup>, *srpHemo-H2A::3xmCherry*,  
1238 rescue: *w-*; *atossa*<sup>BG02278</sup>; *srpHemo-atossa*<sup>TAD2-</sup>, *srpHemo-H2A::3xmCherry*. **Fig. S2C:**  
1239 Control: *w-*; +; *srpHemo-H2A::3xmCherry*, *atos* mutant: *w-*; *atossa*<sup>BG02278</sup>; *srpHemo-*  
1240 *H2A::3xmCherry*, *Atossa* rescue: *w-*; *atossa*<sup>BG02278</sup>; *srpHemo-atossa*, *srpHemo-*  
1241 *H2A::3xmCherry*, rescue: *w-*; *atossa*<sup>BG02278</sup>; *srpHemo-atossa*<sup>TAD1-</sup>, *srpHemo-*  
1242 *H2A::3xmCherry*, rescue: *w-*; *atossa*<sup>BG02278</sup>; *srpHemo-atossa*<sup>TAD2-</sup>, *srpHemo-*  
1243 *H2A::3xmCherry*. **Fig. S2D:** Control: *w-*; +; *srpHemo-H2A::3xmCherry*, mutant: *w-*;  
1244 *atossa*<sup>BG02278</sup>; *srpHemo-H2A::3xmCherry*, rescue: *w-*; *atossa*<sup>BG02278</sup>; *srpHemo-atossa*,  
1245 *srpHemo-H2A::3xmCherry*, rescue: *w-*; *atossa*<sup>BG02278</sup>; *srpHemo-atossa*<sup>DUF4210-</sup>, *srpHemo-*  
1246 *H2A::3xmCherry*, rescue: *w-*; *atoss*<sup>BG02278</sup>; *srpHemo-atossa*<sup>CherSeg-</sup>, *srpHemo-*  
1247 *H2A::3xmCherry*, rescue: *w-*; *atossa*<sup>BG02278</sup>; *srpHemo-atossa*<sup>DUF4210-/CherSeg-</sup>, *2srpHemo-*  
1248 *H2A::3xmCherry*, rescue: *w-*; *atossa*<sup>BG02278</sup>; *srpHemo-atossa*<sup>TAD1-</sup>, *srpHemo-*  
1249 *H2A::3xmCherry*, rescue: *w-*; *atossa*<sup>BG02278</sup>; *srpHemo-atossa*<sup>TAD2-</sup>, *srpHemo-*  
1250 *H2A::3xmCherry*, rescue: *w-*; *atossa*<sup>BG02278</sup>; *srpHemo-atossa*<sup>TAD1-/2-</sup>, *srpHemo-*  
1251 *H2A::3xmCherry*. **Fig. S2E:** Control: *w-*; +; *srpHemo-H2A::3xmCherry*, *atos* mutant: *w-*;  
1252 *atossa*<sup>BG02278</sup>; *srpHemo-H2A::3xmCherry*, *Atossa* rescue: *w-*; *atossa*<sup>BG02278</sup>; *srpHemo-atossa*,  
1253 *srpHemo-H2A::3xmCherry*, rescue: *w-*; *atossa*<sup>BG02278</sup>; *srpHemo-FAM214A*, *srpHemo-*  
1254 *H2A::3xmCherry*, rescue: *w-*; *atossa*<sup>BG02278</sup>; *srpHemo-FAM214B*, *srpHemo-*  
1255 *H2A::3xmCherry*.

1256

### 1257 **Figure 3 and Figure 3S**

1258 **Figs. 3B,F:** Control (for *porthos* or *CG9253*): *w/y,w[1118]*; *P{attP,y[+],w[3']}*; *srpHemo-*  
1259 *Gal4*, *srpHemo-H2A::3xmCherry/+*, *CG9253 RNAi* (*porthos*): *w-*; *porthos RNAi*  
1260 (*v36589*)/+; *srpHemo-Gal4*, *srpHemo-H2A::3xmCherry/+*. **Fig. 3C:** Control 1 (for *CG9331*  
1261 or *GR/HPR*): *w/y,w[1118]*; *P{attP,y[+],w[3']}*; *srpHemo-Gal4*, *srpHemo-*  
1262 *H2A::3xmCherry/+*, *CG9331 RNAi* 1 (*GR/HPR*): *UAS-Dicer2/ w-*; *GR/HPR RNAi*  
1263 (*v44653*)/+; *srpHemo-Gal4*, *srpHemo-H2A::3xmCherry/+*. **Fig. 3D:** Control 1 (for *CG7144*  
1264 or *LKR/SDH*): *w/y,w[1118]*; *P{attP,y[+],w[3']}*; *srpHemo-Gal4*, *srpHemo-*  
1265 *H2A::3xmCherry/+*, *CG7144 RNAi* 1 (*LKR/SDH*): *UAS-Dicer2/ w-*; *LKR/SDH RNAi*  
1266 (*v51346*)/+; *srpHemo-Gal4*, *srpHemo-H2A::3xmCherry/+*. **Fig. 3F:** Control 1: *w/y,w[1118]*;  
1267 *P{attP,y[+],w[3']}*; *srpHemo-Gal4*, *srpHemo-H2A::3xmCherry/+*, *CG9331 RNAi* 1  
1268 (*GR/HPR*): *UAS-Dicer2/ w-*; *GR/HPR RNAi* (*v44653*)/+; *srpHemo-Gal4*, *srpHemo-*  
1269 *H2A::3xmCherry/+*, Control 2: *w/y,w[1118]*; *P{attP,y[+],w[3']}*; *srpHemo-Gal4*, *srpHemo-*  
1270 *H2A::3xmCherry/+*, *CG9331 RNAi* 2 (*GR/HPR*): *UAS-Dicer2/ w-*; *GR/HPR RNAi*  
1271 (*v10780*)/+; *srpHemo-Gal4*, *srpHemo-H2A::3xmCherry/+*, Control 3: *w/y,w[1118]*;  
1272 *P{attP,y[+],w[3']}*; *srpHemo-Gal4*, *srpHemo-H2A::3xmCherry/+*, *CG9331 RNAi* 3  
1273 (*GR/HPR*): *UAS-Dicer2/ w-*; *GR/HPR RNAi* (*64652*)/+; *srpHemo-Gal4*, *srpHemo-*



1274 *H2A::3xmCherry/+*. **Fig. 3G:** Control 1: *w/y,w[1118]; P{attP,y[+],w[3']}*; *srpHemo-Gal4*,  
1275 *srpHemo-H2A::3xmCherry/+*, CG7144 RNAi 1 (*LKR/SDH*): *UAS-Dicer2/w-*; *LKR/SDH*  
1276 *RNAi (v51346)/+*; *srpHemo-Gal4*, *srpHemo-H2A::3xmCherry/+*, Control 2: *w/y,w[1118];*  
1277 *P{attP,y[+],w[3']}*; *srpHemo-Gal4*, *srpHemo-H2A::3xmCherry/+*, CG7144 RNAi 2  
1278 (*LKR/SDH*): *UAS-Dicer2/w-*; *LKR/SDH RNAi (v109650)/+*; *srpHemo-Gal4*, *srpHemo-*  
1279 *H2A::3xmCherry/+*.  
1280 **Figs. S3A-B:** Control: *w-*; *+*; *srpHemo-H2A::3xmCherry*, mutant: *w-*; *P{EP}CG9005<sup>BG02278</sup>*;  
1281 *srpHemo-H2A::3xmCherry*. **Fig. S3D:** Control 1: *w/y,w[1118]; P{attP,y[+],w[3']}*;  
1282 *srpHemo-Gal4*, *srpHemo-H2A::3xmCherry/+*, CG2137 RNAi 1 (*Gpo2*): *w-/y,w[1118];*  
1283 *Gpo2 RNAi (v41234)/+*; *srpHemo-Gal4*, *srpHemo-H2A::3xmCherry/+*, Control 2:  
1284 *w/y,w[1118]; P{attP,y[+],w[3']}*; *srpHemo-Gal4*, *srpHemo-H2A::3xmCherry/+*, CG2137  
1285 RNAi 2 (*Gpo2*): *w-/y,w[1118]; Gpo2 RNAi (68145)/+*; *srpHemo-Gal4*, *srpHemo-*  
1286 *H2A::3xmCherry/+*. **Fig. S3E:** Control 1: *w/y,w[1118]; P{attP,y[+],w[3']}*; *srpHemo-Gal4*,  
1287 *srpHemo-H2A::3xmCherry/+*, CG11061 RNAi 1 (*GM130*): *w-/y,w[1118]; GM130 RNAi*  
1288 (*v330284)/+*; *srpHemo-Gal4 UAS-GFP*, *UAS-H2A::RFP/+*, Control 2: *w/y,w[1118];*  
1289 *P{attP,y[+],w[3']}*; *srpHemo-Gal4*, *srpHemo-H2A::3xmCherry/+*, CG11061 RNAi 2  
1290 (*GM130*): *w-/y,w[1118]; GM130 RNAi (64920)/+*; *srpHemo-Gal4*, *srpHemo-*  
1291 *H2A::3xmCherry/+*. **Fig. S3F:** Control (for CG9253 or *porthos*): *w/y,w[1118];*  
1292 *P{attP,y[+],w[3']}*; *srpHemo-Gal4*, *srpHemo-H2A::3xmCherry/+*, CG9253 RNAi (*porthos*):  
1293 *w-*; *porthos RNAi (v36589)/+*; *srpHemo-Gal4*, *srpHemo-H2A::3xmCherry/+*. **Fig. S3G:**  
1294 Control 1: *w/y,w[1118]; P{attP,y[+],w[3']}*; *srpHemo-Gal4*, *srpHemo-H2A::3xmCherry/+*,  
1295 CG9331 RNAi 1 (*GR/HPR*): *UAS-Dicer2/w-*; *GR/HPR RNAi (v44653)/+*; *srpHemo-Gal4*,  
1296 *srpHemo-H2A::3xmCherry/+*, Control 2: *w/y,w[1118]; P{attP,y[+],w[3']}*; *srpHemo-Gal4*,  
1297 *srpHemo-H2A::3xmCherry/+*, CG9331 RNAi 2 (*GR/HPR*): *UAS-Dicer2/w-*; *GR/HPR RNAi*  
1298 (*v10780)/+*; *srpHemo-Gal4*, *srpHemo-H2A::3xmCherry/+*, Control 3: *w/y,w[1118];*  
1299 *P{attP,y[+],w[3']}*; *srpHemo-Gal4*, *srpHemo-H2A::3xmCherry/+*, CG9331 RNAi 3  
1300 (*GR/HPR*): *UAS-Dicer2/w-*; *GR/HPR RNAi (64652)/+*; *srpHemo-Gal4*, *srpHemo-*  
1301 *H2A::3xmCherry/+*. **Fig. S3H:** Control 1: *w/y,w[1118]; P{attP,y[+],w[3']}*; *srpHemo-Gal4*,  
1302 *srpHemo-H2A::3xmCherry/+*, CG7144 RNAi 1 (*LKR/SDH*): *UAS-Dicer2/w-*; *LKR/SDH*  
1303 *RNAi (v51346)/+*; *srpHemo-Gal4*, *srpHemo-H2A::3xmCherry/+*, Control 2: *w/y,w[1118];*  
1304 *P{attP,y[+],w[3']}*; *srpHemo-Gal4*, *srpHemo-H2A::3xmCherry/+*, CG7144 RNAi 2  
1305 (*LKR/SDH*): *UAS-Dicer2/w-*; *LKR/SDH RNAi (v109650)/+*; *srpHemo-Gal4*, *srpHemo-*  
1306 *H2A::3xmCherry/+*.

1307

#### 1308 **Figure 4 and Figure 4S**

1309 **Fig. 4A:** *w-*; *+*; *UAS-porthos::FLAG::HA*, *srpHemo-Gal4*, *srpHemo::3xmCherry*. **Figs. 4B-**  
1310 **H:** Control: *w/y,w[1118]; P{attP,y[+],w[3']}*; *srpHemo-Gal4*, *srpHemo-*  
1311 *H2A::3xmCherry/+*, CG9253 RNAi (*porthos*): *w-*; *porthos RNAi (v36589)/+*; *srpHemo-*  
1312 *Gal4*, *srpHemo-H2A::3xmCherry/+*. **Figs. 4I-J:** Control: *w-*; *+*; *srpHemo-H2A::3xmCherry*,  
1313 *atos* mutant: *w-*; *atossa<sup>BG02278</sup>*; *srpHemo-H2A::3xmCherry*, *Atos* rescue: *w-*; *atossa<sup>BG02278</sup>*;  
1314 *UAS-atossa::FLAG::HA*, *srpHemo-Gal4*, *srpHemo-H2A::3xmCherry*, rescue: *w-*;  
1315 *atossa<sup>BG02278</sup>*; *UAS-porthos::FLAG::HA*, *srpHemo-Gal4*, *srpHemo-H2A::3xmCherry*.



1316 **Figs. 4SC-H:** Control: *w/y,w[1118]; P{attP,y[+],w[3' ]/+; srpHemo-Gal4, srpHemo-*  
1317 *H2A::3xmCherry/+*, CG9253 RNAi (*porthos*): *w-; porthos RNAi (v36589)/+; srpHemo-*  
1318 *Gal4, srpHemo-H2A::3xmCherry/+*.

1319

### 1320 **Figure 6 and Figure 6S**

1321 **Fig. 6D-F:** Control: *w-; +; srpHemo-Gal4, srpHemo-H2A::3xmCherry*, dominant negative  
1322 inhibitor of Complex V (CV-DN): *w-;UAS-CVDN; srpHemo-Gal4, srpHemo-*  
1323 *H2A::3xmCherry*. **Figs. 6G-H:** Control: *w-; P{attP,y[+],w[3' ]/+; srpHemo-Gal4,*  
1324 *srpHemo-H2A::3xmCherry*, Complex III (Cyt-c1, CG4769) RNAi 1: *w-; cyt-c1 RNAi*  
1325 *(v109809)/+; srpHemo-Gal4, srpHemo-H2A::3xmCherry*, Complex III (UQCR-cp1,  
1326 CG3731) RNAi 2: *w-; UQCR-cp1 RNAi (v101350)/+; srpHemo-Gal4, srpHemo-*  
1327 *H2A::3xmCherry*, Complex III (UQCR-cp2, CG4169) RNAi 3: *w-; UQCR-cp2 RNAi*  
1328 *(v100818)/+; srpHemo-Gal4, srpHemo -H2A::3xmCherry*, Complex V (ATP synthase F1F0,  
1329 CG3612) RNAi: *w-; RNAi (v34664)/+; srpHemo-Gal4, srpHemo-H2A::3xmCherry*. **Fig. 6J:**  
1330 Control: *w-; +; srpHemo-Gal4, srpHemo-3xmCherry*, *atos* mutant: *w-; atossa<sup>BG02278</sup>;*  
1331 *srpHemo-Gal4, srpHemo-3xmCherry*, Control: *w/y,w[1118]; P{attP,y[+],w[3' ]/+;srpHemo-*  
1332 *Gal4, srpHemo-3xmCherry/+*, CG9253 RNAi (*porthos*): *w-; porthos RNAi (v36589)/+;*  
1333 *srpHemo-Gal4, srpHemo-3xmCherry/+*, Control: *w-; +; srpHemo-Gal4, srpHemo-*  
1334 *3xmCherry, CV-DN: w-;UAS-CV DN; srpHemo-Gal4, srpHemo-3xmCherry*.

1335 **Fig. 6SF:** Control: *w-; P{attP,y[+],w[3' ]/+; srpHemo-Gal4, srpHemo-H2A::3xmCherry,*  
1336 Complex III (Cyt-c1, CG4769) RNAi 1: *w-; cyt-c1 RNAi (v109809)/+; srpHemo-Gal4,*  
1337 *srpHemo-H2A::3xmCherry*, Complex III (UQCR-cp1, CG3731) RNAi 2: *w-; UQCR-cp1*  
1338 *RNAi (v101350)/+; srpHemo-Gal4, srpHemo-H2A::3xmCherry*, Complex III (UQCR-cp2,  
1339 CG4169) RNAi 3: *w-; UQCR-cp2 RNAi (v100818)/+; srpHemo-Gal4, srpHemo-*  
1340 *H2A::3xmCherry*, Complex V (ATP synthase F1F0, CG3612) RNAi: *w-; CG3612 RNAi*  
1341 *(v34664)/+; srpHemo-Gal4, srpHemo-H2A::3xmCherry*. **Figs. 6SG-H:** *w-; +; srpHemo-*  
1342 *Gal4, srpHemo-3xmCherry, atos* mutant: *w-; atossa<sup>BG02278</sup>;* *srpHemo-Gal4, srpHemo-*  
1343 *3xmCherry*, Control: *w/y,w[1118]; P{attP,y[+],w[3' ]/+;srpHemo-Gal4, srpHemo-*  
1344 *3xmCherry/+*, CG9253 RNAi (*porthos*): *w-; porthos RNAi (v36589)/+; srpHemo-Gal4,*  
1345 *srpHemo-H2A::3xmCherry/+*, Control: *w-; +; srpHemo-Gal4, srpHemo-3xmCherry, CV-*  
1346 *DN: w-;UAS-CV DN; srpHemo-Gal4, srpHemo-3xmCherry*

1347

### 1348 **Figures 7 and S7:**

1349 **Figs. 7B-H, SB-I:** Control: *w-; +; srpHemo-3xmCherry*, mutant: *w-; atossa<sup>BG02278</sup>;*  
1350 *srpHemo-3xmCherry*.

### 1351 **Resource Availability:**

1352 Fly lines, plasmids and other reagents utilized are available upon request from the Lead  
1353 contact: [daria.siekhaus@ist.ac.at](mailto:daria.siekhaus@ist.ac.at)

1354 Original reads from RNA sequencing and Polysome profiling has been deposited at: (will be  
1355 done once paper is in revision).

### 1356 **REFERENCES**

1357

1358 Anders, S., Huber, W. (2010). Differential expression analysis for sequence count data. *Genome Biol.* 11,

- 1359 R106.  
1360  
1361 Angelin, A., Gil-de-Gómez, L., Dahiya, S., Jiao, J., Guo, L., Levine, M.H., Wang, Z., Quinn W.J.3rd,  
1362 Kopinski, P.K., Wang L., Akimova, T., Liu Y., Bhatti, T.R., Han, R., Laskin, B.L., Baur, J.A., Blair, I.A.,  
1363 Wallace, D.C., Hancock, W.W., Beier, U.H. (2017). Foxp3 reprograms T cell metabolism to function in low-  
1364 glucose, high-lactate environments. *Cell Metab.* 6, 1282–1293.  
1365  
1366 Bassett, A., Liu, J.L. (2014). CRISPR/Cas9 mediated genome engineering in *Drosophila*. *Methods* 69, 128–  
1367 136.  
1368  
1369 Bailey, T.L., Boden, M., Buske, F.A., Frith, M., Grant, C.E., Clementi, L., Ren, J., Li, W.W., Noble, W.S.  
1370 (2009). MEME SUITE: tools for motif discovery and searching. *Nucleic Acids Res.* 37, 202–208.  
1371  
1372 Bao, Y., Ledderose, C., Graf, A.F., Brix, B., Birsak, T., Lee, A., Zhang, J., Junger, W.G. (2015). mTOR and  
1373 differential activation of mitochondria orchestrate neutrophil chemotaxis. *J. Cell Biol.* 7, 1153–1164.  
1374  
1375 Baßler, J., Hurt, E. (2019). Eukaryotic ribosome assembly. *Annu. Rev. Biochem.* 88, 281–306.  
1376  
1377 Beecham, G.W., Hamilton, K., Naj, A.C., Martin, E.R., Huentelman, M., Myers, A.J., Comeveaux, J.J.,  
1378 Hardy, J., Vonsattel, J.P., Younkin, S.G., et al. (2014). Genome-wide association meta-analysis of  
1379 neuropathologic features of Alzheimer's disease and related dementias. *PLoS Genet.* 9, e1004606.  
1380  
1381 Belogradov, G.I. (2002). Factor B is essential for ATP synthesis by mitochondria. *Arch. Biochem. Biophys.*  
1382 2, 271-274.  
1383  
1384 Belogradov, G.I. (2008). The proximal N-terminal amino acid residues are required for the coupling activity  
1385 of the bovine heart mitochondrial factor B. *Arch. Biochem. Biophys.* 1, 76–87.  
1386  
1387 Belyaeva, V., Wachner, S., Gridchyn, I., Linder, M., Emtenani, S., Gyoergy, A., Sibilia, M., Siekhaus, D.  
1388 (2020). Cortical actin properties controlled by *Drosophila* Fos aid macrophage infiltration against  
1389 surrounding tissue resistance. *BioRxiv*. <https://doi.org/10.1101/2020.09.18.301481>  
1390  
1391 Berg, J., Tymoczko, J., Stryer, L. (2002). *Biochemistry*. New York: W.H. Freeman, p. Chapter 17.  
1392  
1393 Bernstein, B.W., Bamburg, J.R. (2003). Actin-ATP hydrolysis is a major energy drain for neurons. *J.*  
1394 *Neurosci.* 23, 1–6.  
1395  
1396 Bischof, J., Maeda, R.K., Hediger, M., Karch, F., Basler, K. (2007). An optimized transgenesis system for  
1397 *Drosophila* using germ-line-specific uC31 integrases. *Proc. Natl. Acad. Sci. USA* 104, 3312–3317.  
1398  
1399 Bhattacharjee, J.K. (1985). a-Amino-adipate pathway for the biosynthesis of lysine in lower eukaryotes. *Crit.*  
1400 *Rev. Microbiol.* 12, 131–151.  
1401  
1402 Bodor, D.L., Pönisch, W., Endres, R.G., Paluch, E.K. (2020). Of cell shapes and motion: the physical basis of  
1403 animal cell migration. *Dev. Cell* 5, 550–562.  
1404  
1405 Booth, M.P.S., Connors, R., Rumsby, G., Brady, R.L. (2006). Structural basis of substrate specificity in  
1406 human Glyoxylate Reductase/Hydroxypyruvate Reductase. *J. Mol. Biol.* 360, 178–189.  
1407  
1408 Bourgeois, C.F., Mortreux, F., Auboef, D. (2016). The multiple functions of RNA helicases as drivers and  
1409 regulators of gene expression. *Mol. Cell. Bio.* 17, 426–438.  
1410  
1411 Brandt, T., Mourier, A., Tain, L.S., Partridge, L., Larsson, N.G., Kühlbrandt, W. (2017). Changes of  
1412 mitochondrial ultrastructure and function during ageing in mice and *Drosophila*. *Elife* 6, e24662.  
1413  
1414 Brückner, K., Kockel, L., Duchek, P., Luque, C.M., Rørth, P., Perrimon, N. (2004). The PDGF/VEGF  
1415 receptor controls blood cell survival in *Drosophila*. *Dev. Cell* 7, 73–84.  
1416  
1417 Buck, M.D., O'Sullivan, D., Klein Geltink, R.I., Curtis, J.D., Chang, C.H., Sanin, D.E., Qiu, J., Kretz, O.,  
1418 Braas, D., van der Windt, G.J., Chen, Q., Huang, S.C., O'Neill, C.M., Edelson, B.T., Pearce, E.J., Sesaki, H.,

- 1419 Huber, T.B., Rambold, A.S., Pearce, E.L. (2016). Mitochondrial dynamics controls T cell fate through  
1420 metabolic programming. *Cell* 166, 63–76.  
1421
- 1422 Bunt, S., Hooley, C., Hu, N., Scahill, C., Weavers, H., Skaer, H. (2010). Hemocyte-eecreted Type IV collagen  
1423 enhances BMP signaling to guide renal tubule morphogenesis in *Drosophila*. *Dev. Cell* 19, 296–306.  
1424
- 1425 Calvo, S.E., Tucker, E.J., Compton, A.G., Kirby, D.M., Crawford, G., Burt, N.P., Rivas, M., Guiducci, C.,  
1426 Bruno, D.L., Goldberger, O.A., Redman, M.C., Wiltshire, E., Wilson, C.J., Altshuler, D., Gabriel, S.B., Daly,  
1427 M.J., Thorburn, D.R., Mootha, V.K. (2010). High-throughput, pooled sequencing identifies mutations in  
1428 NUBPL and FOXRED1 in human complex I deficiency. *Nat. Genet.* 10, 851–858.  
1429
- 1430 Caputa, G., Castoldi, A., Pearce, E.J. (2019). Metabolic adaptations of tissue-resident immune cells. *Nat.*  
1431 *Immunol.* 20, 793–801.  
1432
- 1433 Cho, N.K., Keyes, L., Johnson, E., Heller, J., Ryner, L., Karim, F., Krasnow, M.A. (2002). Developmental  
1434 control of blood cell migration by the *Drosophila* VEGF pathway. *Cell* 108, 865–876.  
1435
- 1436 Commander, R., Wei, C., Sharma, A., Mouw, J.K., Burton, L.J., Summerbell, E., Mahboubi, D., Peterson,  
1437 R.J., Konen, J., Zhou, W., Du, Y., Fu, H., Shanmugam, M., Marcus, A.I. (2020). Subpopulation targeting of  
1438 pyruvate dehydrogenase and GLUT1 decouples metabolic heterogeneity during collective cancer cell  
1439 invasion. *Nat. Commun.* 1, 1533.  
1440
- 1441 Cui L, Jeong H, Borovecki F, Parkhurst CN, Tanese N, Krainc D. (2006). Transcriptional repression of PGC-  
1442 1alpha by mutant huntingtin leads to mitochondrial dysfunction and neurodegeneration. *Cell* 1, 59–69.  
1443
- 1444 Cunniff, B., McKenzie, A.J., Heintz, N.H., Howe, A.K. (2016). AMPK activity regulates trafficking of  
1445 mitochondria to the leading edge during cell migration and matrix invasion. *Mol. Biol. Cell* 17, 2662–2674.  
1446
- 1447 Cuvelier, D., Thery, M., Chu, Y.S., Dufour, S., Thiery, J.P., Bornens, M., Nassoy, P., Mahadevan, L. (2007).  
1448 The universal dynamics of cell spreading. *Curr. Biol.* 17, 694–699.  
1449
- 1450 Davies, K.M., Strauss, M., Daum, B., Kief, J.H., Osiewacz, H.D., Rycovska, A., Zickermann, V., Kühlbrandt,  
1451 W. (2011). Macromolecular organization of ATP synthase and complex I in whole mitochondria. *Proc. Nat.*  
1452 *Acad. Sci. USA* 34, 14121–14126.  
1453
- 1454 Davies, G., Lam, M., Harris, S.E., Trampush, J.W., Luciano, M., Hill, W.D., Hagens, S.P., Ritchie, S.J.,  
1455 Marioni, R.E., Fawns-Ritchie, C., et al. (2018). Study of 300,486 individuals identifies 148 independent  
1456 genetic loci influencing general cognitive function. *Nat. Commun.* 1, 2098.  
1457
- 1458 Dennerlein, S., Oeljeklaus, S., Jans, D., Hellwig, C., Bareth, B., Jakobs, S., Deckers, M., Warscheid, B.,  
1459 Rehling, P. (2015). MITRAC7 acts as a COX1-specific chaperone and reveals a checkpoint during  
1460 cytochrome c oxidase assembly. *Cell Rep.* 10, 1644–1655.  
1461
- 1462 Dietzl, G., Chen, D., Schnorrer, F., Su, K.C., Barinova, Y., Fellner, M., Gasser, B., Kinsey, K., Oettel, S.,  
1463 Scheiblauer, S., Couto, A., Marra, V., Keleman, K., Dickson, B.J. (2007). A genome-wide transgenic RNAi  
1464 library for conditional gene inactivation in *Drosophila*. *Nature* 7150, 151–156.  
1465
- 1466 Dobin, A., Davis, C.A., Schlesinger, F., Drenkow, ., Zaleski, C., Jha, S., Batut, P., Chaisson, M., Gingeras,  
1467 T.R. (2013). STAR: ultrafast universal RNA-seq aligner. *Bioinformatics* 29, 15–21.  
1468
- 1469 Flora, P., Wong-Deyrup, S.W., Martin, E.T., Palumbo, R.J., Nasrallah, M., Oligney, A., Blatt, P., Patel, D.,  
1470 Fuchs, G., Rangan, P. (2018). Sequential regulation of maternal mRNAs through a conserved cis-acting  
1471 element in their 3' UTRs. *Cell Rep.* 25, 3828–3843.  
1472
- 1473 Formosa, L.E., Mimaki, M., Frazier, A.E., McKenzie, M., Stait, T.L., Thorburn, D.R., Stroud, D.A., Ryan,  
1474 M.T. (2015). Characterization of mitochondrial FOXRED1 in the assembly of respiratory chain complex I.  
1475 *Hum. Mol. Genet.* 20, 2952–2965.  
1476
- 1477 Freije, W.A., Mandal, S., Banerjee, U. (2012). Expression profiling of attenuated mitochondrial function

- 1478 identifies retrograde signals in *Drosophila*. *G3: Gene Genom. Genet* 2: 843–851.  
1479  
1480 Garcia, I., Albring, M.J., Uhlenbeck, O.C. (2012). Duplex destabilization by four ribosomal DEAD-box  
1481 proteins. *Biochem. J.* 453, 10109–10118.  
1482  
1483 Guak, H., Al Habyan, S., Ma, E.H., Aldossary, H., Al-Masri, M., Won, S.Y., Ying, T., Fixman, E.D., Jones,  
1484 R.G., McCaffrey, L.M., Krawczyk, C.M. (2018). Glycolytic metabolism is essential for CCR7  
1485 oligomerization and dendritic cell migration. *Nat. Commun.* 9, 2463.  
1486  
1487 Guak, H., Krawczyk, C.M. (2020). Implications of cellular metabolism for immune cell migration.  
1488 *Immunology* 161, 200–208.  
1489  
1490 Gyoergy, A., Roblek, M., Ratheesh, A., Valoskova, K., Belyaeva, V., Wachner, S., Matsubayashi, Y.,  
1491 Sa´nchez-Sa´nchez, B.J., Stramer, B., Siekhaus, D.E. 2018. Tools allowing independent visualization and  
1492 genetic manipulation of *Drosophila melanogaster* macrophages and surrounding tissues. *G3: Gene Genom.*  
1493 *Genet.* 8, 845–857.  
1494  
1495 Hahn, A., Parey, K., Bublitz, M., Mills, D.J., Zickermann, V., Vonck, J., Khlbrandt, W., Meier, T. (2016).  
1496 Structure of a complete ATP synthase dimer reveals the molecular basis of inner mitochondrial membrane  
1497 morphology. *Mol. Cell* 61, 445–456.  
1498  
1499 Hall, C.N., Klein-Flgge, M.C., Howarth, C., Attwell, D. (2012). Oxidative phosphorylation, not glycolysis,  
1500 powers presynaptic and postsynaptic mechanisms underlying brain information processing. *J. Neurosci.* 32,  
1501 8940–8951.  
1502  
1503 Hurd, T.R., Herrmann, B., Sauerwald, J., Sanny, J., Grosch, M., Lehmann, R. (2016). Long Oskar controls  
1504 mitochondrial inheritance in *Drosophila melanogaster*. *Dev. Cell* 39, 560–571.  
1505  
1506 Httemann, M., Lee, I., Samavati, L., Yu, H., Doan, J.W. (2007). Regulation of mitochondrial oxidative  
1507 phosphorylation through cell signaling. *Biochim. Biophys. Acta.* 1773, 1701–1720.  
1508  
1509 Kelley, L.C., Chi, Q., Ca´ceres, R., Hastie, E., Schindler, A.J., Jiang, Y., Matus, D.Q., Plastino, J., Sherwood,  
1510 D.R. (2019). Adaptive F-actin polymerization and localized ATP production drive basement membrane  
1511 invasion in the absence of MMPs. *Dev. Cell* 48, 313–328.  
1512  
1513 Khalil, A.A., Friedl, P. (2010). Determinants of leader cells in collective cell migration. *Integr. Biol. (Camb.)*  
1514 2, 568–574.  
1515  
1516 Kierdorf, K., Prinz, M., Geissmann, F., Gomez Perdiguero, E. (2015). Development and function of tissue  
1517 resident macrophages in mice. *Semin. Immunol.* 6, 369–378.  
1518  
1519 Kim, D., Langmead, B., Salzberg, S.L. (2015). HISAT: a fast spliced aligner with low memory  
1520 requirements. *Nat. Methods* 12, 357–360.  
1521  
1522 Kishore, M., Cheung, K.C.P., Fu, H., Bonacina, F., Wang, G., Coe D., Ward, E.J., Colamatteo, A., Jangani,  
1523 M, Baragetti, A., Matarese, G., Smith, DM, Haas, R, Mauro, C., Wraith, D.C., Okkenhaug, K., Catapano,  
1524 A.L., De Rosa, V., Norata, G.D., Marelli-Berg, F.M. (2018). Regulatory T cell migration is dependent on  
1525 glucokinase-mediated glycolysis. *Immunity* 48, 831–832.  
1526  
1527 Koopman, W.J., Distelmaier, F., Smeitink, J.A., Willems, P.H. (2013). OXPHOS mutations and  
1528 neurodegeneration. *EMBO J.* 32, 9–29.  
1529  
1530 Kurosaka, S., Kashina, A. (2008). Cell biology of embryonic migration. *Birth Defects Res. C: Embryo*  
1531 *Today* 84, 102–122.  
1532  
1533 LeBleu, V.S., O’Connell, J.T., Gonzalez Herrera, K.N., Wikman, H., Pantel, K., Haigis, M.C., de Carvalho,  
1534 F.M., Damascena, A., Domingos Chinen, L.T., Rocha, R.M., Asara, J.M., Kalluri, R. (2014). PGC-1 $\alpha$   
1535 mediates mitochondrial biogenesis and oxidative phosphorylation in cancer cells to promote metastasis. *Nat.*  
1536 *Cell Biol.* 16, 992–1003.  
1537

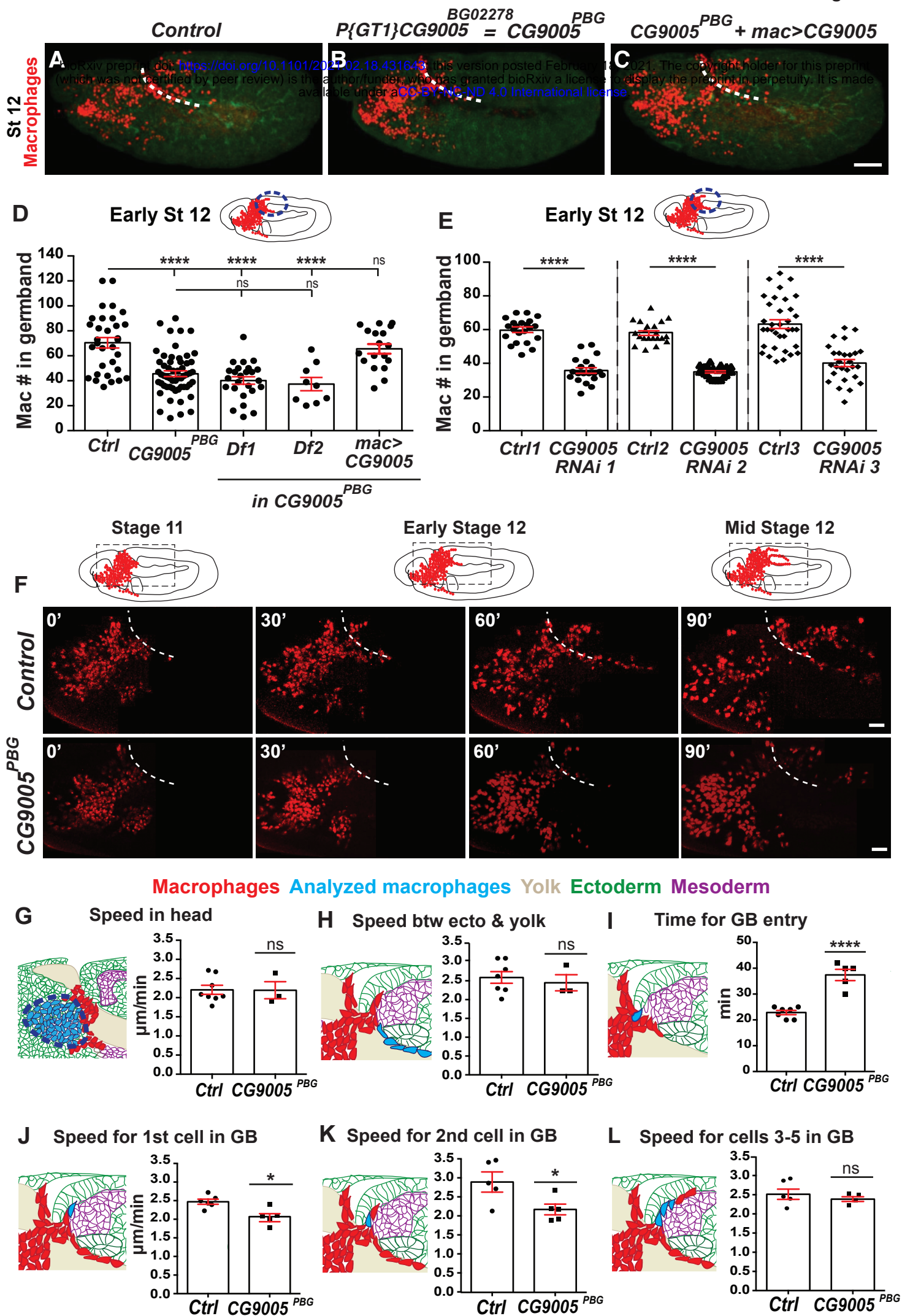
- 1538 Lieber, T., Jeedigunta, S.P., Palozzi, J.M., Lehmann, R., Hurd, T.R. (2019). Mitochondrial fragmentation  
1539 drives selective removal of deleterious mtDNA in the germline. *Nature* 570, 380–384.  
1540
- 1541 Lin, J., Handschin, C., Spiegelman, B.M. (2005). Metabolic control through the PGC-1 family of transcription  
1542 coactivators. *Cell Metab.* 6, 361–370.  
1543
- 1544 Liu, J., Zhang, X., Chen, K., Cheng, Y., Liu, S., Xia, M., Chen, Y., Zhu, H., Li, Z., Cao, X. (2019). CCR7  
1545 Chemokine receptor-inducible *Inc-Dpf3* restrains dendritic cell migration by inhibiting HIF-1 $\alpha$ -mediated  
1546 glycolysis. *Immunity* 3, 600–615.  
1547
- 1548 Llufrío, E.M., Wang, L., Naser, F.J., Patti, G.J. (2018). Sorting cells alters their redox state and cellular  
1549 metabolome. *Redox Biol.* 16, 381–387.  
1550
- 1551 Luster, A.D., Alon, R., von Andrian, U.H. (2005). Immune cell migration in inflammation: present and future  
1552 therapeutic targets. *Nat. Immunol.* 12, 1182–1190.  
1553
- 1554 Mannella, C.A. (2020). Consequences of folding the mitochondrial inner membrane. *Front. Physiol.* 1, 536.  
1555
- 1556 Martin, E., Blatt, P., Ngyuen, E., Lahr, R., Yoon, H., Pocchiari, T., Berman, A., Emtenani, S., Siekhaus, D.,  
1557 Fuchs, G., Rangan, P. (2021). Ribosome biogenesis promotes germline stem cell differentiation through  
1558 translation regulation of a p53 repressor during *Drosophila* oogenesis (paper in submission).  
1559
- 1560 Martínez-Reyes, I., Chandel, N.S. (2020). Mitochondrial TCA cycle metabolites control physiology and  
1561 disease. *Nat. Commun.* 11, 102.  
1562
- 1563 Masopust, D., Schenkel, J.M. (2013). The integration of T cell migration, differentiation and function. *Nat.*  
1564 *Rev. Immunol.* 5, 309–320.  
1565
- 1566 Mookerjee, S.A., Gerencser, A.A., Nicholls, D.G., Brand, M.D. (2017). Quantifying intracellular rates of  
1567 glycolytic and oxidative ATP production and consumption using extracellular flux measurements. *J. Biol.*  
1568 *Chem.* 292, 7189–7207.  
1569
- 1570 Nicholson, L.B. (2016). The immune system. *Essays Biochem.* 3, 275–301.  
1571
- 1572 Nourshargh, S., Alon, R. (2014). Immune cell invasion and function leukocyte migration into inflamed  
1573 tissues. *Immunity* 41, 694–707.  
1574
- 1575 O'Day, C.L., Chavanikamannil, F., Abelson, J. (1996). 18S rRNA processing requires the RNA helicase-like  
1576 protein Rrp3. *Nucleic Acids Res.* 16, 3201–3207.  
1577
- 1578 Oka, T., Sayano, T., Tamai, S., Yokota, S., Kato H, Fujii G, Mihara K. 2008. Identification of a novel protein  
1579 MICS1 that is involved in maintenance of mitochondrial morphology and apoptotic release of cytochrome c.  
1580 *Mol. Biol. Cell* 6, 2597–608.  
1581
- 1582 O'Neill, L.A., Kishton, R.J., Rathmell, J. (2016). A guide to immunometabolism for immunologists. *Nat. Rev.*  
1583 *Immunol.* 9, 553–565.  
1584
- 1585 Patel, M.S., Nemeria, N.S., Furey, W., Jordan, F. (2014). The pyruvate dehydrogenase complexes: structure-  
1586 based function and regulation. *J. Biol. Chem.* 289, 16615–16623.  
1587
- 1588 Pavlova, N.N., Thompson, C.B. (2016). The emerging hallmarks of cancer metabolism. *Cell Metab.* 1, 27–47.  
1589
- 1590 Price, M.J., Patterson, D.G., Scharer, C.D., Boss, J.M. (2018). Progressive upregulation of oxidative  
1591 metabolism facilitates plasmablast differentiation to a T-independent antigen. *Cell Rep.* 11, 3152–3159.  
1592
- 1593 Puchalska, P., Crawford, P.A. (2017). Multi-dimensional roles of ketone bodies in fuel metabolism,  
1594 Signaling, and Therapeutics. *Cell Metab.* 2, 262–284.  
1595
- 1596 Raichle, M.E., Gusnard, D.A. (2002). Appraising the brain's energy budget. *Proc. Nat. Acad. Sci. USA* 16,



- 1597 10237–10239.
- 1598
- 1599 Rambold, A.S., Cohen, S., Lippincott-Schwartz, J. (2015). Fatty acid trafficking in starved cells: regulation by
- 1600 lipid droplet lipolysis, autophagy, and mitochondrial fusion dynamics. *Dev. Cell* 6, 678-692.
- 1601
- 1602 Rao, S., Mondragón, L., Pranjić, B., Hanada, T., Stoll, G., Köcher, T., Zhang, P., Jais, A., Lercher, A.,
- 1603 Bergthaler, A., Schramek, D., Haigh, K., Sica, V., Leduc, M., Modjtahedi, N., Pai, T.P., Onji, M., Uribealag,
- 1604 I., Hanada, R., Kozieradzki, I., Kogelgruber, R., Cronin, S.J., She, Z., uehenberger, F.Q. (2019). AIF-regulated
- 1605 oxidative phosphorylation supports lung cancer development. *Cell Res.* 29, 579–591.
- 1606
- 1607 Ratheesh, A., Belyaeva, V., and Siekhaus, D.E. 2015. *Drosophila* immune cell migration and adhesion during
- 1608 embryonic development and larval immune responses. *Curr. Opin. Cell Biol.* 36, 71–79.
- 1609
- 1610 Ratheesh, A., Biebl, J., Vesela, J., Smutny, M., Papusheva, E., Krens, S.F.G., Kaufmann, W., Gyoergy, A.,
- 1611 Casano, A.M., Siekhaus, D.E. (2018). *Drosophila* TNF modulates tissue tension in the embryo to facilitate
- 1612 macrophage invasive migration. *Dev. Cell* 3, 331–346.
- 1613
- 1614 Riera-Domingo, C., Audigé, A., Granja, S., Cheng, W.C., Ho, P.C., Baltazar, F., Stockmann, C., Mazzone, M.
- 1615 (2020). Immunity, hypoxia, and metabolism- the ménage a trois of cancer: implications for immunotrophy.
- 1616 *Physiol. Rev.* 100, 100–102.
- 1617
- 1618 Rottner, K., Schaks, M. (2019). Assembling actin filaments for protrusion. *Curr. Opin. Cell Biol.* 56, 53–63.
- 1619
- 1620 Sekiguchi, T., Hayano, T., Yanagida, M., Takahashi, N., Nishimoto, T. (2006). NOP132 is required for proper
- 1621 nucleolus localization of DEAD-box RNA helicase DDX47. *Nucleic Acids Res.* 16, 4593–4608.
- 1622
- 1623 Semba, H., Takeda, N., Isagawa, T., Sugiura, Y., Honda, K., Wake, M., Miyazawa, H., Yamaguchi, Y.,
- 1624 Miura, M., Jenkins, D.M., Choi, H., Kim, J.W., Asagiri, M., Cowburn, A.S., Abe, H., Soma, K., Koyama, K.,
- 1625 Katoh, M., Sayama, K., Goda, N., Johnson, R.S., Manabe, I., Nagai, R., Komuro, I. (2016). HIF-1 $\alpha$ -PDK1
- 1626 axis-induced active glycolysis plays an essential role in macrophage migratory capacity. *Nat. Commun.* 7,
- 1627 11635.
- 1628
- 1629 Sherva, R., Gross, A., Mukherjee, S., Koesterer, R., Amouyel, P., Bellenguez, C., Dufouil, C., Bennett, D.A.,
- 1630 Chibnik, L., Cruchaga, C., Del-Aguila, J., Farrer, L.A., Mayeux, R., Munsie, L., Winslow, A., Newhouse, S.,
- 1631 Saykin, A.J., Kauwe, J.S.K., Crane, P.K., Green, R.C. (2020). Genome-wide association study of rate of
- 1632 cognitive decline in Alzheimer's disease patients identifies novel genes and pathways. *Alzheimers Dement.* 8,
- 1633 1134–1145.
- 1634
- 1635 Shin, B., Benavides, G.A., Geng, J., Koralov, S.B., Hu, H., Darley-USmar, V.M., Harrington, L.E. (2020).
- 1636 Mitochondrial oxidative phosphorylation regulates the fate decision between pathogenic Th17 and regulatory
- 1637 T cells. *Cell Rep.* 6,1898–1909.
- 1638
- 1639 Siekhaus, D., Haesemeyer, M., Moffitt, O., Lehmann, R. (2010). RhoL controls invasion and Rap1
- 1640 localization during immune cell transmigration in *Drosophila*. *Nat. Cell Biol.* 12, 605–610.
- 1641
- 1642 Smutny, M., A'kos, Z., Grigolon, S., Shamipour, S., Ruprecht, V., Capek, D., Behrndt ,M, Papusheva, E,
- 1643 Tada, M., Hof, B., Salbreux, G., Heisenberg ,C.P. (2017). Friction forces position the neural anlage. *Nat. Cell*
- 1644 *Biol.* 19, 306–317.
- 1645
- 1646 Sreekumar, A., Poisson, L.M., Rajendiran, T.M., Khan, AP, Cao, Q., Yu, J., Laxman, B., Mehra, R., Lonigro,
- 1647 R.J., Li, Y., Nyati, M.K., Ahsan, A, Kalyana-Sundaram, S, Han, B., Cao X, Byun, J, Omenn, G.S., Ghosh, D.,
- 1648 Pennathur, S., Alexander, D.C., Berger, A., Shuster, J.R., Wei, J.T., Varambally, S., Beecher, C., Chinnaiyan,
- 1649 AM. (2009). Metabolomic profiles delineate potential role for sarcosine in prostate cancer progression. *Nature*
- 1650 457, 910–914.
- 1651
- 1652 Tabata, S., Yamamoto, M., Goto, H., Hirayama, A., Ohishi, M., Kuramoto, T., Mitsuhashi, A., Ikeda, R.,
- 1653 Haraguchi, M., Kawahara K., Shinsato, Y., Minami, K., Saijo, A., Hanibuchi, M., Nishioka, Y., Sone, S.,
- 1654 Esumi, H., Tomita, M., Soga, T., Furukawa, T, Akiyama, S.I. (2017). Thymidine catabolism as a metabolic
- 1655 strategy for cancer survival. *Cell Rep.* 7, 1313–1321.

- 1656  
1657 Thurmond, J., Goodman, J.L., Strelets, V.B., Attrill, H., Gramates, L.S., Marygold, S.J., Matthews, B.B.,  
1658 Millburn, G., Antonazzo, G., Trovisco, V., Kaufman, T.C., Calvi, B.R. (2019). FlyBase Consortium. FlyBase  
1659 2.0: the next generation. *Nucleic Acids Res.* 47, 759–765.
- 1660  
1661 Tomancak, P., Beaton, A., Weiszmam, R., Kwan, E., Shu, S., Lewis, S.E., Richards, S., Ashburner, M.,  
1662 Hartenstein, V., Celniker, S.E., Rubin, G.M. (2002). Systematic determination of patterns of gene expression  
1663 during *Drosophila* embryogenesis. *Genome Biol.* 12, RESEARCH0088.
- 1664  
1665 Tomancak, P., Berman, B.P., Beaton, A., Weiszmam, R., Kwan, E., Hartenstein, V., Celniker, S.E., Rubin,  
1666 G.M. (2007). Global analysis of patterns of gene expression during *Drosophila* embryogenesis. *Genome Biol.*  
1667 7, R145.
- 1668  
1669 Valoskova, K., Biebl, J., Roblek, M., Emtenani, S., Gyoergy, A., Misova, M., Ratheesh, A., Reis-Rodrigues,  
1670 P., Shkarina, K., Larsen, I.S.B., Vakhrushev, S.Y., Clausen, H., Siekhaus, D.E. (2019). A conserved major  
1671 facilitator superfamily member orchestrates a subset of O-glycosylation to aid macrophage tissue invasion.  
1672 *eLife* 8, e41801.
- 1673  
1674 Vander Heiden, M.G., Cantley, L.C., Thompson, C.B. (2009). Understanding the Warburg effect: the  
1675 metabolic requirements of cell proliferation. *Science* 324, 1029–1033.
- 1676  
1677 van der Windt, G.J., Everts, B., Chang, C.H., Curtis, J.D., Freitas, T.C., Amiel, E., Pearce, E.J., Pearce, E.L.  
1678 (2012). Mitochondrial respiratory capacity is a critical regulator of CD8+ T cell memory development.  
1679 *Immunity* 1, 68–78.
- 1680  
1681 van der Windt, G.J., O'Sullivan, D., Everts, B., Huang, S.C., Buck, M.D., Curtis, J.D., Chang, C.H., Smith,  
1682 A.M., Ai, T., Faubert, B., Jones, R.G., Pearce, E.J., Pearce, E.L. (2013). CD8 memory T cells have a  
1683 bioenergetic advantage that underlies their rapid recall ability. *Proc. Natl. Acad. Sci. USA* 35, 14336–14341.
- 1684  
1685 Vats, D., Mukundan, L., Odegaard, J.I., Zhang, L., Smith, K.L., Morel, C.R., Greaves, D.R., Murray, P.J.,  
1686 Chawla, A. (2006). Oxidative metabolism and PGC-1 $\beta$  attenuate macrophage mediated inflammation. *Cell*  
1687 *Metab.* 4, 13–24.
- 1688  
1689 Venema, J., Cile Bousquet-Antonelli, C., Gelugne, J.P., Le Caizergues-Ferrer, M., Tollervey, D. (1997).  
1690 Rok1p is a putative RNA helicase required for rRNA processing. *Mol. Cell Biol.* 17, 3398–3407.
- 1691  
1692 Venema, J., Tollervey, D. (1995). Processing of pre-ribosomal RNA in *Saccharomyces cerevisiae*. *Yeast* 11,  
1693 1629–1650.
- 1694  
1695 Wang, H., Yang, J., Schneider, J.A., De Jager, P.L., Bennett, D.A., Zhang, H.Y. (2020). Genome-wide  
1696 interaction analysis of pathological hallmarks in Alzheimer's disease. *Neurobiol. Aging.* 93, 61–68.
- 1697  
1698 Weavers, H., Martin, P. (2020). The cell biology of inflammation: from common traits to remarkable  
1699 immunological adaptations. *J. Cell Biol.* 7, e202004003.
- 1700  
1701 Weavers, H., Evans, I.R., Martin, P., Wood, W. (2016). Corpse engulfment generates a molecular memory  
1702 that primes the macrophage inflammatory response. *Cell* 165, 1658–1671.
- 1703  
1704 Weinberg, S.E., Singer, B.D., Steinert, E.M., Martinez, C.A., Mehta, M.M., Martínez-Reyes, I., Gao, P.,  
1705 Helmin, K.A., Abdala-Valencia, H., Sena, L.A., Schumacker, P.T., Turka, L.A., Chandel, N.S. (2019).  
1706 Mitochondrial complex III is essential for suppressive function of regulatory T cells. *Nature* 7740, 495–499.
- 1707  
1708 Weydt, P., Pineda, V.V., Torrence, A.E., Libby, R.T., Satterfield, T.F., Lazarowski, E.R., Gilbert, M.L.,  
1709 Morton, G.J., Bammler, T.K., Strand, A.D., Cui, L., Beyer, R.P., Easley, C.N., Smith, A.C., Krainc, D.,  
1710 Luquet, S., Sweet, I.R., Schwartz, M.W., La Spada, A.R. (2006). Thermoregulatory and metabolic defects in  
1711 Huntington's disease transgenic mice implicate PGC-1 $\alpha$  in Huntington's disease neurodegeneration. *Cell*  
1712 *Metab.* 5, 349–362.
- 1713  
1714 Wood, W., Martin, P. (2017). Macrophage functions in tissue patterning and disease: new insights from the

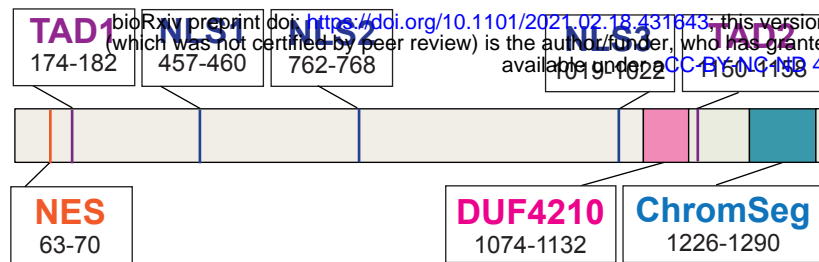
- 1715 fly. Dev. Cell 40, 221–233.  
1716  
1717 Wood, W., Faria, C., Jacinto, A. (2006). Distinct mechanisms regulate hemocyte chemotaxis during  
1718 development and wound healing in *Drosophila melanogaster*. J. Cell Biol. 3, 405–416.  
1719  
1720 Woodcock, K.J., Kierdorf, K., Pouchelon, C.A. Vivancos, V., Dionne, M.S., Geissmann, F. (2015).  
1721 Macrophage-derived upd3 cytokine causes impaired glucose homeostasis and reduced lifespan in *Drosophila*  
1722 fed a lipid-rich diet. Immunity 1, 133–144.  
1723  
1724 Wu, D., Sanin, D.E., Everts, B., Chen, Q., Qiu, J., Buck, M.D., Patterson, A., Smith, A.M., Chang, C.H., Liu,  
1725 Z., Artyomov, M.N., Pearce, E.L., Cella, M., Pearce, E.J. (2016). Type 1 interferons induce changes in core  
1726 metabolism that are critical for immune function. Immunity. 6, 1325–1336.  
1727  
1728 Zanotelli, M.R., Goldblatta, Z.E., Millera, J.P., Bordeleau, F., Lia J., Vander Burgha, J.A., Lampia, M.C.,  
1729 Kinga, M.R., Reinhart-Kinga, A. (2018). Regulation of ATP utilization during metastatic cell migration by  
1730 collagen architecture. Mol. Biol. Cell 1, 1-9.  
1731  
1732 Zanotelli, M.R., Rahman-Zaman, A., Vander Burgh, J.A., Taufalele, P.V., Jain, A., Erickson, D., Bordeleau,  
1733 F., Reinhart-King, C.A. (2019). Energetic costs regulated by cell mechanics and confinement are predictive of  
1734 migration path during decision-making. Nat. Commun. 1, 4185.  
1735  
1736 Zhang, J., Goliwas, K.F., Wang, W., Taufalele, P.V., Bordeleau, F., Reinhart-King, C.A. (2019). Energetic  
1737 regulation of coordinated leader-follower dynamics during collective invasion of breast cancer cells. Proc.  
1738 Natl. Acad. Sci. USA 16, 7867–7872.  
1739  
1740 Zhang, W.C., Shyh-Chang, N., Yang, H., Rai, A., Umashankar, S., Ma, S., Soh, B.S., Sun, L.L., Tai, B.C.,  
1741 Nga, M.E., Bhakoo, K.K., Jayapal, S.R., Nichane, M., Yu, Q., Ahmed, D.A., Tan, C., Sing, W.P., Tam, J.,  
1742 Thirugananam, A., Soroush Noghabi, M., Pang, Y.H., Ang, H.S., Mitchell, W., Robson, P., Kaldis, P., Soo,  
1743 R.A., Swarup, S., Lim, E.H., Lim, B. (2012). Glycine decarboxylase activity drives non-small cell lung cancer  
1744 tumor-initiating cells and tumorigenesis. Cell 148, 259–272.  
1745  
1746 Zheng, X., Boyer, L., Jin, M., Mertens, J., Kim, Y., Ma, L., Ma, L., Hamm, M., Gage, F.H., Hunter, T.  
1747 (2016). Metabolic reprogramming during neuronal differentiation from aerobic glycolysis to neuronal  
1748 oxidative phosphorylation. Elife. 5, e13374.  
1749  
1750 Zheng, B., Liao, Z., Locascio, J.J., Lesniak, K.A., Roderick, S.S., Watt, M.L., Eklund, A.C., Zhang-James,  
1751 Y., Kim, P.D., Hauser, M.A., et al. (2010). PGC-1 $\alpha$ , a potential therapeutic target for early intervention in  
1752 Parkinson's disease. Sci. Transl. Med. 52, 52ra73.  
1753  
1754 Zhou, W., Cao, L., Jeffries, J., Zhu, X., Staiger, C.J., Deng, Q. (2018). Neutrophil-specific knockout  
1755 demonstrates a role for mitochondria in regulating neutrophil motility in zebrafish. Dis. Model Mech. 3,  
1756 dmm033027.



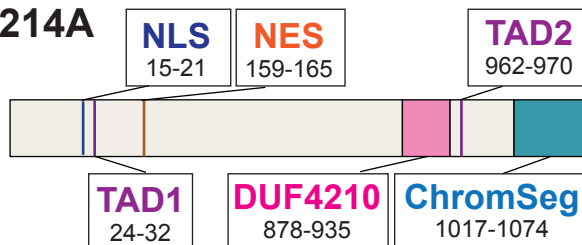


A

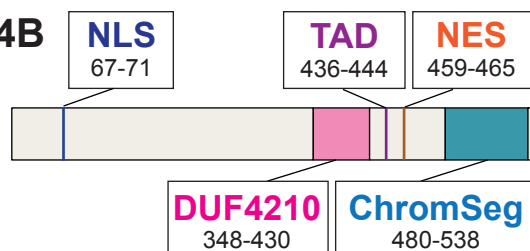
## CG9005 = Atossa



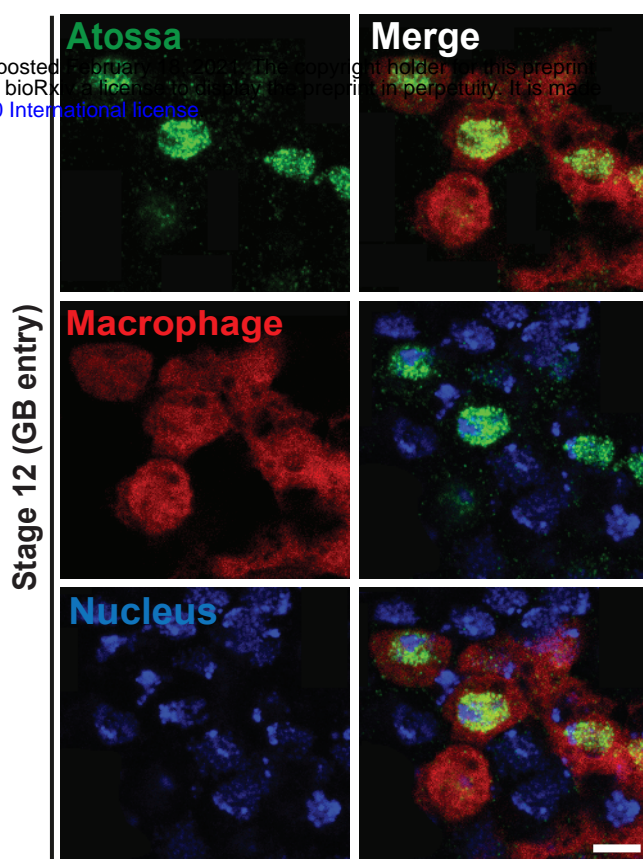
## Murine FAM214A



## Murine FAM214B

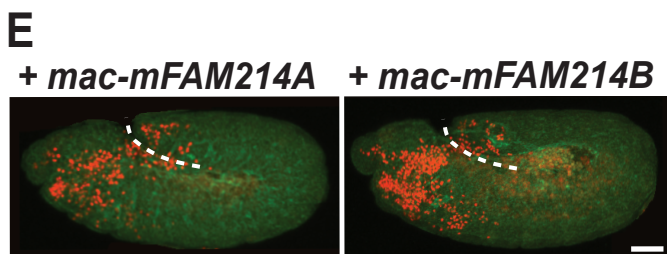
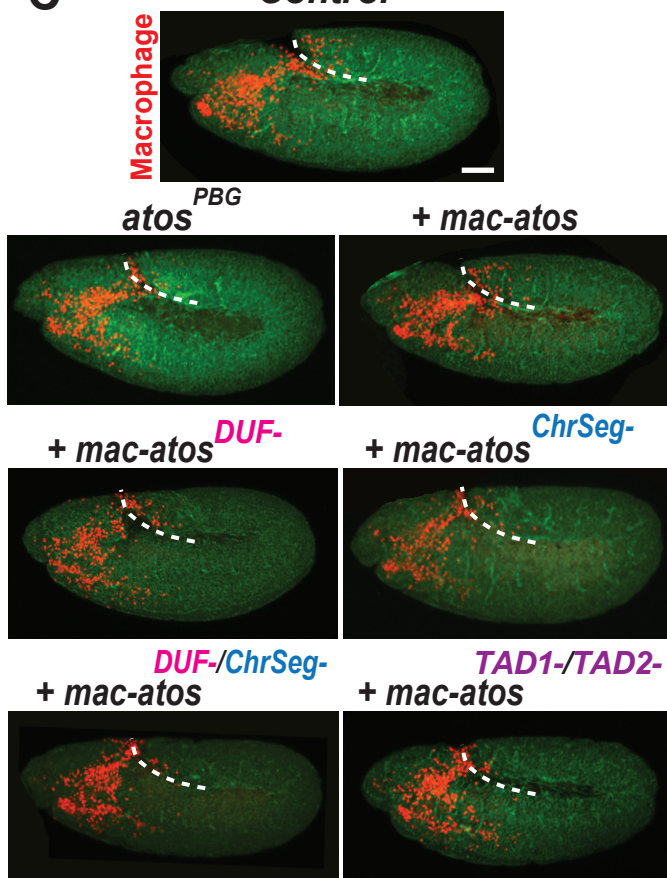


B

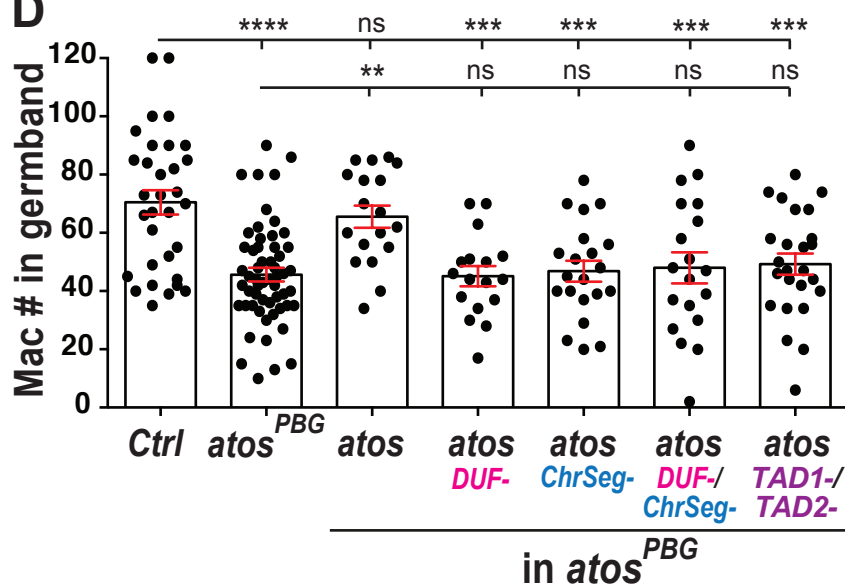


C

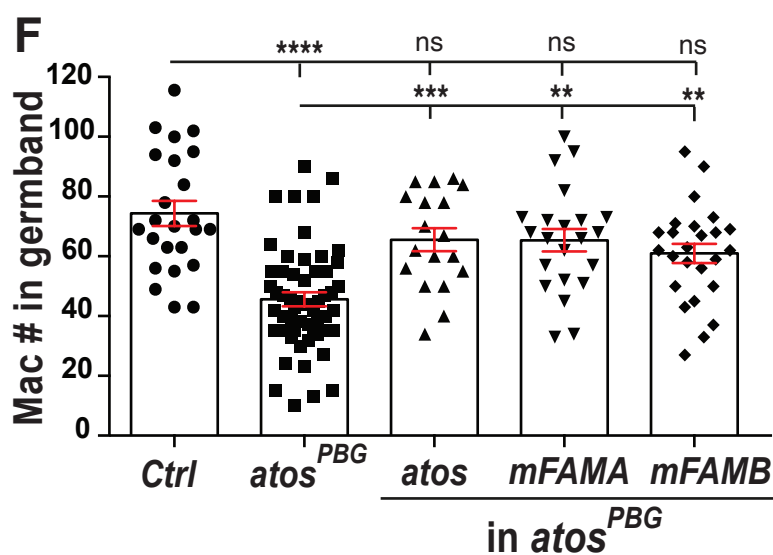
## Control



D

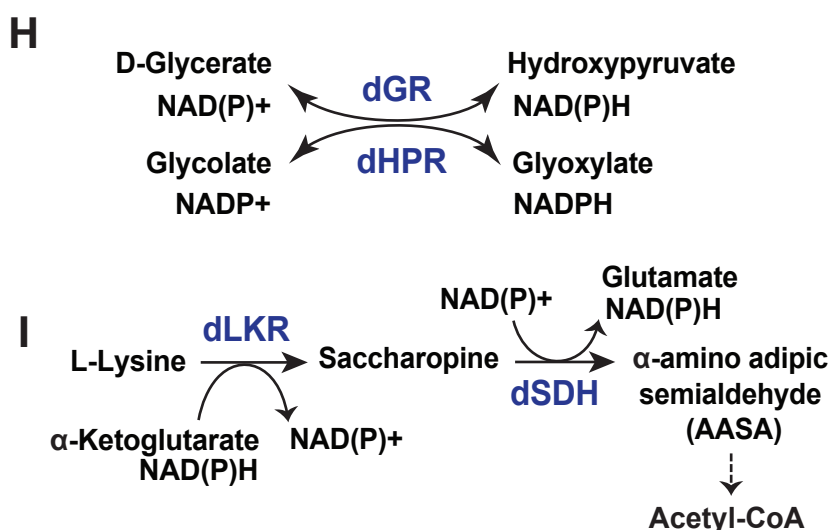
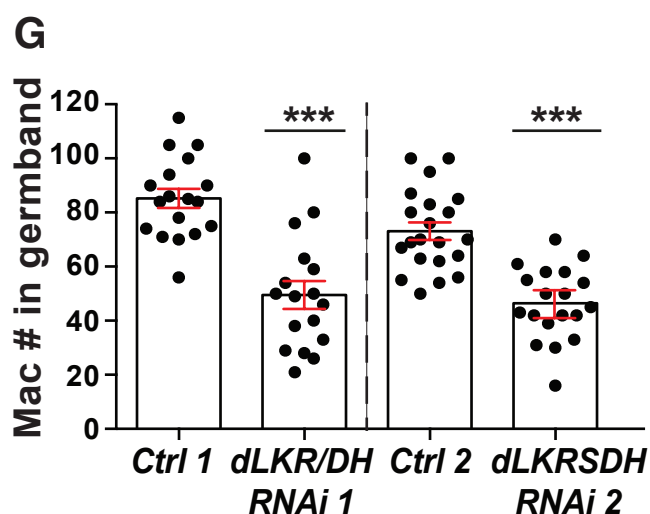
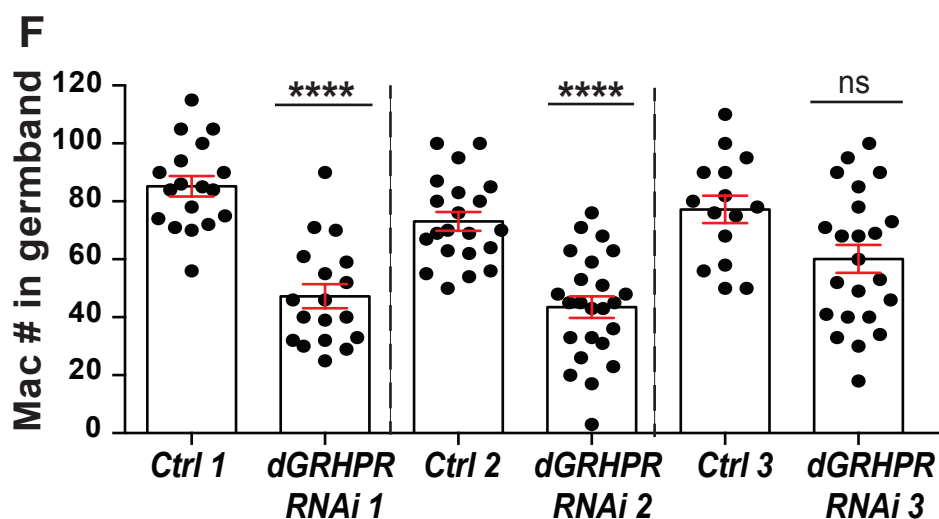
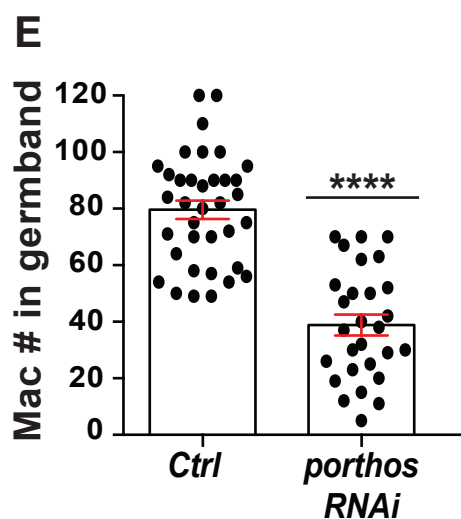
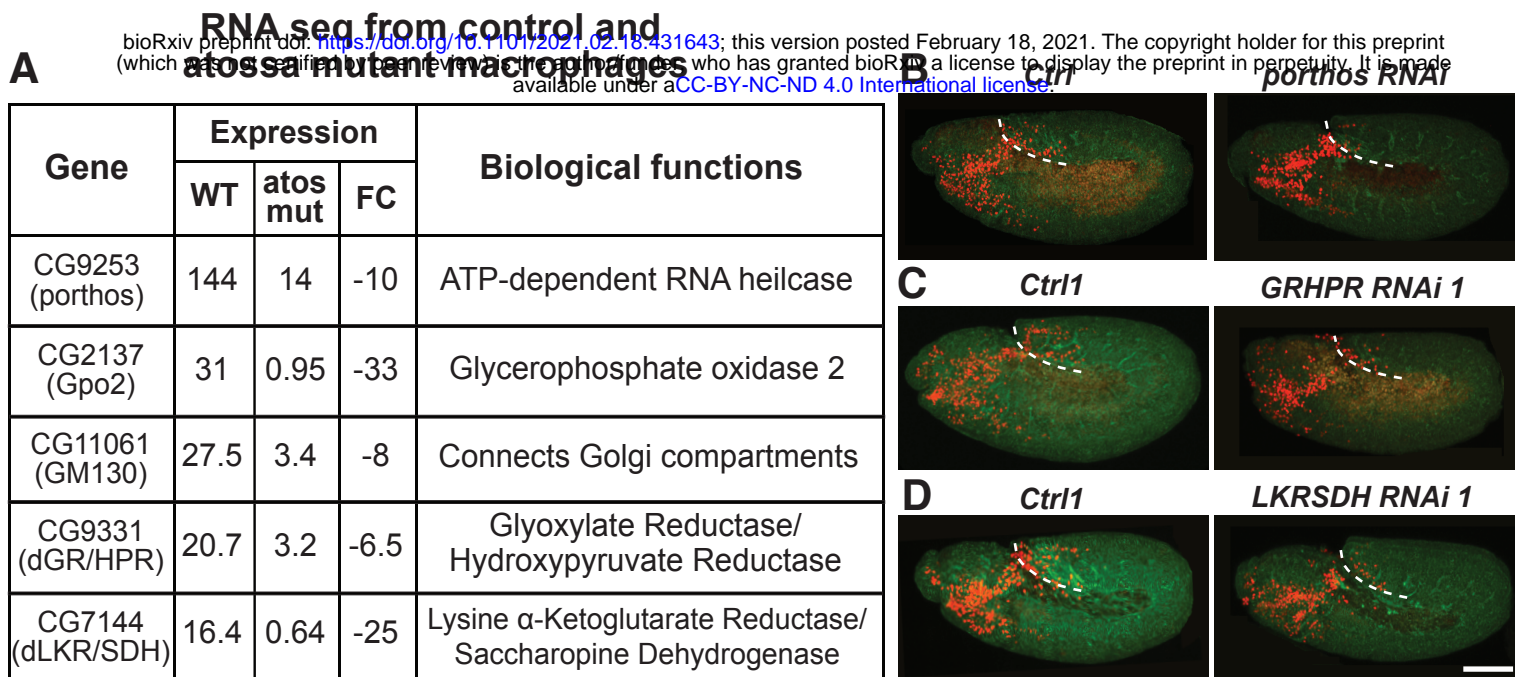


E

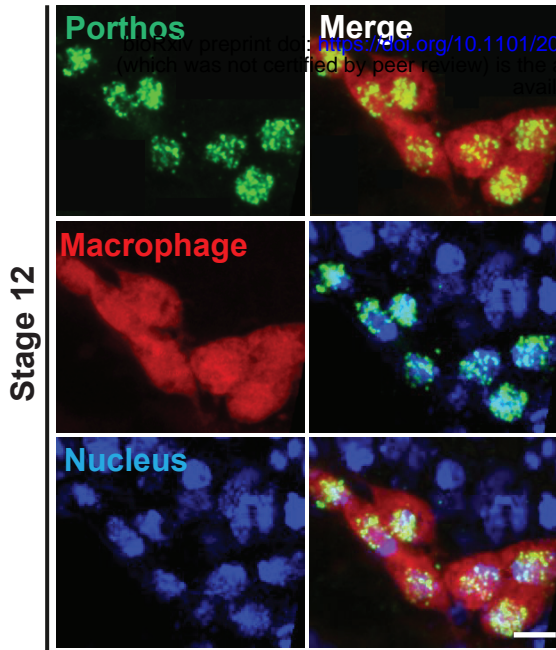




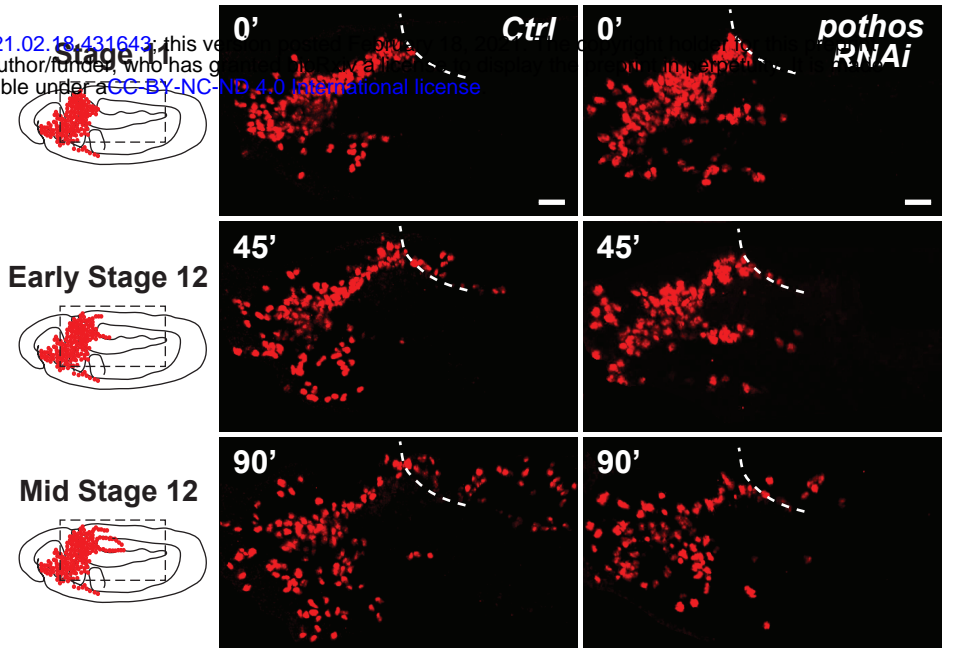
bioRxiv preprint doi: <https://doi.org/10.1101/2021.02.18.431643>; this version posted February 18, 2021. The copyright holder for this preprint (which was not certified by peer review) is the author/funder, who has granted bioRxiv a license to display the preprint in perpetuity. It is made available under aCC-BY-NC-ND 4.0 International license.



A

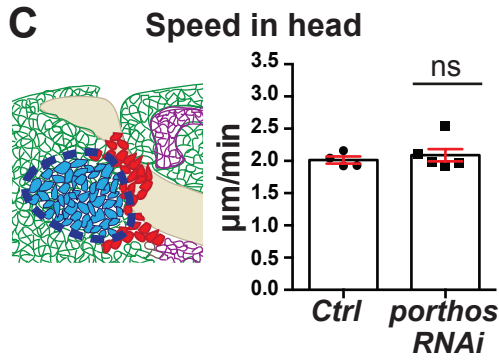


B

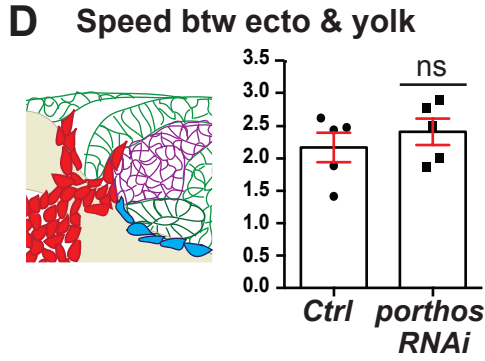


Macrophages Analyzed macrophages Yolk Ectoderm Mesoderm

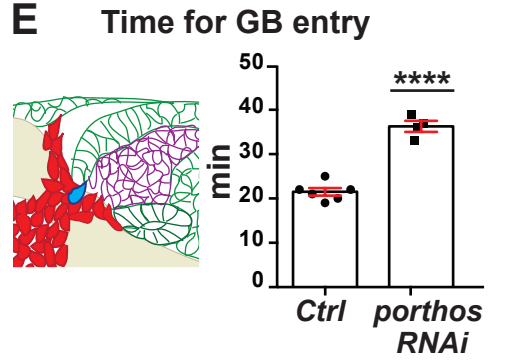
C



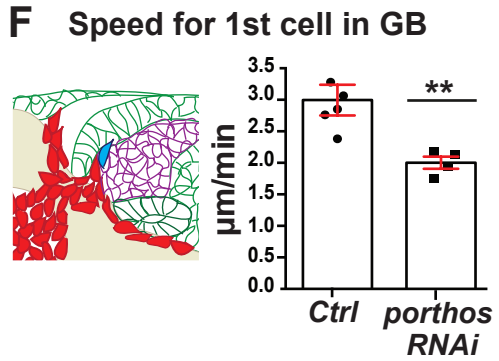
D



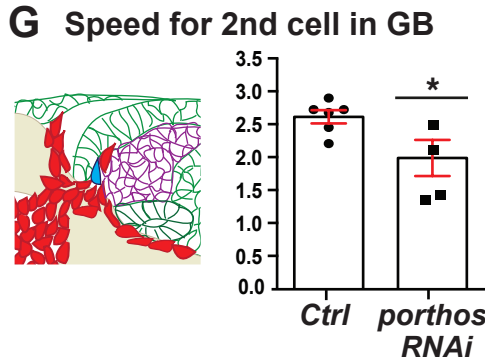
E



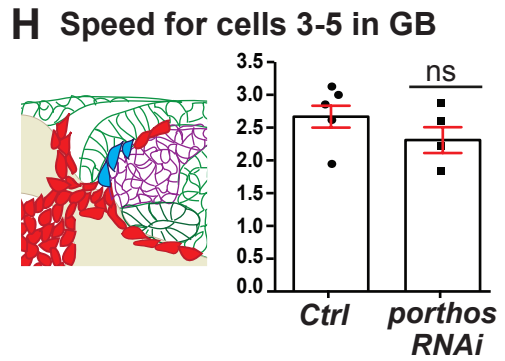
F



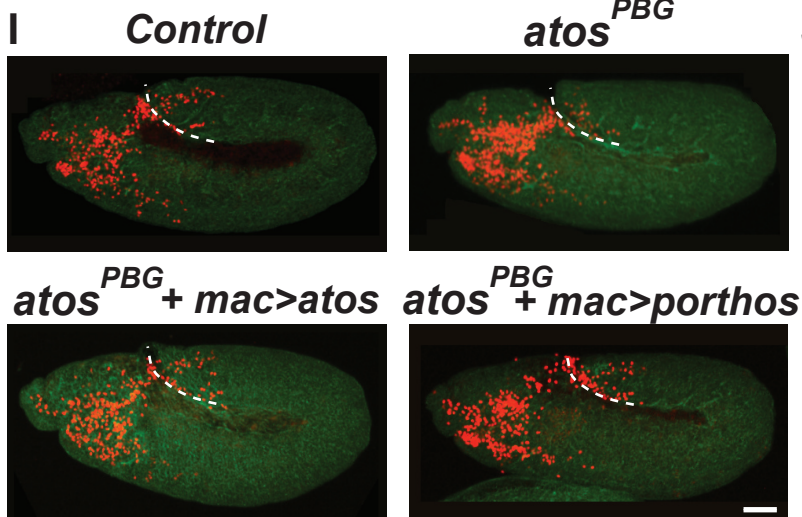
G



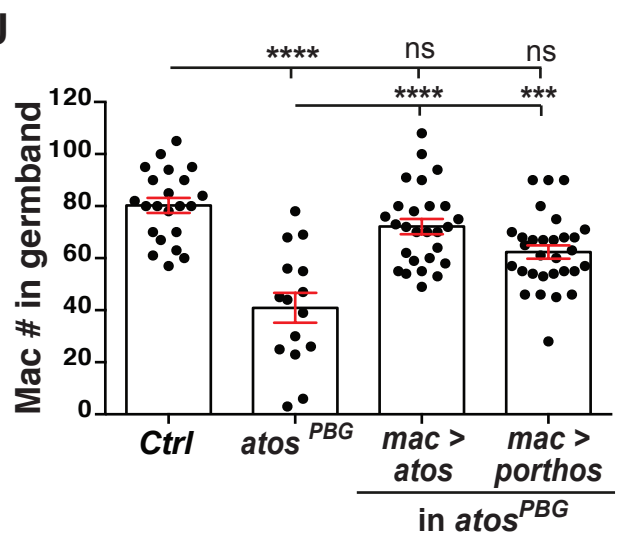
H

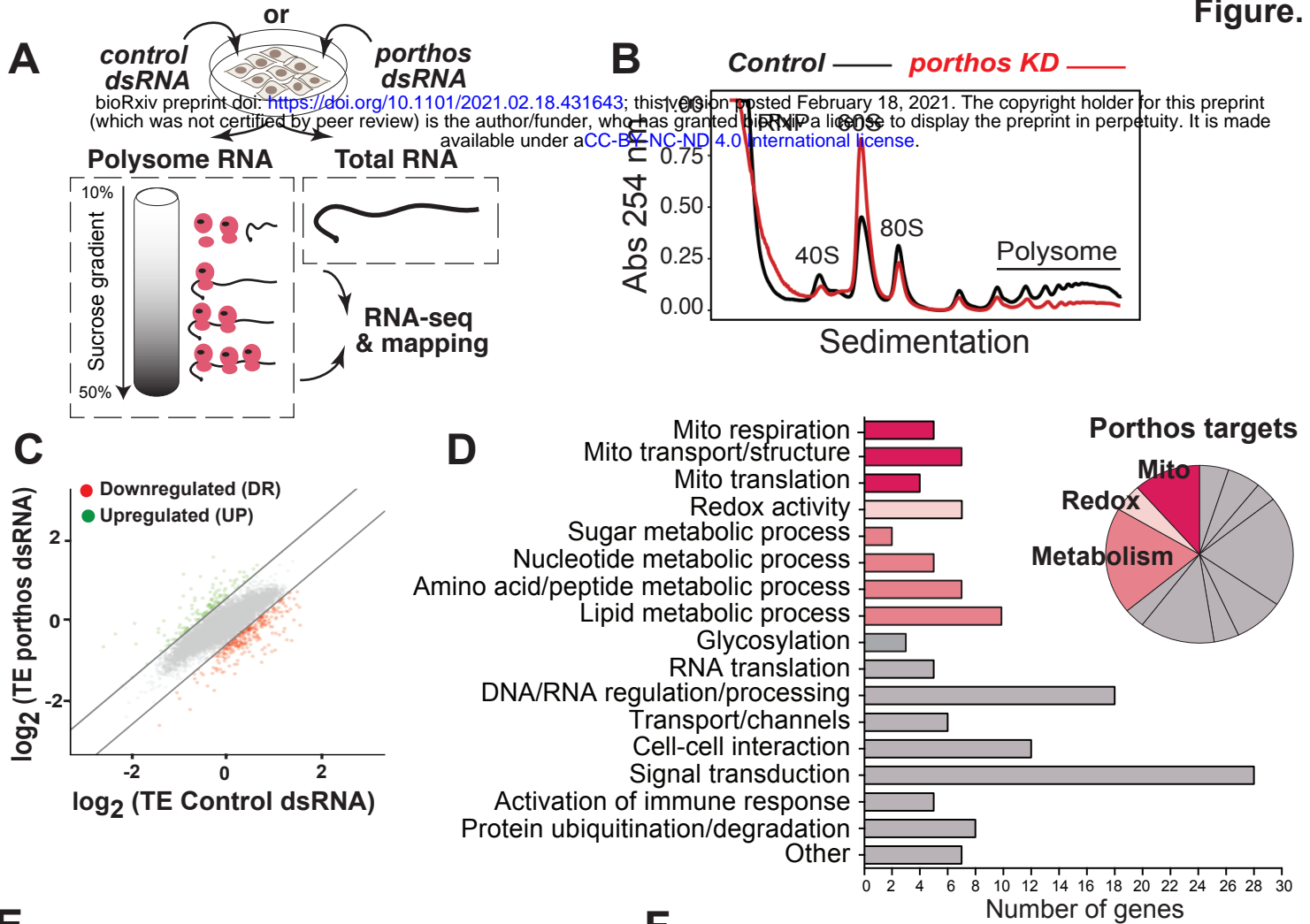


I



J





**E**

Cellular function	Gene symbol	Description of Porthos targets	Vertebrate ortholog
Mito respiration	CG3270	Complex I, NADH:ubiquinone oxidoreductase, predicted assembly factor	Foxred1
	CG8764	Complex III, ubiquinol-cytochrome c reductase, Oxen Qcr9	Uqcr10
	CG34242	Complex IV, mitochondrial cytochrome c oxidase predicted assembly factor	Smim20
	CG6105	Complex V, ATP synthase, Fo portion, subunit G (ATPsynG)	Atp5l
	CG10731	Complex V, ATP synthase, coupling factor B	Dmac2l
Mito transport/structure	CG1158	Tim17b1, Mito protein-transporting ATPase	Timm17a
	CG8860	Mitochondrial protein-transporting ATPase	Sec61g
	CG9090	Mpcp1, Mitochondrial phosphate carrier protein 1	Slc25a3
	CG5646	Acyl carnitine transmembrane transporter	Slc25a45
	CG1287	Mics1, Mitochondrial morphology/ cristae structure 1	Ghitm
	CG34132	Protein localization into MIM	Timm13
Mito translation	CG11110	Serine peptidase, protein targeting to mitochondrion	Immp2l
	CG2854	Predicted mitochondrial T cell activation inhibitor	Tcaim
	CG32531	mRpS14, mitochondrial ribosomal small protein S14	Mrps14
	CG13608	mRpS24, mitochondrial ribosomal small protein S24	Mrps24
Redox	CG34147	mRpL34, mitochondrial ribosomal large protein L34	Mrpl34
	CG11679	Predicted positive regulator of mito translation	Rmnd1
	CG9363	GstZ2, glutathione metabolic process	Gstz1
	CG11512	Mitochondrial GstD4, glutathione metabolic process	Gstt1
	CG6461	Ggt-1, glutathione metabolic process	Ggt1
Redox	CG14221	Glutathione metabolic process	Nme8
	CG6762	Sulfiredoxin, response to oxidative stress	Srxn1
	CG7460	Polyamine oxidase, redox process	Paox
CG5653	Redox process	Paox	

**F**

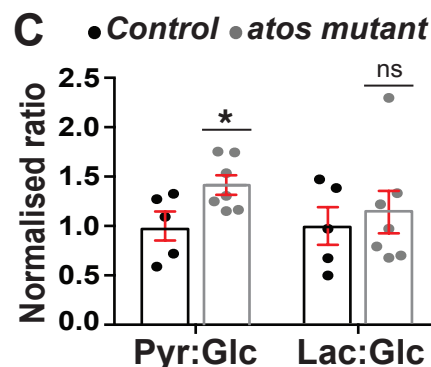
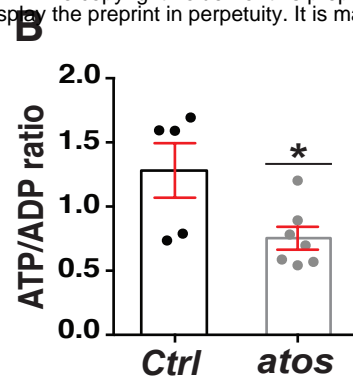
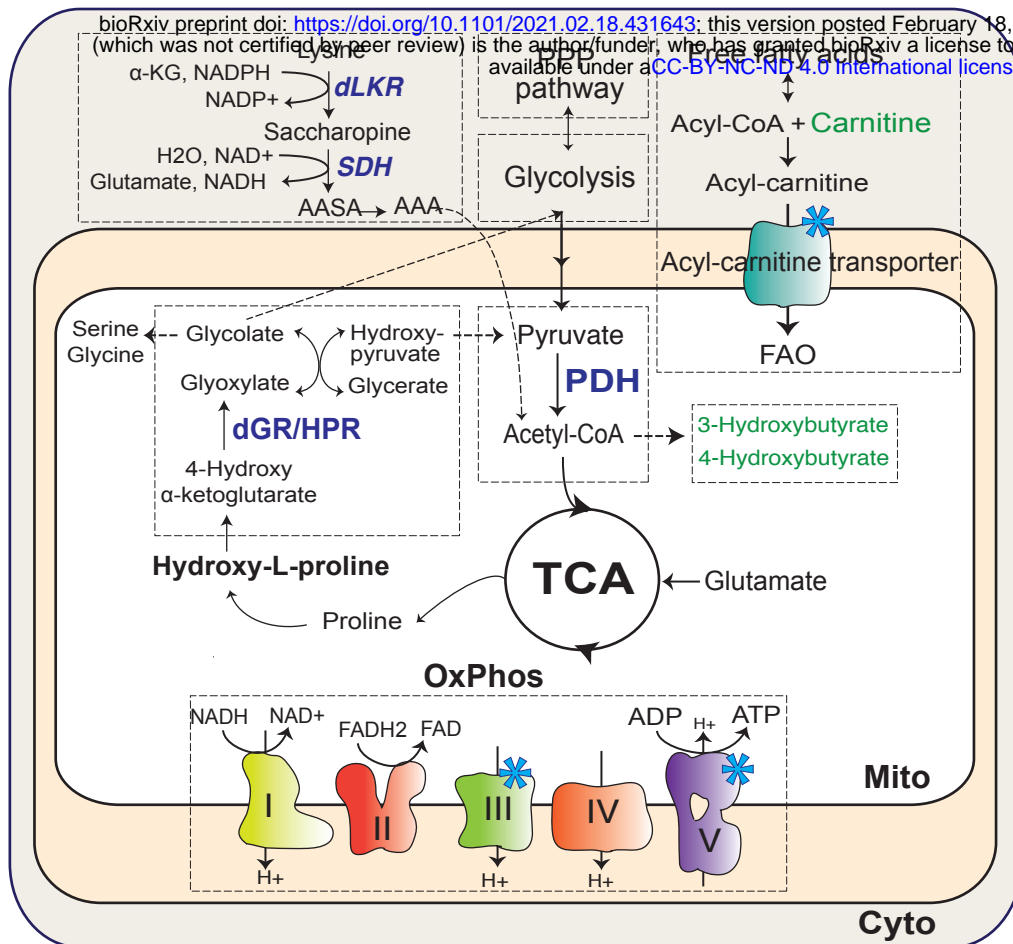
Cellular function	Gene symbol	Description of Porthos targets	Vertebrate ortholog
Sugar metabolism	CG42814	UDP-sugar diphosphatase	Nudt14
	CG14212	Haloacid dehalogenase, sugar dephosphorylation	Phospho1
Nucleotide metabolism	CG30016	Hydroxyisourate hydrolase, purine metabolism	Urah
	CG3788	Uridine phosphorylase	Upp1
	CG5828	Pantothenate kinase	Pank4
	CG33514	Phosphatidylinositol bisphosphate binding	Civs1
	CG7735	ADP ribosylation factor-like 6	Arl6
Amino acid/peptide metabolism	CG5840	P5cr-2, Pyrroline-5-carboxylate reductase-like 2	Pycr1
	CG7768	Peptidylprolyl isomerase	Ppif
	CG11843	Acylaminoacyl-peptidase	F12
	CG34041	Methylation of glycine to generate sarcosine	P4ha2
	CG6188	Gnmt, Glycine N-methyltransferase	Gnmt
	CG14990	SPH97, serine-type endopeptidase	Tpsab1
	CG10764	Acylaminoacyl-peptidase	NF
Lipid metabolism	CG7367	Carboxylesterase	Liph
	CG17562	Fatty-acyl-CoA reductase	Far2
	CG11052	Acylphosphatase	Acyp2
	CG8303	Fatty-acyl-CoA reductase (alcohol-forming)	Far1
	CG9709	Acox57D-d, acyl-Coenzyme A oxidase	Acox1
	CG8498	Acbp1, Acyl-CoA binding protein 1	Acbd7
	CG13091	Sgroppino, fatty-acyl-CoA reductase	Far2
Glycosylation	CG2985	Yolk protein 1, carboxylesterase	Lipi
	CG11129	Yolk protein 3, carboxylesterase	Lipi
	CG31956	N-Acetylgalactosaminyltransferase 4	Galnt10
Glycosylation	CG33774	Protein N-linked glycosylation	Ost4
	CG3253	Glucuronosyltransferase, O-linked mannosylation	B4GAT1







**A** Altered metabolic pathways in *atos* embryos:  
Significantly upregulated metabolites compared to the control



**D** Avg FC

Dipeptides	Avg FC	Significance
Val-HydroxyPro	3.04	****
Met-Glu	3.02	*
Ser-Tyr	1.20	*
Arg-HydroxyPro	1.17	*
Cys-Asp	0.89	
Ala-Pro	0.92	*
Arg-Glu	0.80	
Leu-Gln	0.68	
His-Pro	0.63	

**E** Avg FC

Carnitine metabolism	Avg FC	Significance
Carnitine	0.50	*
Acetyl-carnitine (C2)	-0.10	
Propionyl-carnitine (C3)	1.0	
3-Hydroxybutyryl-carnitine (C4)	0.04	
Hexanoyl-carnitine (C6)	0.52	
Lauryl-carnitine (C12)	1.08	
Myristoyl-carnitine (C14)	1.60	
Pentadecanoyl-carnitine (C15)	1.16	
Palmitoyl-carnitine (C16)	0.92	
Stearoyl-carnitine (C18)	0.20	
Behenoyl-carnitine (C22)	0.18	
3-Hydroxybutyric acid	2.94	*

**F** Avg FC

Ketone bodies	Avg FC	Significance
3-Hydroxybutyric acid	2.94	*
4-Hydroxybutyric acid	2.18	**

